Finding Companions in the YSES IFS Data

MSc Thesis

Zachary Burr

Delft University of Technology

TUDelft

Finding Companions in the YSES IFS Data

MSc Thesis

by

Zachary Burr

to obtain the degree of Master of Science
at the Delft University of Technology.
to be defended publicly on Friday January 26, 2024 at 14:00.

Student number:	4659821
Supervisor:	Dr.ir. M.A. Kenworthy
Institution:	Delft University of Technology, Faculty of Aerospace Engineering
Project duration:	May 2023 – January 2024

Style:	TU Delft Report Style, with modifications by Daan Zwaneveld

TU Delft

Preface

This thesis represents the culmination of all my years as a student, and around a year full of intense work. This was a very fun project to work on: I learned so much about exoplanets, high contrast imaging, and astronomy in general. This thesis, much like my entire student career, was oftentimes full of struggle, but looking back I am incredibly proud of what I have accomplished: both in this past year working on this project and also my last seven years at TU Delft. I am so grateful to have had this opportunity to learn and grow and I think this study really shaped me into the person that I am today.

I would like to thank all the people that helped me along the way, but in particular my thesis supervisor Matt for all his wonderful guidance and advice. As well as Thomas Stolker for all the support with PynPoint during this project, and Rick Dullart for assisting with the evolutionary models. And I would especially like to thank my parents for all of their support: I would certainly not be here today if not for them.

<div align="right">

Zachary Burr
Delft, January 2024

</div>

Note: This work contains some sections originally included as part of the author's literature survey.

Summary

Planet formation is a topic that still has many unanswered questions, particularly regarding the formation of wide orbit giant planets. Detecting more of these types of planets can aid understanding of how they form by giving examples of what kind of planets exist. Direct imaging is uniquely well suited to detecting these kinds of planets, which is why several direct imaging surveys have been launched with this goal. Including the Young Suns Exoplanet Survey, which is looking specifically for wide orbit giant planets around young solar analogues.

The survey makes use of the IRDIS instrument on the VLT, which images in parallel with the IFS. By analyzing the IRDIS data, the researchers have already detected three planets in two systems. However, the IFS data has not yet been analyzed. That was the goal for this thesis: to contribute to YSES and the broader scientific community by analyzing the IFS data to search for potential companions.

In total, 41 observations of 37 different star systems were analyzed. The data was pre- and post-processed (with SDI), and candidate companions were identified and examined. Eight candidate companions were found in five systems. Of those candidates, all were determined to be background stars and not related to the host. Two were bright single stars. One system had two M-dwarf candidate companions that were in a binary system together. The last two systems each had two candidate companions, and in both cases it was revealed that these candidates form a triple system of their own, with one of the candidates being an unresolved binary. One of these triple systems was previously thought to be an equal mass binary with the host star, however this thesis has proved that this is not the case.

All of the systems analyzed also had detection limits computed. This gives a good idea for what size of objects could have been seen if they had been in the images. For most systems, the limit after SDI is around 5–$10 M_J$ at 0.3”–0.5”. This leaves room for planetary mass companions in these systems which could be found in follow-up observations. The two background triple systems should also have follow-up observations performed, as this configuration is somewhat unusual and warrants further study.

Contents

List of Figures

List of Tables

vii

Nomenclature

Abbreviations

Abbreviation	Definition
ADI	Angular Differential Imaging
ALC	Apodized pupil Lyot Coronagraph
AO	Adaptive Optics
CI	Classical Imaging
CPI	Common Path and Infrastructure
DBI	Dual-Band Imaging
ESO	European Southern Observatory
FF	Flat Field
FOV	Field of View
FPF	False Positive Fraction
GPIES	Gemini Planet Imager Exoplanet Survey
IFS	Integral Field Spectrograph
IFU	Integral Field Unit
IRDIS	InfraRed Dual-band Imager and Spectrograph
LCC	Lower Centaurus Crux
NRMSE	Normalized Root Mean Square Error
PSF	Point Spread Function
SAXO	Sphere Ao for eXoplanet Observation
Sco-Cen	Scorpius Centaurus moving group
SDI	Spectral Differential Imaging
SHINE	SpHere INfrared survey for Exoplanets
SNR	Signal to Noise Ratio
SPHERE	Spectro-Polarimetric High-contrast Exoplanet REsearch
VLT	Very Large Telescope
WFS	Wave Front Sensor
YSES	Young Suns Exoplanet Survey
ZIMPOL	Zurich IMaging POLarimeter

Symbols

Symbol	Definition	Unit
D	Telescope diameter	m
$M_{\odot}$	Solar mass	kg
M_J	Jupiter mass	kg
T_{eff}	Effective temperature	K
λ	Wavelength	μm

1

Introduction

The topic of planet formation is not yet well understood, especially regarding the formation mechanisms of wide orbit giant planets.(Morbidelli and Raymond, 2016) The best method to detect and analyze such planets is with direct imaging, as other detection methods (such as transits or radial velocity) have a drop off in sensitivity at larger distances.(Marois et al., 2008) In recent years, several surveys have been initiated with the goal of finding these wide orbit companions, including the Gemini Planet Imager Survey (GPIES; Nielsen et al., 2019), the SpHere INfrared survey for Exoplanets (SHINE; Vigan et al., 2021), and the Young Suns Exoplanet Survey (YSES; Bohn et al., 2021). These surveys aim to increase our understanding of how these objects form by looking at what type of planets are out there, and where and how readily they form.

YSES focuses on young (<20Myrs old), sun-like stars (approximately $1M_\odot$) to search for companions there. The survey is being performed with the Spectro-Polarimetric High-contrast Exoplanet REsearch (SPHERE) extreme adaptive optics (AO) system of the Very Large Telescope (VLT). So far YSES has detected three new planets in two different systems using the InfraRed Dual-band Imager and Spectrograph (IRDIS).(Bohn et al., 2020a,b, 2021) During the survey, images were also made of most of the systems utilizing the Integral Field Spectrograph (IFS) instrument imaging in parallel with IRDIS. This data from the IFS has not yet been analyzed, so there may still be some companions hiding in those images. This thesis aims to further the goals of the YSES survey and the broader scientific community by analyzing these images to find new wide orbit planets, and answer the main research question:

What companions can be identified in the IFS data from YSES, and what are the characteristics of these companions?

This thesis will present the work performed over the past few months to answer this question. It will be broken down into three parts. Part I gives background information necessary for the thesis, beginning with information on previous direct imaging research in Chapter 2. A brief explanation of YSES, the survey this thesis is contributing to, will be presented in Chapter 3. And Chapter 4 will present some information about the instrument used for the thesis. The methodology used to carry out this work will be presented in Part II: Chapter 5 will discuss the reduction, the first step to processing the images; then Chapter 6 will explain postprocessing, the method by which the light of the star is subtracted out to reveal the companions. The methods used to characterize the companions will be outlined in Chapter 7. Finally, Part III gives the results of the companions detected and their properties in Chapter 8 and conclusions and recommendations for future work in Chapter 9.

Part I

Background

<div style="text-align: right; font-size: 3em;">2</div>

History of Direct Imaging

Before trying to detect new planets with direct imaging, it is useful to see what has been achieved with direct imaging thus far. In Section 2.1 an overview of direct imaging and its merits compared to other exoplanet detection methods will be given. Then a select group of significant detections of planetary mass companions will be discussed in Section 2.2. In Section 2.3 some results from current direct imaging surveys will be mentioned.

2.1. Direct Imaging vs. Other Detection Methods

At time of writing, there are 5539 confirmed exoplanets discovered with various different methods.[1] In Figure 2.1, a number of these planets are plotted by mass and semi-major axis, and labeled by what method they were detected with. Around 60 of these exoplanets were detected using direct imaging.[2] This is a comparatively low number of detections compared to other methods like radial velocity or transits, however direct imaging works very well to detect those planets the other methods cannot.
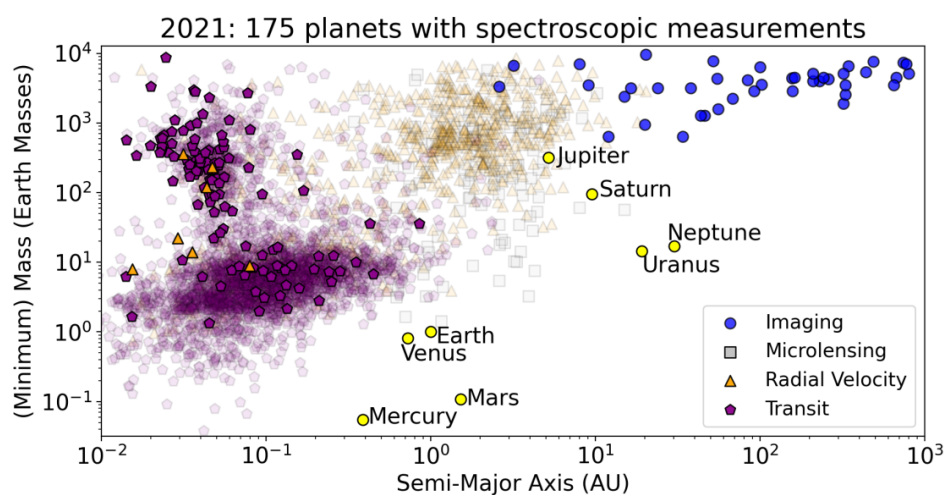
Figure 2.1: Distribution of planetary-mass companions detected with various methods. The bold symbols denote those planets with spectroscopic measurements (175 planets as of 2021). Solar system planets are included for comparison. Direct imaging is ideal for detecting wide orbit giant planets, and for retrieving spectra, which cannot be done with other methods. Taken from Currie et al. (2023).

Other methods decrease in effectiveness with separation from the host star, whereas direct imaging performs best for wide separations.(Marois et al., 2008) With current methods, direct imaging can only

---

[1]Exoplanet catalog: `https://exoplanets.nasa.gov/discovery/exoplanet-catalog/`, accessed 2023-11-13

[2]See footnote 1.

detect giant planets, specifically those that are young and thus hot and self luminous. Imaging can help fill in the gaps of wide orbit planets that the other methods cannot detect. Direct imaging is the only way to retrieve spectra for planets that are not transiting. In Figure 2.1 it can be seen that directly imaged planets make up a significant portion of those planets which have spectroscopic measurements. Hopefully with the next generation of extremely large telescopes, it will be possible to image smaller planets, and/or planets at smaller separations, and thus retrieve spectra for some of those planets originally detected with radial velocity.(Artigau et al., 2018)

2.2. Notable Direct Imaging Detections

Too many planets have been discovered with direct imaging to discuss all of them, so only a few of the most notable planets will be discussed here, with their most important features highlighted. Images of a select few of these are displayed in Figure 2.2.

First Detections

The first planetary mass companion to be discovered with direct imaging was found orbiting 2MASSWJ 1207334−393254 (or 2M1207) in 2004.(Chauvin et al., 2004) It was confirmed as a companion in 2005 after follow up observations proved it had common proper motion.(Chauvin et al., 2005) The companion has a mass of approximately 5 M_J, and orbits a 25 M_J M dwarf. This was quickly followed by the detections of DH Tau b and GQ Lup b in 2005.(Itoh et al., 2005; Neuhäuser et al., 2005) These detections were made with the first generation of AO systems (VLT/NACO for 2M1207b and GQ Lup b, and Subaru/CIAO for DH Tau b). A few more detections were made in the next couple years, but the real watershed moment for direct imaging came with the detections of HR 8799 bcd in late 2008 and β Pictoris b in early 2009.(Marois et al., 2008; Lagrange et al., 2009)

HR 8799

HR 8799 is a mid-A field star with a massive debris disk, which shows signs of perturbation due to massive planets.(Su et al., 2009) Three of these planets were discovered in 2008, with a fourth, inner planet discovered two years later.(Marois et al., 2008, 2010) This was the first ever multiple planet system discovered via direct imaging, and one of only six to be confirmed thus far.[3] The system still boasts more confirmed planets than any other directly imaged system. The planets were also discovered in older archival images of the system.(Lafrenière et al., 2009) A decade of archival data allowed for placing constraints on the orbits of these planets, which appear to be in or close to a 1:2:4:8 orbital resonance.(Konopacky et al., 2016) These planets have projected separations ranging from 15-70 AU; their masses are calculated to range from 5-13 M_J based on their magnitude, but dynamical constraints put the masses below 10 M_J for cde or 7 M_J for b.(Marois et al., 2010) This is one of the best studied systems, with a number of papers about characterizing the planets and their orbits.(e.g. Greenbaum et al., 2018; Mollière et al., 2020; Wang et al., 2018) The system is said to resemble a scaled up version of the outer part of our solar system.(Marois et al., 2008) An image of the four planets can be found in Figure 2.2a.

β Pictoris

β Pic is an A type star, and is the eponymous member of the β Pic Moving Group. It has a debris disk, which has been imaged many times over several decades. The disk was long thought to be associated with planet formation due to its flattened shape.(Smith and Terrile, 1984) In 2009 β Pic b was imaged within the inner edge of the disk, at a projected separation of about 8 AU.(Lagrange et al., 2009) The detection was confirmed with follow-up observations the following year.(Lagrange et al., 2010) The planet's separation of 8-15 AU is still one of the smallest separations of any directly imaged planet. In 2019, Lagrange et al. (2019) found a second planet in the system via the radial velocity method and the planet was directly imaged one year later with the Very Large Telescope Interferometer instrument Gravity. β Pic c has a mass of 8.2 M_J, slightly smaller than the 9.3 M_J mass of β Pic b, and has a

---

[3]Exoplanet catalog: `https://exoplanets.nasa.gov/discovery/exoplanet-catalog/`, accessed 2023-11-13

projected separation of only 2.7 AU.(Nowak et al., 2020) HR 8799 and β Pictoris are probably the most famous and best studied of all the directly imaged planetary systems. The planet β Pic b can be seen in Figure 2.2b.
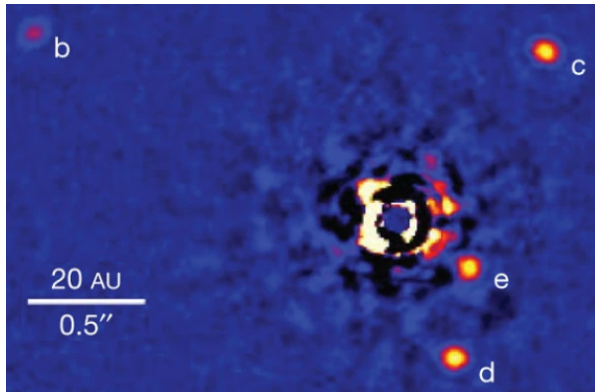
(a) HR8799 system with all four planets labeled. Adapted from Marois et al. (2010).
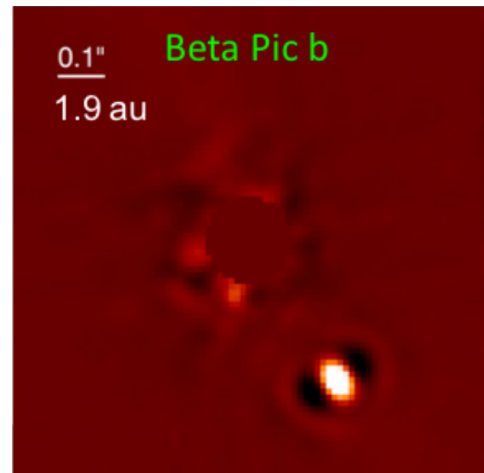
(b) β Pic b. β Pic c is not visible in this image. Taken from Currie et al. (2023).
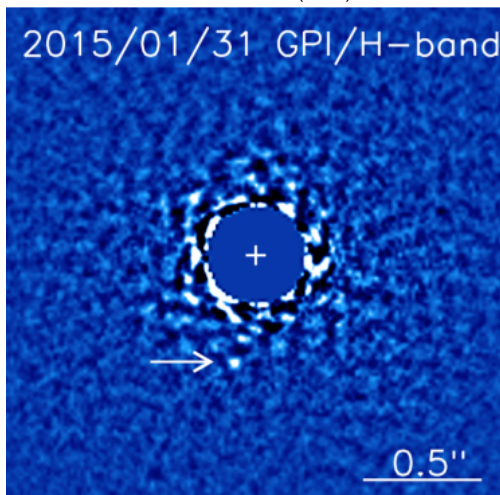
(c) Image of 51 Eridani b. Taken from Macintosh et al. (2015)
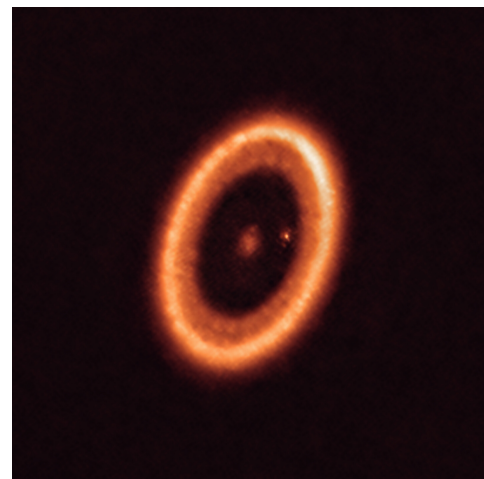
(d) Image of the PDS 70 system. The protoplanetary disk is clearly visible, as well as the planet PDS 70 b on the center right. PDS 70 c is not shown in this image. Taken from ESO.[4]

Figure 2.2: Images of four notable systems with directly imaged planetary mass companions.

51 Eridani

51 Eridani b was the first planet to be discovered with the current generation of extreme AO systems, using the Gemini Planet Imager. The planet has a separation of about 13 AU, and a mass from 2 to 9 M_J, with the lower end meaning it would be one of the lowest mass companions imaged.(Macintosh et al., 2015) The star is an F type and part of the β Pic Moving Group. It is part of a wide triple system with binary M dwarfs GJ 3305AB.(Feigelson et al., 2006) This makes it one of few exoplanets discovered in such a multi star system.[5] GJ 3305 may be the cause of the estimated high eccentricity in the orbit of 51 Eri b.(Maire et al., 2019) In Figure 2.2c an image of the planet can be found.

---

[4]The PDS 70 system as seen with ALMA: `https://www.eso.org/public/images/eso2111b/`, accessed 2023-12-17

[5]Planets in binary systems: `http://www.openexoplanetcatalogue.com/systems/?filters=multistar`, accessed 2023-11-13

PDS 70

PDS 70 b was discovered in a gap in the dust cloud of its host star.(Keppler et al., 2018) It was followed by the detection of a second planet c the following year.(Haffert et al., 2019) These planets are still actively accreting, making these the first detections of protoplanets still undergoing formation. The mass of the host star is around 0.9 $M_\odot$, making it one of very few planetary systems found around a sun-like star. Both PDS b and c have some of the lowest mass ratios of any directly imaged companions.(Bohn et al., 2020a) PDS 70 b and the protoplanetary disk around the star can be seen in Figure 2.2d.

GJ 504

The star GJ 504 is a 1.2 $M_\odot$ with an age of about 160 Myr. This makes GJ 504 b one of few planets imaged around a sun-like star, and one of the oldest (and thus coolest) planets imaged to date. The planet likely has a mass of between 3 and 5.5 M_J.(Kuzuhara et al., 2013) This gives it the lowest mass ratio with its host star of any planet discovered with direct imaging around a sun-like star to date.(Bohn et al., 2020a)

TYC 8998

TYC 8998, also known as YSES 1, is one of few imaged systems with a sun-like host star (mass 1 $M_\odot$), and one of even fewer multi planet systems discovered with direct imaging. There are two planets: b with a mass of about 14 M_J and projected separation of 162 AU, and c with a mass of around 6 M_J and projected separation of 320 AU.(Bohn et al., 2020a,b) Both planets have very low mass ratios with their host star relative to other directly imaged planets. YSES 1c has one of the furthest separations from its host star of any confirmed exoplanet. An image of the YSES 1 system can be found in Figure 3.1a.

2.3. Direct Imaging Surveys

Over the years several large and small scale direct imaging surveys have been carried out to detect wide orbit giant planets. The current generation of direct imaging surveys target hundreds of stars using 8 m class telescopes, extreme adaptive optics, sophisticated speckle suppression, and coronography.(Currie et al., 2023) Some current surveys and their most important findings will be discussed here. SHINE and GPIES are the two largest ongoing surveys. Some smaller more focused surveys will also be mentioned, but this is not an exhaustive list. A summary of all the surveys mentioned here is given in Table 2.1. Based on meta-analysis, most surveys tend to detect about one planetary mass companion per 100 stars.(Bowler and Nielsen, 2018)

Table 2.1: Summary of current direct imaging surveys.

Survey	Number of stars	Type of targets	Example paper
SHINE	500	0.5-3 $M_\odot$	Langlois et al. (2021)
GPIES	600	All types	Nielsen et al. (2019)
COCONUTS	3×10^5	Ultrawide orbit companions	Zhang et al. (2020)
SCExAO/CHARIS	-	Accelerating stars	Currie et al. (2021)
SPOTS	62	Binary stars	Asensio-Torres et al. (2018)
YSES	70	1 $M_\odot$	Bohn et al. (2021)

SHINE

SHINE is a 500 star survey utilizing VLT/SPHERE. The survey began in 2015 with the goal of constraining the frequency of substellar companions with separation >5 AU for varying host star mass.(Desidera et al., 2021) 17 substellar companions were imaged during the course of the survey, including seven brown dwarfs and 10 planetary mass companions. Only two of these companions are new detections: planetary mass companion HIP 65426 b and brown dwarf HIP 64892 B.(Langlois et al., 2021) The survey has determined an occurrence rate of at least one substellar companion of 23.0%, 5.8%, and

12.6% for BA, FGK, and M stars, respectively.(Vigan et al., 2021)

GPIES

GPIES is a counterpart to SHINE, but using the Gemini Planet Imager instead of SPHERE. This survey targets a similar number of stars, with similar goals of inferring the occurrence rate of wide orbit substellar companions. The survey has detected two new companions including planet 51 Eri b (mentioned above) and brown dwarf HR 2562, as well as performing additional observations of previously detected companions. Based on the first half of the survey, the researchers conclude an occurrence rate of specifically planetary mass companions of 9% around stars >1.5 $M_\odot$. They additionally find that higher mass stars are more likely to have wide orbit giant planet companions.(Nielsen et al., 2019)

COCONUTS

COCONUTS (COol Companions ON Ultrawide orbiTS) is a smaller survey focused on companions at ultra wide separations above 500 AU. The survey has so far discovered two new brown dwarfs, and a new planetary mass companion.(Zhang et al., 2020, 2022, 2021) The planet, COCONUTS-2b, is the nearest imaged planet to Earth known to date, at 10.9 pc.

SCExAO/CHARIS HGCA

This survey uses the Hipparcos Gaia Catalog of Accelerations to determine targets that show accelerations with precise radial velocity measurements, likely due to companions orbiting them. These are then imaged using SCExAO/CHARIS.(Currie et al., 2021) Thus far at least one new brown dwarf companion has been detected around a sun-like star with this approach.(Currie et al., 2020)

SPOTS

SPOTS is the Search for Planets Orbiting Two Stars. The survey focused specifically on imaging binary stars, as these targets are often excluded from other surveys. This way they could hopefully derive meaning results about the occurrence rates of planets orbiting binary stars. The survey has not discovered any new companions, but was able to use detection limits on their observations to set an upper bound for the occurrence rate of such planets.(Asensio-Torres et al., 2018)

YSES

YSES is the survey that the thesis work is contributing to, and is explained much more thoroughly in its own section in Chapter 3.

<div style="text-align: right">

3

</div>

<div style="text-align: right">

Data

</div>

In order to perform data analysis, there must be a dataset to analyze. The thesis will make use of data from YSES. This chapter will explain where the data is coming from, and what YSES is all about. Section 3.1 will deliver some background information about YSES and its goals, as well as explaining what data from the survey will be used for the thesis. Then in Section 3.2, the details of the targets that were observed with YSES will be explained. Finally the strategy used by YSES to observe these targets will be outlined in Section 3.3.

3.1. YSES Background

YSES is a survey that was led by Leiden Observatory PhD student Alexander Bohn, as well as other researchers from Leiden Observatory and abroad. It was initiated with the goal to get better estimations of the fraction of sun-like stars with planets, and to better understand the formation mechanisms of planets around sun-like stars.(Kenworthy et al., 2021) Prior to the survey, few planets had been imaged around sun-like stars, with the majority of imaged planets being found around B, A, or F stars, which are at least 1.5 $M_{\odot}$.(Currie et al., 2023) To achieve this goal it is necessary to investigate sun-like stars and hopefully discover planetary mass companions orbiting them.

Searching for systems similar to our own can help to answer a lot of questions about our own solar system. Questions like how common are systems like ours? and how did the planets of our solar system form and evolve over time?(Barbato et al., 2018; Martin and Livio, 2015) An even more interesting question is whether or not there is life elsewhere in the universe, and a natural place to start looking for this life is in systems similar to our own. The planets of our own system do not seem especially unusual when compared to known exoplanetary systems. The orbits of our system's planets are somewhat unique, with lower eccentricities and wider orbits than most other systems. However, this may simply be because wider orbit planets are more difficult to detect.(Martin and Livio, 2015) This is why it is important to try to find these systems and why it is particularly interesting to image sun-like stars to try and find planets there. Direct imaging is especially useful for finding and characterizing outer giant planets similar to Jupiter and Saturn, and with the advancement of telescopes and AO systems, may one day be able to image an Earth-like planet in the habitable zone.(Currie et al., 2023) This is why a survey such as YSES looking to directly image planets around sun-like stars is important.

Thus far the survey has three confirmed detections of planetary mass companions orbiting two different sun-like stars, as well as a protoplanetary disk.(Bohn et al., 2021, 2020a,b, 2019) Images of the three planetary mass companions can be seen in Figure 3.1. This is already a much higher detection rate than other similar surveys, which might point to the fact that planets are more likely to form around stars in the region where YSES was looking, or that the occurrence rates for planets around sun-like stars has been underestimated thus far.(Bohn et al., 2021) Thus far all of the companions found by YSES were discovered with SPHERE/IRDIS, and this instrument operates in parallel with SPHERE/IFS (both of which will be described in more detail in Chapter 4). The data from the IFS instrument has not yet been analyzed by the YSES team. To complete the survey, it is necessary to analyze the data from
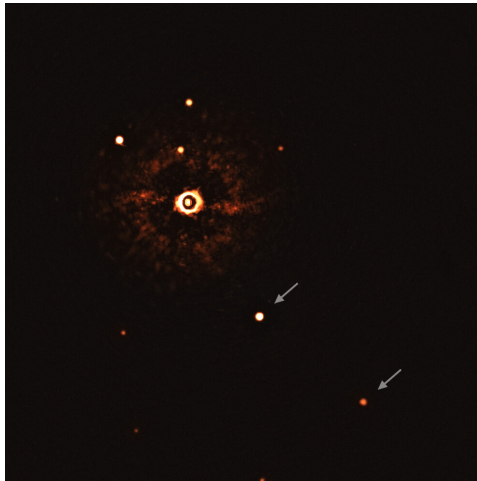
(a) Image of the YSES 1 system. The two planets are marked, with the other point sources being background objects. The speckles around the star are optical artifacts. Taken from ESO.[1]
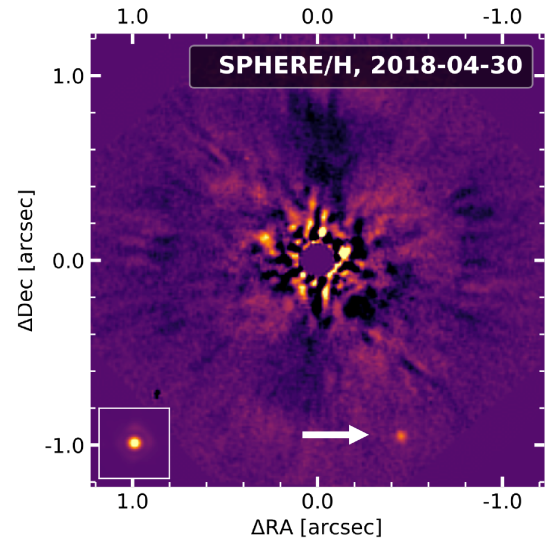
(b) Image of YSES 2, with the planet marked. Taken from Bohn et al. (2021).

Figure 3.1: The planets discovered by YSES thus far.

the IFS as well to see if there are any other companions that can be identified. These images taken by SPHERE/IFS as part of YSES will make up the dataset for the thesis work which will follow this report.

In addition to the observations taken as part of YSES, use will be made of the calibration data provided by ESO, which operates SPHERE. This calibration data is necessary for the reduction, which is explained in Chapter 5.

3.2. YSES Target Selection

One of the most important parts of carrying out a survey such as YSES is the selection of which targets to observe. Telescope time is limited so observations cannot be made of everything, but instead the most promising targets must carefully selected. Direct imaging is currently only able to observe planets around young, nearby stars.(Currie et al., 2023) If the stars are too far away the projected separation between the planet and its host star will be too small, and it will be impossible to observe. If the planet is too old, it will be too cold to observe. Currently we can only image planets that are self luminous: those that give off a significant amount of radiation in the IR spectrum due to their high temperature just after forming. As the planet ages, it will cool down and have a lower luminosity.(Marley et al., 2007) The next generation of 30m class telescopes might be able to image planets in the optical by looking at the light they reflect from their host star, however current technology is limited to only imaging these self luminous (and thus young) planets.(Artigau et al., 2018)

YSES is attempting to determine the frequency and type of planets that form around sun-like stars. Thus, the target stars should ideally be around 1 $M_\odot$. This gives three clear criteria for target selection, as the target stars should all be: (1) approximately 1 $M_\odot$, (2) relatively young, and (3) not too far from Earth.

One such place a large group of young stars can be found is in OB associations. These are unbound "moving groups" of recently formed stars which share a common origin and age.(de Zeeuw et al., 1999) They are so named due to the high concentration of the massive, bright O and B type stars in such groups. The closest such group is the Scorpius Centaurus association (Sco-Cen). The existence of the Sco-Cen group was first proposed in Kapteyn (1914) and subsequently confirmed by other astronomers

---

[1]First ever image of a multi-planet system around a Sun-like star: `https://www.eso.org/public/images/eso2011b/`, accessed 2022-08-21

of the era. Since then it has been examined widely, most notably by de Zeeuw et al. (1999), who were the first to confirm the membership of less massive, sun-like stars within the group. More recently the group has been extensively studied in a number of papers by Pecaut and Mamajek (2010, 2016), who focused specifically on low mass members of the association.

Sco-Cen has three sub-groups: Upper Scorpius, Upper Centaurus–Lupus, and Lower Centaurus–Crux (LCC). Of the three, LCC is the closest, with the member stars having a mean distance of about 118 pc.(de Zeeuw et al., 1999) The LCC subgroup is the oldest of the three, but is still young with a median age of 17 Myr.(Pecaut and Mamajek, 2010) Thus, LCC represents a perfect selection of young, nearby stars.

The YSES targets are drawn from this group of stars, and consists of 70 stars in LCC which are all K-type stars with masses ranging from 0.8-1.2 $M_\odot$, ages from 0-20 Myr, and a median distance of 112 pc.(Kenworthy et al., 2021) All of the stars were identified as members of the LCC subgroup by Pecaut and Mamajek (2016).

3.3. YSES Methodology

YSES takes a new approach to finding planets with direct imaging. Whereas most other surveys use long integration times(Nielsen et al., 2019; Zhang et al., 2020), YSES uses a "snapshot" method: they have a total integration time of only roughly five minutes per observation per star.(Bohn et al., 2021) All the targets were observed with SPHERE on the VLT (which is discussed in more detail in Chapter 4). Each target is observed twice, with each observation about a year apart, so that the common proper motion of the companions with their host star can be used to differentiate them from background objects.(Bohn et al., 2021) In this way, this survey has an improved efficiency compared to others by increasing the number of detections per hour of telescope time.

The YSES team primarily uses the IRDIS instrument for their observations, which can image together with the IFS (as will be explained in Chapter 4). The IFS images are what is being used for this thesis. However, the IFS was not turned on for the first epoch of YSES observations. Thus, only the second epoch observations can be used. The survey is still waiting on more telescope time to complete the observations, and only 37 of the 70 target stars have been imaged for the second epoch.

This makes up the complete dataset used for the thesis: a set of 41 IFS observations of 37 different K-type stars located in LCC.

<div align="right">

4

</div>

Instrumentation

All of the targets for YSES were observed using SPHERE, an extreme AO and coronagraphic system which is installed on the Nasmyth platform of the VLT. A picture of the outside of the system can be found in Figure 4.1. The system is specifically designed to enable direct imaging of exoplanets. It consists of three instruments and the common path which feeds all of them. The Common Path Infrastructure (CPI) will be described in Section 4.1, followed by information about the science instruments. Only the IFS will be used for the thesis work, however all three will be briefly touched upon. The Zurich IMaging POLarimeter (ZIMPOL) is examined in Section 4.2, then the InfraRed Dual-band Imager and Spectrograph (IRDIS) in Section 4.3. Finally the Integral Field Spectrograph (IFS) will be described in Section 4.4.

Figure 4.1: Picture of SPHERE on the VLT. The location of each of the instruments is labeled. Adapted from ESO instrument description.[1]
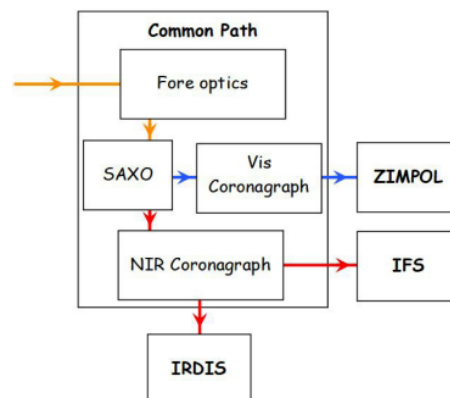
Figure 4.2: Block diagram of SPHERE, showing the main parts of the CPI and how they connect to each of the instruments. Orange beams represent VIS+NIR light, Blue is only VIS, and Red is only NIR. Taken from Beuzit et al. (2019).

4.1. CPI

CPI is the common path and infrastructure, which is the optical elements that are common to all the instruments. A block diagram of SPHERE can be found in Figure 4.2, which shows the main parts of the CPI and how they feed to the science instruments. Each of the four main elements from the CPI will be discussed in a subsection below. The full layout of the CPI with most of the components labeled is shown in Figure 4.3.

---

[1]SPHERE: `https://www.eso.org/sci/facilities/paranal/instruments/sphere.html`, accessed 2023-11-15
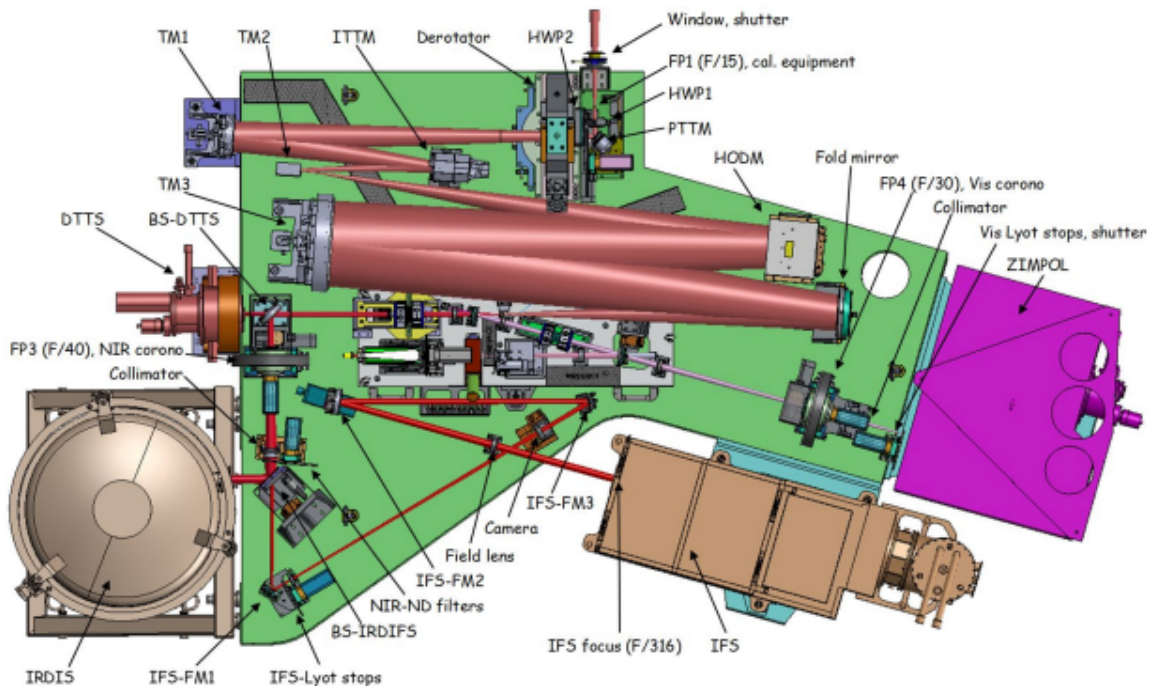
Figure 4.3: Layout of the CPI for SPHERE, with various components marked. Taken from Beuzit et al. (2019).

4.1.1. Fore optics

The fore optics mainly serve to stabilize and to focus the incoming light into the instrument. Near the beginning of the instrument is the de-rotator, which corrects for the rotation of the Earth as observations are being made. This can be set to either pupil or image stabilization.(Beuzit et al., 2019) A series of several toroidal mirrors focus the light onto the various elements of the adaptive optics system, SAXO (Sphere Ao for eXoplanet Observation), which will be explained below.

After the adaptive optics system, the light is split using a dichroic beam splitter, and the VIS light is sent to the wave front sensor (WFS) and ZIMPOL, while the NIR light is sent to IRDIS and IFS.

4.1.2. SAXO

SAXO is the extreme AO system of SPHERE. Adaptive optics is used to correct for the effects of atmospheric turbulence in order to achieve as clear a picture as possible. A block diagram of the main components of SAXO and the control loops can be found in Figure 4.4. A beam splitter sends part of the visible light to ZIMPOL and part to the WFS, or all of the light to the WFS if ZIMPOL is not in use.(Beuzit et al., 2019)
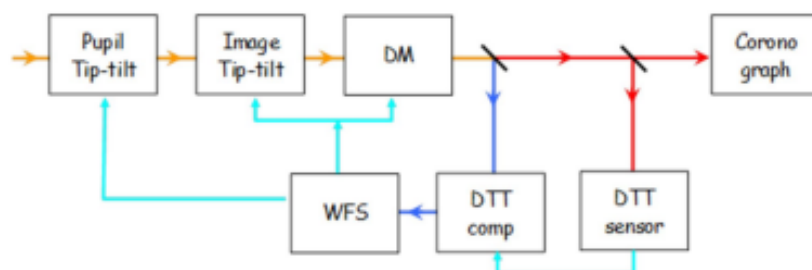
Figure 4.4: Block diagram of the AO components and control loops of SPHERE. Orange beams represent VIS+NIR light, Blue is only VIS, Red is only NIR, and Light Blue is for the control loops. Taken from Beuzit et al. (2019).

The WFS utilized by SPHERE is a spatially filtered Shack-Hartmann sensor.(Fusco et al., 2016) This sensor works by using a number of subapertures with the same focus, which are focused onto the sensor. Measuring the gradient of the wavefront across the sensor allows for measuring the error, which can be used for reconstructing the aberrations. The spatial filtering is done using a stop which blocks the higher-order spatial frequencies.(Poyneer and Macintosh, 2003) This stop is adjusted based on the atmospheric conditions.(Fusco et al., 2016)

The WFS communicates the necessary corrections to the deformable mirror, which uses its 41x41 actuators to correct for phase perturbations, while image tip-tilt errors are corrected by the image tip-tilt mirror, and pupil tip-tilt errors by the pupil tip-tilt mirror.(Fusco et al., 2016) There is an additional control loop for fine centering of the IR coronagraph, using a separate differential tip-tilt sensor and tip-tilt mirror.(Fusco et al., 2016)

All of this put together allows for vastly improved performance of the instruments, and enables it to reach a Strehl Ratio of >0.9 in the H band.

4.1.3. Coronagraphs

SPHERE has multiple options for coronagraphs, both for VIS for ZIMPOL and for NIR for IRDIS and IFS. The YSES observations made use of the apodized pupil Lyot coronagraph (ALC), so that is the one that will be discussed here.(Bohn et al., 2021) Coronagraphs are used to block the light of a bright, on-axis point source, in this case the central star, improving sensitivity to faint off-axis sources, such as disks or planets.(Sivaramakrishnan et al., 2001) A classical Lyot coronagraph has an occulting mask which blocks out the central light, followed by a Lyot stop, which further reduces any stray light that bends around the occulter.(Sivaramakrishnan et al., 2001) An ALC adds an apodizer at the entrance pupil, which helps to further reduce diffraction wings, thus improving the performance.(Carbillet et al., 2011) A diagram of an ALC can be found in Figure 4.5.
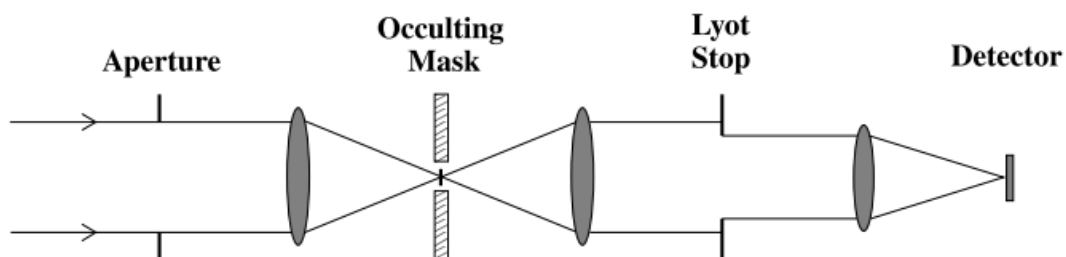
Figure 4.5: Diagram of a classical Lyot coronagraph. For an ALC, an apodizer would be added at the aperture. Taken from Sivaramakrishnan et al. (2001).

4.2. ZIMPOL

ZIMPOL is the imaging polarimeter of SPHERE. As the young planets YSES is targeting largely emit in IR and not in VIS, this instrument is not utilized by the YSES team.(Marley et al., 2007) As this instrument is only tangentially related to the thesis work, it will only be described very briefly here. ZIMPOL can be used to measure the polarization of light, or to image in the visible spectrum. It has a fairly narrow field of view (FOV) of only 3.5"x3.5", so it is used to look very close in to nearby stars.(Thalmann et al., 2008) The polarimetry can be used to look at the polarized light which is reflected off a protoplanetary or debris disk.(Thalmann et al., 2015)

4.3. IRDIS

IRDIS is the InfraRed Dual-band Imager and Spectrograph. IRDIS provides classical imaging (CI), dual-band imaging (DBI, where two images are made simultaneously in two neighboring filters), long-slit spectroscopy, and differential polarimetric imaging (where two images are made simultaneously

with different polarization directions).(Dohlen et al., 2008) It has a wavelength range of 0.95–2.4 μm over a wide FOV of 11"x11" in imaging.(Beuzit et al., 2019) The YSES observations (in particular those of the YSES 1 and 2 systems) primarily make use of both the CI and DBI modes, so both modes will be discussed here.(Bohn et al., 2021, 2020a,b)

The layout of IRDIS with the most important components labeled can be found in Figure 4.6.
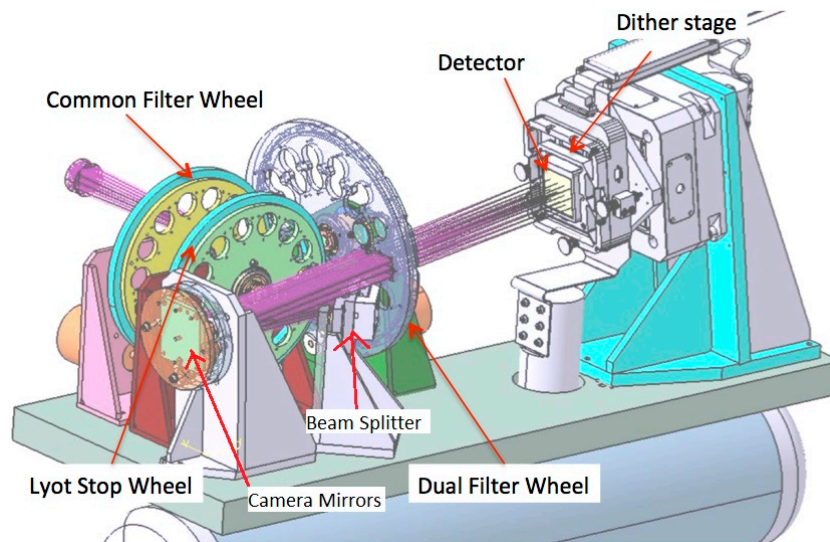
Figure 4.6: IRDIS layout. Adapted from ESO instrument description.[2]

4.3.1. CI
The CI mode can image in the Y, J, H, and Ks bands. There are two possible filters: narrow-band, which images over a narrower wavelength range, but with a higher spectral resolution of R=70–80; and broadband, which is over a wider range, but with a lower resolution of R=5.(Beuzit et al., 2019) The YSES observations all use the broadband filter, imaging primarily in both the H and Ks bands.(Bohn et al., 2021, 2020a,b). This mode has a contrast of 10^{-4} at 0.1", and 3×10^{-4} at 0.5" separations.(Beuzit et al., 2019)

4.3.2. DBI
DBI is the main mode for IRDIS, and is specifically designed for detecting planetary mass companions. In this mode, the beam is split into two parallel beams, which are filtered with two different neighboring filters before each being imaged on one half of the detector. These filters are optimized to be centered around features that are expected to be sharp in the expected planet spectra based on models.(Beuzit et al., 2019) The various filter pairs are listed in Table 4.1. This mode has a contrast of 10^{-4} at 0.1" and 10^{-5} at 0.5", which is only slightly better than the contrast for CI. An example of an image taken with DBI in various phases of the data reduction process can be seen in Figure 4.7.

This mode allows for imaging the same object with IFS in parallel. A dichroic beam splitter sends some of the light to IRDIS and some to IFS depending on the wavelength. This will be explained more in Section 4.4. The YSES observations have made use of the DBI mode in both H and K bands.(Bohn et al., 2021, 2020a,b)

---

[2]SPHERE instrument description: `https://www.eso.org/sci/facilities/paranal/instruments/sphere/inst.html`, accessed 2023-11-15

Table 4.1: Filter pairs for IRDIS DBI. From Vigan et al. (2010).

Pair name	Filter 0		Filter 1	
	λ_0 (μm)	R_0	λ_1 (μm)	R_1
Y2Y3	1.020	20	1.073	20
J2J3	1.190	25	1.270	25
H2H3	1.587	30	1.667	30
H3H4	1.667	30	1.731	30
K1K2	2.100	20	2.244	20

(a)   (b)   (c)   (d)
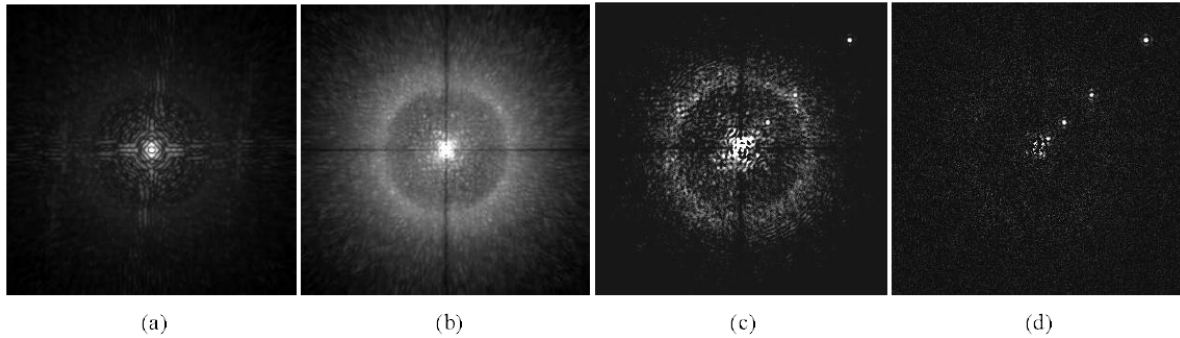
Figure 4.7: Example of an image taken with IRDIS DBI in various steps of the science reduction. "M0V star 10pc image with DBI (H2H3), the detected planets are located at 0.1", 0.2", 0.5", 1", 2" from the star and correspond to : 1MJ at 10My - 3MJ at 100My - 11MJ at 1Gy - 25MJ at 5Gy. The illustrations show the star PSF (a), the 4QPM raw image (b), the 4QPM single subtraction of 2 wavelengths H2H3 (c), the double subtraction image including calibration of differential aberrations and chromatic residual (d). Gray scales are arbitrary." Image and caption taken from Dohlen et al. (2008).

4.4. IFS

IFS is the integral field spectrograph of SPHERE. It provides low resolution spectroscopy over a very narrow FOV. The opto-mechanical layout of the instrument is shown in Figure 4.8. This is the instrument that will be utilized for the thesis work, so it will be discussed in detail.

4.4.1. Instrument Description

IFS allows for taking images in a full range of wavelengths at once. It does this by utilizing an Integral Field Unit (IFU) which consists of a grid of 122x122 hexagonal lenslets which cover the full FOV. Each lenslet acts as its own slit for spectroscopy, dispersing the light received by that lenslet onto the detector.(Claudi et al., 2006) The lenslets are rotated by $10.5°$ with respect to the detector, allowing for longer spectra. These hexagonal lenslets with the spectra projected onto them can be seen in Figure 4.9. Each of the spectra are 35 pixels long, with a separation of about 5 pixels from the nearest spectra in each direction.(Antichi et al., 2009) A close up of these spectra in an unreduced image can be seen in Figure 4.10.

The detector itself is a 2kx2k Hawaii 2RG array. It has an efficiency of around 96% in the J and H bands.(Claudi et al., 2008) To reduce the thermal noise, the detector is cooled to 80K, and a filter is used to block all wavelengths of light not being imaged by IFS (above 1.35 or 1.68 μm, depending on the mode).

IFS has a narrow FOV of 1.73"x1.73", but allows for high contrast at small separations. IFS can image in two modes: a Y–J mode imaging from 0.95–1.35 μm and a Y–H mode from 0.95–1.68 μm. The Y–J mode has a spectral resolution of about 50, whereas the Y–H mode only has a spectral resolution of about 30, but allows for better contrast. Utilizing a dichroic beam splitter, both modes can be used in parallel with IRDIS DBI: IRDIS images in H (H2H3 or H3H4) while IFS images in Y–J, or IRDIS images in K (K1K2) while IFS images in Y–H. Under ordinary observing conditions, IFS has a contrast of 10^{-6} at 0.5".(Beuzit et al., 2019) The observations analyzed for the thesis are in the Y–J band.
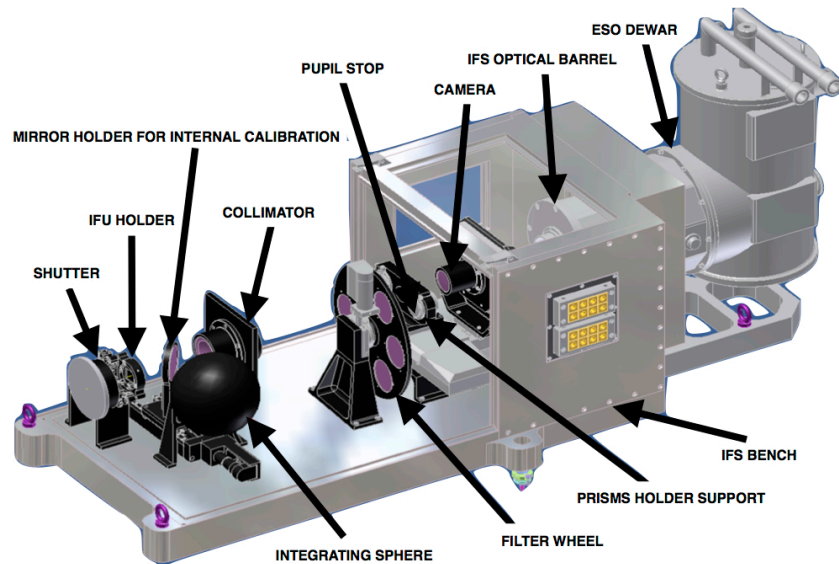
Figure 4.8: IFS layout. Taken from ESO instrument description.[3]
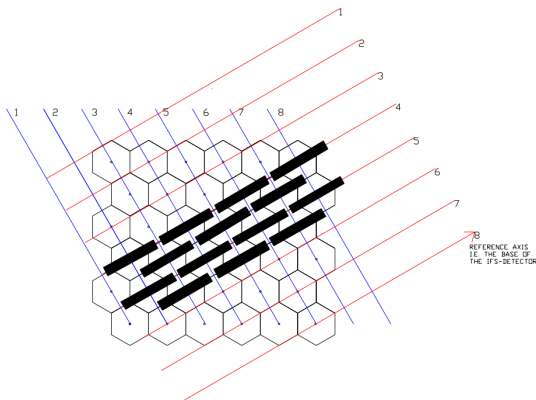
Figure 4.9: Hexagonal lenslet array with spectra projected onto them. The numbered lines represent the orientation of the detector. Taken from Claudi et al. (2006).
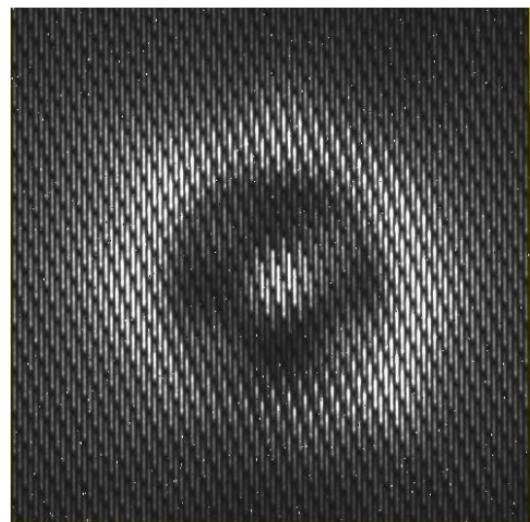
Figure 4.10: Close up of spectra in science image prior to data reduction. Taken from Mesa et al. (2015).

4.4.2. Instrument Calibration

IFS has a number of internal calibration sources used to calibrate the instrument. Proper calibration is necessary to ensure observations are of the best possible quality. Calibration also produces many files which are necessary for the data reduction process as will be explained in Chapter 5.

On the CPI there are a number of calibration sources. There are a number of lamps used to measure the throughput of the optical components. There are also four lasers with wavelengths of 0.9877, 1.1237, 1.3094, and 1.5451 μm. These produce four evenly spaced lines in the spectra, and allow for determining the wavelength which lands on each pixel of the detector, which is necessary for extracting the spectra.(Beuzit et al., 2019)

---

[3]SPHERE instrument description: `https://www.eso.org/sci/facilities/paranal/instruments/sphere/inst.html`, accessed 2022-07-07

On the IFS bench itself there are an additional five calibration lamps: one white light lamp as well as four narrow band lamps. The narrow band lamps have $\lambda_c = 1.0, 1.2, 1.3$ and 1.5 μm respectively, and each has a FWHM of 0.01–0.04 μm. There is also an integrating sphere, which is used to spread the light of the lamps evenly over the detector. These sources are located after the IFU and are used to calibrate the detector itself by making detector Flat Fields (FF) and checking the FF dependence on wavelength. As these sources are internal to IFS they can be used at the same time that IRDIS is being calibrated, saving time on the calibration procedures.(Desidera et al., 2008)

During the observations with the coronagraph (ideally immediately before and after the science observations), both flux and star center calibration observations should be made. The flux observation measures the peak flux of the star by placing it to the side of the coronagraph; this ensures accurate relative photometry. The star center observation applies a special waffle pattern on the DM, which will show up in the image. This ensures that the final science image can be centered on the star, so that the precise position of any companions can be measured.[4]

A number of other calibrations are performed by the observatory staff during the day, usually directly following the science observations. These can then be used to help process the science images. A list of which calibrations are performed for IFS is given in Table 4.2.

Table 4.2: IFS calibrations. The matching parameters list which variables for the calibration must match the science observation. Examples of some of the resulting calibration images are shown in Figure 5.1. Information from SPHERE user manual.[5]

Calibration	Matching parameter(s)	Validity
Dark	DIT	1 day
Lamp Flat	Prism	1 week
Wavelength calibration	Prism	1 week
Spectra registration	Prism	1 day
Distortion map	Filter (+dichroic), Coronagraph combination	1 week

4.5. Comparison of IRDIS and IFS

The YSES survey has made use of both the IRDIS and IFS instruments. For this thesis, only the data from the IFS will be analyzed. However, it is useful to compare the instruments and their capabilities. Figure 4.11 shows images from IFS and IRDIS taken at the same time side by side. These are of HD 114174, a sun-like star with a white dwarf companion, which is used as a photometric calibrator for the SHINE survey.(Beuzit et al., 2019) The IFS image was processed using angular differential imaging (ADI) and spectral differential imaging (SDI, both together ASDI), while the IRDIS one only used ADI.

The companion is much more clearly visible in the IFS image. This is due to the improved contrast of IFS compared to IRDIS. The contrast curves for this target for both instruments are shown in Figure 4.12. IFS has a full order of magnitude better contrast than IRDIS (IFS: 10^{-6} at 0.5", IRDIS: 10^{-5} at 0.5" with DBI). However, IRDIS has a much wider FOV of 11"x11" vs. IFS with only 1.73"x1.73". This means IRDIS can detect ultra wide orbit companions that are not in the IFS FOV.

IRDIS and IFS can image together in different wavelengths: IRDIS imaging in H while IFS images in Y–J, or IRDIS imaging in K while IFS images in Y–H. This extends the spectral information, allowing better characterization of any targets. IFS itself provides low resolution spectra of all objects it images. This gives a lot of extra information about the companions without needing to perform follow-up observations. Additionally, this spectral information allows for using SDI, which can be very helpful to reveal companions hidden in the stellar halo (as will be explained in more detail in Chapter 6). The spectral

---

[4]   SPHERE   user   manual: `https://www.eso.org/sci/facilities/paranal/instruments/sphere/doc/`
`VLT-MAN-SPH-14690-0430_v96.pdf`, accessed 2023-11-15
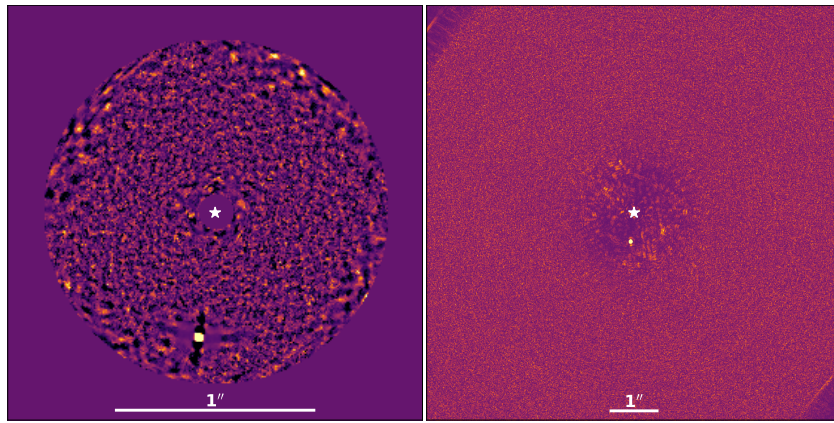
Figure 4.11: IFS (Y–J, left) and IRDIS (H2 filter, right) images of HD 114174 using ASDI/ADI. The IFS image has much better contrast, but IRDIS has a much wider FOV. Taken from Beuzit et al. (2019)
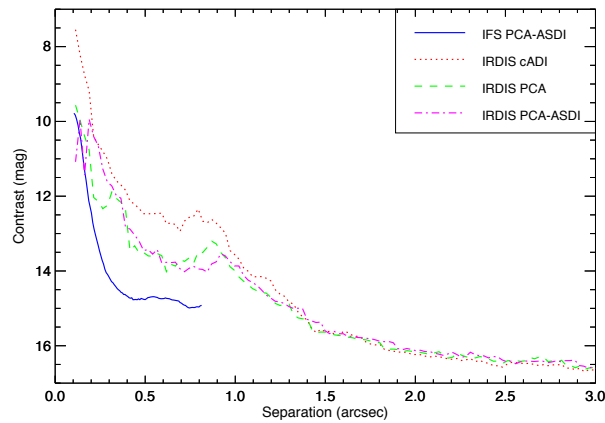
Figure 4.12: 5σ contrast curves for IFS (Y–J) and IRDIS (DBI H23) for HD 114174 using ASDI/ADI. IFS clearly performs better than IRDIS at small separations. Taken from Beuzit et al. (2019).

information can help to determine the mass of any potential companions, which will be explained in Section 7.3.

IRDIS and IFS are both complementary and are very strong together. However, IFS should be much better than IRDIS at detecting companions that are closer in to their host star. Thus, analyzing the IFS data may reveal smaller and fainter companions that were missed in the analysis of the IRDIS images.

Part II

Methods

5

Reduction

In order to analyze the images in the dataset, they must first be reduced. Reduction is the process of removing the instrument signature and noise sources such that the signal of the target can be retrieved.(Freudling et al., 2013) The data reduction can sometimes be used to refer to the science reduction steps, including differential imaging and other post-processing techniques. Here data reduction is used to mean only the pre-processing: the basic steps performed on any image from the instrument in order to prepare it for further analysis. The post-processing will be discussed in Chapter 6.

To perform this basic data reduction the automatic reduction pipeline provided by ESO, ESO Reflex, will be used in combination with the SPHERE reduction Python package by Arthur Vigan.(Freudling et al., 2013; Vigan, 2020) This package allows for writing and executing ESO Reflex recipes in Python.

The IFS can be tricky to work with as the science image presents both the spatial and spectral information together. The spectra must be extracted to go from a 2D image to a 3D (x, y, λ) data cube. Various noise sources must also be removed to improve the image quality. This reduction follows a number of different steps, the most important of which will be explained here.(Desidera et al., 2008)

Data Organization
The first step is to organize the data, including collecting the data from ESO. Each separate observation is downloaded from the ESO portal, packaged together with the necessary calibration files. Then all of the files are assessed and categorized according to their purpose. The science files are separated from the various calibration files. All the files are prepared such that the following steps can access the necessary files.

Master Dark
During calibration several "darks" are made by reading out the detector with no light on it. This gives the thermal background noise which can be subtracted later. An example of a dark frame is shown in Figure 5.1a. The dark needs to have the same exposure time as the science image.

Bad Pixel Map
The dark is combined with the detector flat field (an image made with a white lamp shining on the detector, see Figure 5.1b) to create a bad pixel map. This shows the location of all the bad pixels on the detector, so that they can be removed later.

Wavelength Calibration Map
The external calibration sources include four lasers, which, when imaged on the IFS, produce four distinct lines in the spectra. Interpolating between these four wavelengths allows for determining which
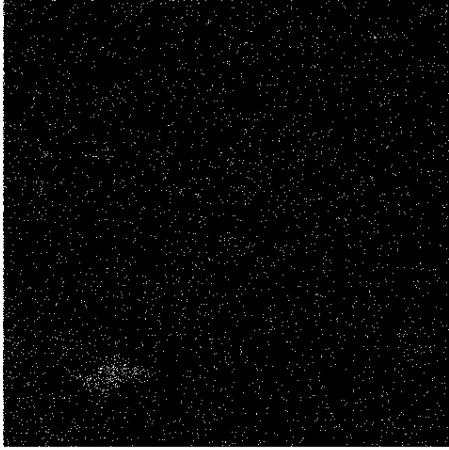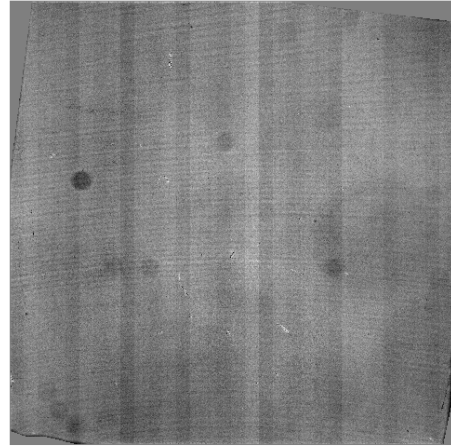
Figure 5.1: Example of frames used for calibrating IFS.

wavelength is on which pixel. This is used to create a map of where the spectra appear to aid in extracting them.

Corrections
The bad pixel map and the dark are subtracted from the science image to remove the effects of thermal noise and bad pixels.

Spectrum Location
The spectra can appear at slightly different positions in the science image, so they must be located in the image. The position of the spectra can be measured on the detector using cross-correlation. A spectrum position map is created which shows the position of each spectra from each lenslet. An example of this map can be found in Figure 5.2.
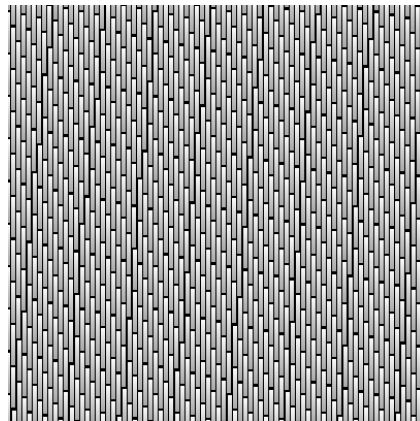
Figure 5.2: Example of a spectra position map. The image is zoomed in to show the lines more clearly. Taken from example data included with ESO REFLEX.(Desidera et al., 2008)

Spectrum Extraction
Now that the spectra position map has been constructed and the major noise has been removed, the spectra can be extracted from the image. 39 wavelength slices are created and filled with all the pixels

of the corresponding wavelength. The science image is transformed from a single 2048x2048 image to a data cube with 39 slices of 290x290 where each slice corresponds to a certain wavelength. At this point the data cube is derotated and final, minor corrections are applied. An example of an unreduced science image and a slice of the final, reduced data cube can both be seen in Figure 5.3.
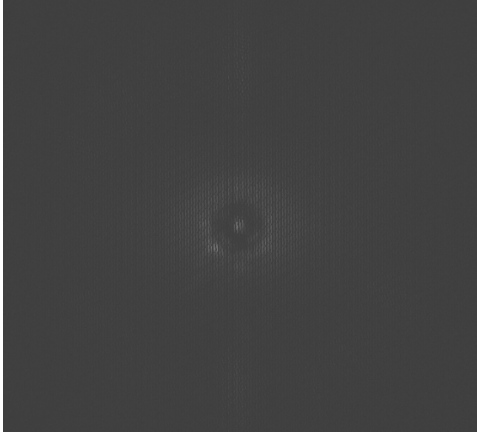
(a) Example of a science image taken with IFS before data reduction. Here the lines of the spectra are visible as they have not yet been extracted. Taken from example data included with ESO REFLEX.(Desidera et al., 2008)
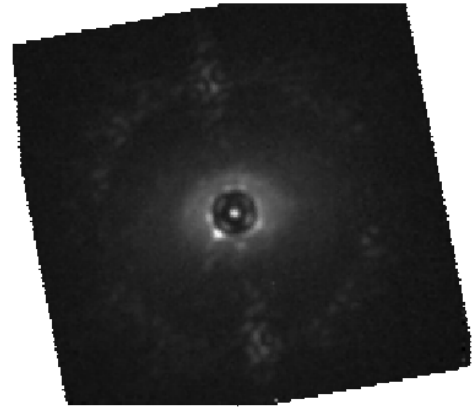
(b) Example of a single wavelength slice of a reduced IFS data cube. The lines of the spectra are gone as they have been separated out, and the stellar halo is much more clearly visible. The image is not completely square due to the offset of the IFU with respect to the detector. Taken from example data included with ESO REFLEX.(Desidera et al., 2008)

Figure 5.3: A science image before (left) and after (right) reduction.

6

Post Processing

Post-processing involves using various techniques to further subtract the light of the star and reveal any faint objects in the image. For this thesis, spectral differential imaging was used, as this works very well for IFS data. Section 6.1 will discuss how spectral differential imaging works and its limitations.

6.1. Spectral Differential Imaging

Spectral differential imaging (SDI), makes use of the spectral differences between the companion and the host star point spread function (PSF). It requires having images of the system at multiple different wavelengths. Due to diffraction, the host star PSF will increase in size proportional to $\frac{\lambda}{D}$. However the companion's position does not change with wavelength. This can be seen clearly by looking at a cube in the separation vs. wavelength space, as is shown in Figure 6.1. By scaling the wavelength slices proportional to the wavelength, now the companion moves, but the star PSF is always in the same position. Taking the median of this cube gives just the star PSF, which can be subtracted from all the slices. The slices are then scaled back down to original size, and can either be combined or left as individual slices.(Kiefer et al., 2021) This can improve the contrast of the images drastically, revealing fainter objects that could otherwise not be seen. A graphical representation of how SDI works can be found in Figure 6.2.

For this thesis, the Python package PynPoint was utilized to apply SDI to all the observations.(Stolker et al., 2019; Amara and Quanz, 2012)

6.1.1. Limitations

SDI is a very powerful tool, but it comes with a few limitations. Chief among these is the risk of self-subtraction. If the wavelength range is not broad enough then when the images are scaled by wavelength, the companion can end up still partially on top of itself. This can lead to some of the light of the companion being subtracted out. This problem becomes worse if there are multiple companions aligned radially, as the interior companion will end up on top of the exterior companion when resizing. This can be seen in Figure 6.3, which shows a cube in the λ vs. separation space before and after resizing.

Additionally, the effective FOV is reduced when performing SDI. This is because when the images are scaled, only the portion of the PSF that appears in every slice can be used. This effect can be seen in Figure 6.2. For IFS, scaling based on the longest wavelength reduces the FOV from 1.73"x1.73" to 1.22"x1.22" for Y-J band, or 1.00"x1.00" for Y-H.(Kiefer et al., 2021)
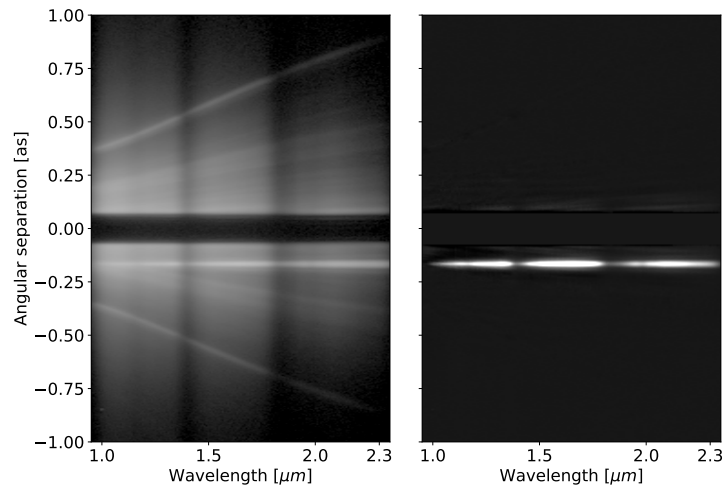
Figure 6.1: Slice of data cube showing intensity for wavelength vs angular separation. The dark portion around +/-0.1" is from the coronagraph. The bright horizontal line at around -0.2" is a companion. The left image is before PSF subtraction, showing how the stellar PSF increases proportional to the wavelength while the planet's position is constant. The right image shows after subtraction, leaving only the light of the planet. Taken from Beuzit et al. (2019).
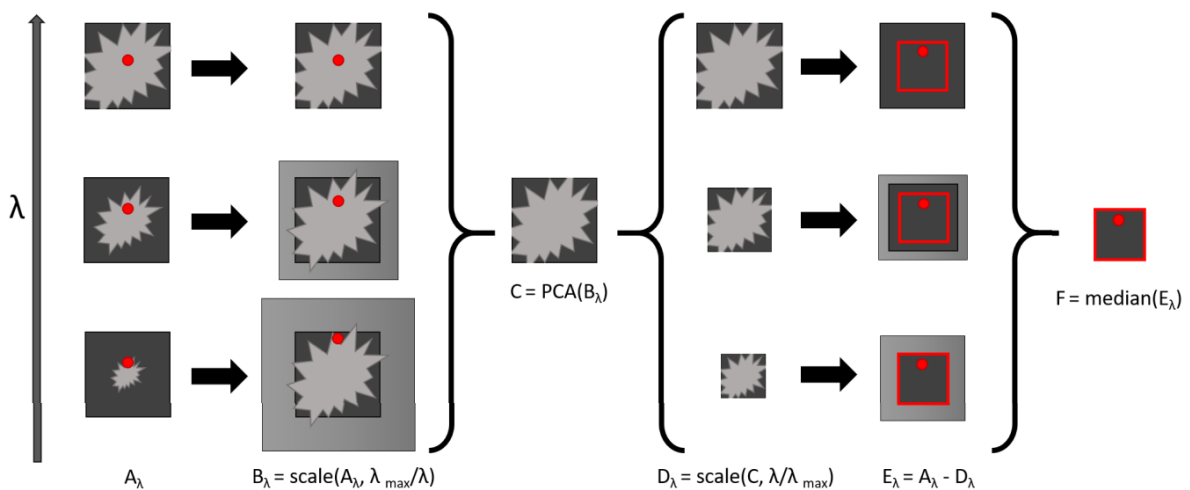
Figure 6.2: Graphical representation of the SDI technique. Taken from Kiefer et al. (2021).
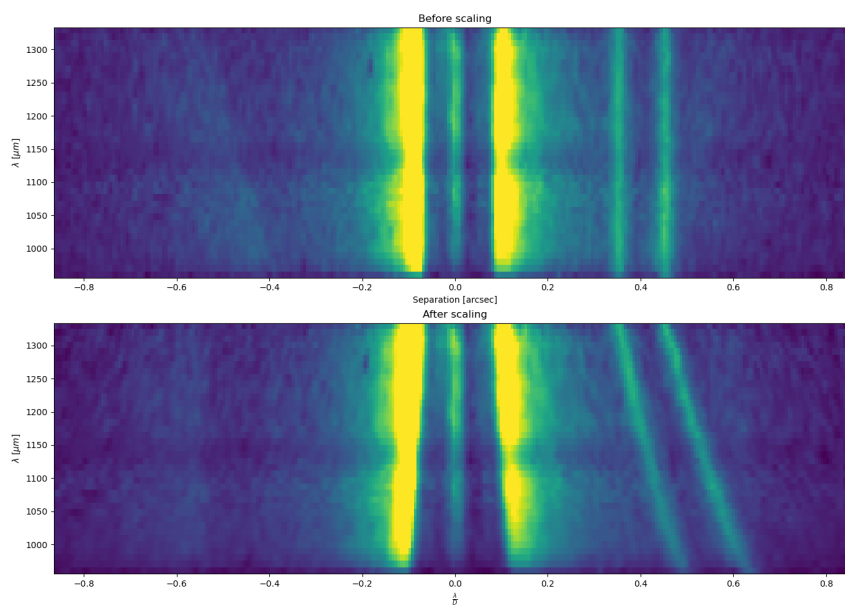
Figure 6.3: λ vs. separation slice of a data cube before and after resizing. The two vertical lines in the top image are planets that have been injected into the image at the same angle with a small separation. After resizing by wavelength, the planets are smeared out such that one planet at one wavelength ends up on top of the other planet at a different wavelength. When taking the mean or median of the resized cube, the signal from the two planets will interfere.

7

Companion Characterization

After the images have been pre- and post-processed, they can be analyzed for companions. Any candidate companions that are discovered can then be characterized to determine their key properties. In this chapter this identification and characterization process will be discussed. Section 7.1 will discuss the identification of candidate companions. Then Section 7.2 will explain how the candidates' astrometry (the precise position relative to the host star) was measured. The measurement and analysis of the candidates' spectra will be discussed in Section 7.3, as well as how this can be used to delineate between gravitationally bound companions and background objects. Finally in Section 7.4, a discussion will be made on how detection limits are computed for each system.

7.1. Companion Identification

Candidate companions are first identified visually. This is done by co-adding all the wavelength slices of the cube, which should increase the signal to noise ratio (SNR) of the companion by a factor $\sqrt{n}$ where n is the number of slices. In this case, the first two and last two slices of the cube are discarded as they are typically significantly noisier than other slices, so n is 35. Any particularly bright point sources in the images are noted to be checked further.

Each potential candidate is checked using hypothesis testing. Hypothesis testing compares the null hypothesis: that the candidate is just noise and drawn from the same distribution as the noise, with the alternative hypothesis: that the candidate is an astrophysical object, and thus drawn from a different distribution. This is done by measuring the noise at the same distance from the star as the point source and fitting a Gaussian distribution to it, then calculating the likelihood that the point source could have come from that distribution or if it is from a separate distribution.(Bonse et al., 2022) The noise distribution is corrected for any effects of small-sample statistics as described in Mawet et al. (2014). A graphical depiction of hypothesis testing can be seen in Figure 7.1. The threshold for detection is typically set at 5σ or a false positive fraction (FPF, the chance that noise will be identified as a companion) of 3×10^{-7}.(Mawet et al., 2014) This is a very conservative FPF, however this is ideal as it reduces the chance of identifying noise as a planet and wasting time and resources performing follow-up observations.(Currie et al., 2023)

Unfortunately, although hypothesis testing can do a reasonably good job of determining whether a bright point source is astrophysical or noise, it cannot determine whether the object is gravitationally bound to the host. Meaning with hypothesis testing alone there is no way to determine if an object is a true companion or if it is a background star. For this project, that was determined with the spectra, and will be explained in Section 7.3.

The measuring of the candidate's brightness and calculating the FPF was performed in Python with PynPoint.Stolker et al. (2019)
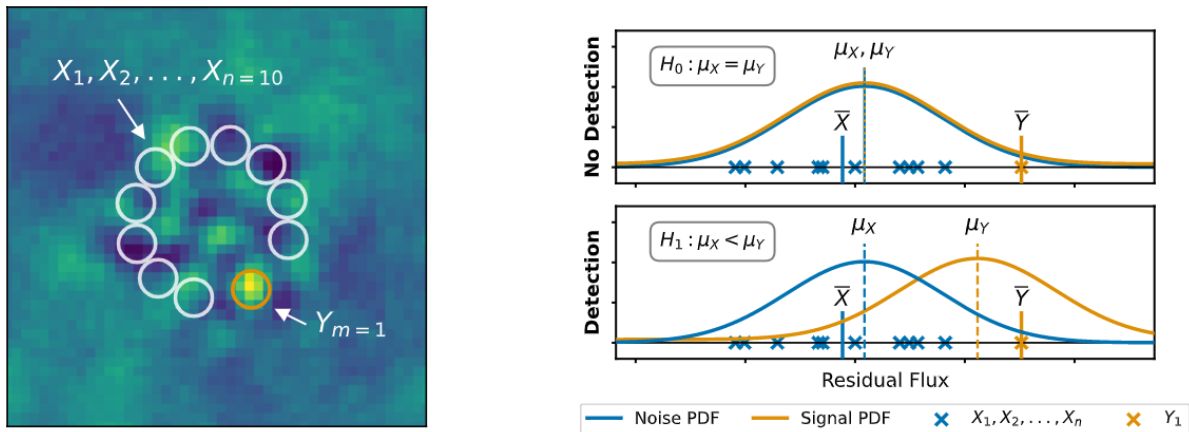
Figure 7.1: Example of hypothesis testing for direct imaging. At left is an image with a potential companion Y and all the spots X where the noise is sampled at the same distance. At right are the two different scenarios or "hypotheses": that the candidate is just noise, or that it is in fact a companion. Taken from Bonse et al. (2022).

7.2. Astrometry

Astrometry is the measurement of the precise position of an object, in this case the candidate companions relative to the host star. This is crucial so that future researchers know where to look if follow-up observations are to be made.

The airy disk of a point source (i.e. the diffraction limited PSF) is a 2D Gaussian. This fact can be used to find the position of the companions. A 2D Gaussian can be fit to the image in the region of the companion, lining up the peak of the function with the peak of the companion PSF.(Stone, 1989) In this way, sub-pixel precision can be achieved for the companion position. The fit also gives an estimation of the error on the companion position. This 2D Gaussian fitting was implemented using PynPoint.(Stolker et al., 2019)

7.3. Spectra

7.3.1. Measuring and Correcting Spectra

With a precise measurement of the companion position, the spectra can now be extracted. This is done by drawing a circular aperture around this position. The radius of this aperture was determined visually, and was set to 0.035", or roughly 5.9 pixels in the IFS images. An example of what this aperture looks like in context can be seen in Figure 7.2. The average value of all the pixels inside the aperture is then measured. This was done for each wavelength slice of the cube, giving a very low resolution spectrum of the companions.

Measurements of the noise were made at each wavelength to give a margin of error on the spectrum. This is done by measuring several noise elements in a ring around the host star at the same separation as the companion, using the same size aperture. A Gaussian distribution is fit to the noise. The mean of the noise distribution is subtracted from the companion spectrum, and the standard deviation gives the 1-sigma error on the companion spectrum. This standard deviation is corrected for any possible effects of small sample statistics (due to having too few noise elements) as described in Mawet et al. (2014). This was done using PynPoint.(Stolker et al., 2019)

As part of each SPHERE observation, the telescope is moved so that the host star is just outside the coronograph and can be imaged. This allows for comparing the photometry of the companion to that of its host star. For this purpose, the spectrum of each host star was also measured in the same way. The noise of the host star spectra is estimated by measuring the noise just outside the aperture, with a ring of apertures of the same size, and is fit with a Gaussian distribution, same as for the companion noise. This noise is used to estimate the sky background at the observation. The mean of the noise is subtracted from the host star spectrum, and the standard deviation gives an estimation of the error on
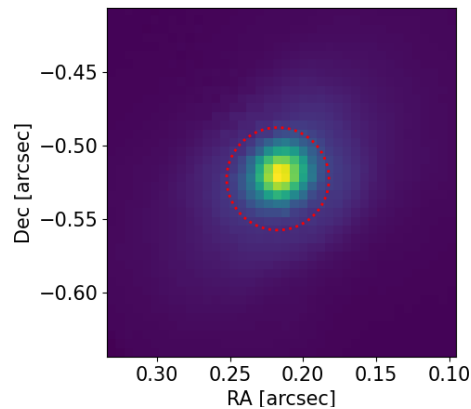
Figure 7.2: Example of the aperture used for measuring the candidate companions. The RA and Dec are measured relative to the host star.

the host star spectrum.

Due to absorption features from the Earth atmosphere, there are aberrations in the spectra which needed to be corrected (see Figure 7.3). This was done by finding a representative model of the host star and using that to correct the spectrum. Measurements of each of the host stars have been made in the past, and have noted the host star temperature.(Pecaut and Mamajek, 2016) This can be used to select the correct model. The models used were the BT-Settl spectra models from Allard et al. (2013) At each wavelength, it was determined what correction factor was necessary to map the measured host star spectrum to the model spectrum. Then these same correction factors were applied to the companion spectra to correct for the same effects.

7.3.2. Estimating Companion Type

With a low resolution spectrum of the companions, an estimation can now be made of their their temperature and thus spectral type and size. Stars and giant planets have distinct spectra corresponding to their temperature. The temperature is in turn related to mass, as larger mass stars burn brighter, and larger mass planets are heated more during formation. By comparing the measured spectrum to various models (again using the BT-Settl models from Allard et al. (2013)), and determining which fits best, an estimation can be made of the temperature or spectral type of the companion.

This fitting is done both visually and by calculating the normalized root mean square error (NRMSE) of each model vs. the candidate's spectrum. The normalization is using the mean of the candidate spectrum, so that the fit is independent of the candidate's brightness. The first and last data point of each are ignored as these are typically noisier than the rest of the data points. The BT-Settl models are available in 100K increments, and for the fitting a range of models from T_{eff} of 400K–6000K was used. All the models are with metallicity and log(g) equal to the solar values. These parameters do influence the spectra slightly, but have a much smaller effect than T_{eff}, which is the main parameter of interest.

Comparing the brightness of the companion to hypothetical model objects placed at the same distance as the host star can also provide evidence for if a candidate companion is gravitationally bound to the host star or not. If the candidate matches up very well with the models of similar brightness, this is evidence that the candidate is at the same distance as the host star, and thus likely to be gravitationally bound to it. However, if it does not match up well against models of a similar brightness, or the best fit model is significantly brighter, that suggests the candidate is likely to be an unrelated background star. Calculating the exact difference in apparent magnitude between the candidate and its best fit model allows for estimating the distance to the candidate, and thus how far behind the host star it is.
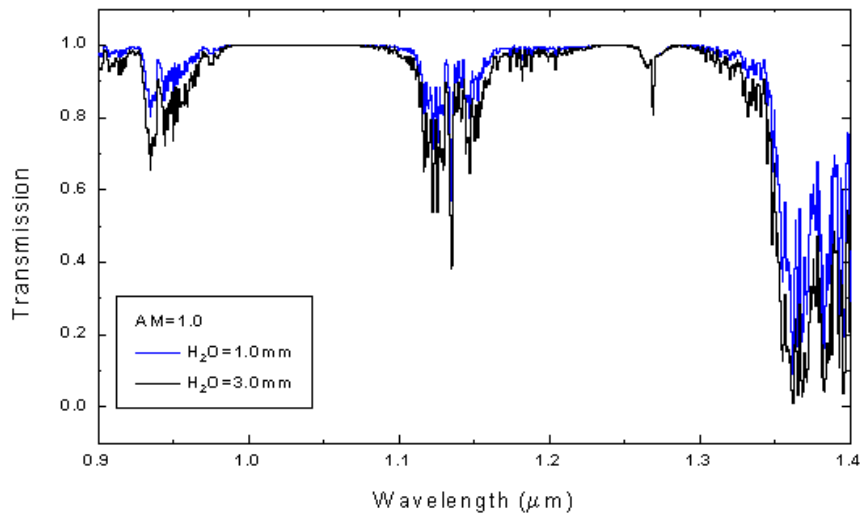
Figure 7.3: Earth atmosphere transmission in the NIR. There are clear absorption features at 0.95, 1.15, and 1.35 μm. This causes a reduction in the observed host star and planet spectra at these wavelengths, which must be corrected. Taken from Gemini Observatory.[1]

7.4. Detection Limits

Detection limits set an upper bound on how bright an object would need to be to have been found in a given observation. This is essentially the opposite of hypothesis testing (described in Section 7.1): instead of finding out if a given candidate is above a threshold, one calculates how bright a companion would need to be to be exactly at the threshold.

This is done by artificially injecting a planet into the observations, coadding the wavelength slices, and then computing the FPF of the companion. The process is iterated, adjusting the planet's brightness each time, until the FPF is close enough to the threshold of 3×10^{-7}. This must be done at a range of separations and angles to compute the detection limits in each part of the image. Here, the detection limits have been computed from just outside the inner working angle at 0.15" to the edge of the image at 0.8", in 0.05" steps. At each separation the limit is then also computed at $60°$ intervals from $0°$ to $360°$. The limits should be roughly the same at each separation, so the values at each angle are averaged to make a contrast curve with contrast vs. separation. The standard deviation of the values at each angle gives an estimate of the error on the contrast limit.

An example showing these injected planets at various positions in an IFS image can be seen in Figure 7.4.

By performing SDI just before measuring the FPF, the contrast limit can be obtained for before and after subtraction. This allows for determining how well the subtraction performed to improve the contrast.

The fake planet injected is taken from the image of a host star from one of the systems. The same fake planet is used for all the contrast curves to keep it more consistent. The observation chosen was of 2MASS J13064012-5159386 from observation 2023-06-15-2, because the host star observation was particularly clean with little noise. The brightness of the planet is measured relative to this star, by determining how many magnitudes fainter it should be.

The iterating is handled by scipy.optimize.root_scalar, which is well suited to these types of problems.

---

[1]Gemini observatory: `https://www.gemini.edu/observing/telescopes-and-sites/sites#Transmission`, accessed 2023-11-27
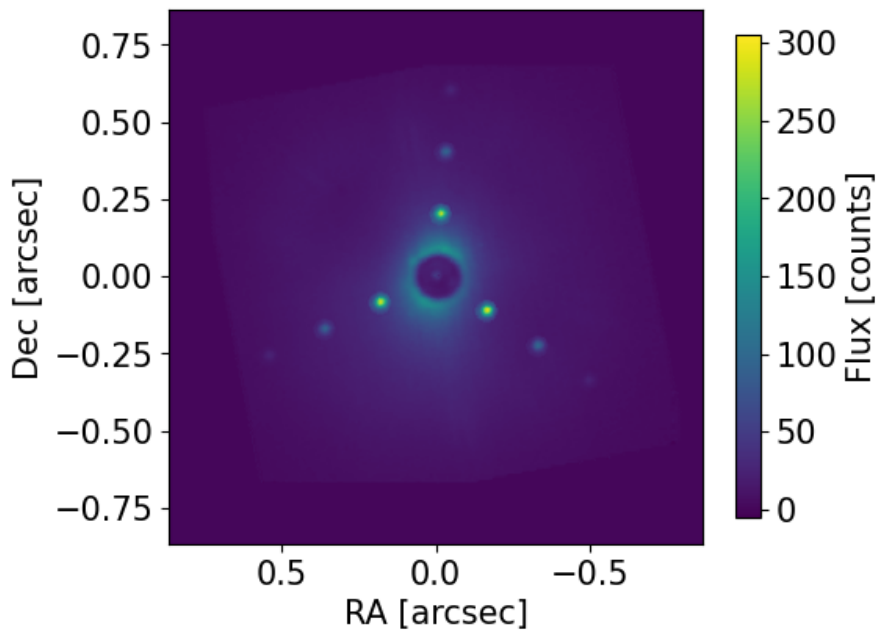
Figure 7.4: Coadded observation of 2MASS J13064012-5159386 with fake planets injected at various positions in the image. The planets shown are all exactly at the threshold for definitive detection at that position in the image.

Before subtraction the upper and lower bounds for this optimization are set to [0,10). After subtraction, the upper bound is set to the result for before subtraction at this same position (+2 magnitudes to avoid edge cases) and the lower bound is at 15; the subtraction should improve contrast, allowing fainter planets to be seen. For each separation and angle, the value from the previous run is taken as the initial guess.

Once the detection limits have been computed in terms of magnitude, this can be converted to a mass. The distance to the system and the relative magnitude of the host star can be used to compute the absolute magnitude of the injected companion at the threshold. Then using the age of the system and evolutionary models, the corresponding mass for an object of this age and brightness can be computed. The age and distance estimates for all the targets in this survey were obtained from Pecaut and Mamajek (2016) and the evolution models used were those from Phillips et al. (2020).

Converting to mass introduces a lot more uncertainty as there are additional errors on the age and distance estimates, and the evolution of low mass objects like planets is still not completely understood. However, having a mass estimate allows for better comparison of the detection limits between systems, and a better intuitive understanding of what the limits represent.

Part III

Results and Discussion

8
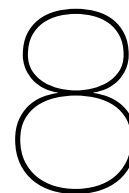
Results

This chapter presents the final results of the processing and analysis performed during this thesis. Section 8.1 discusses the reduction and subtraction steps, including identification of candidates. Then Section 8.2 will discuss each system with candidate companions one by one and the properties of these candidates. Finally the detection limits of each system will be given in Section 8.3.

8.1. Reduction and Subtraction

The first step for each cube was to download the data from the ESO portal, and then perform the reduction and PSF subtraction (here using SDI). For more details on the specifics of this process, see Chapter 5 for the reduction and Chapter 6 for the subtraction.

There were a total of 41 observations that were analyzed. Table 8.1 lists all the observations with the corresponding target. They are labeled according to the date of observation, and in cases when multiple observations were performed in the same night an additional number is added for which observation of that night it was. Three targets had repeated observations due to issues with the first observation(s); these are color coded in the table.

Careful examination of the reduced and subtracted cubes revealed a number of potential point sources in five different observations:
- 2023-05-27   2MASS J12182762-5943128
- 2023-05-30-2   2MASS J12404664-5211046
- 2023-06-15-1   2MASS J12560830-6926539
- 2023-07-26-1   2MASS J13130714-4537438
- 2023-08-07-2   2MASS J13015435-4249422

Each of these observations and the candidate companions will be discussed in detail in Section 8.2. For those systems without candidate companions, the coadded images can be found in Appendix A.

8.2. Candidate Companions

Careful examination of the resulting cubes revealed eight candidate companions in five systems. Each of the systems with candidates will be discussed here one by one, by date of observation.

For all five observations, the candidates were already bright enough before SDI, and in most cases the SDI caused a large amount of self-subtraction: especially for some of the systems where candidate companions were aligned radially, as scaling by wavelength shifts one of the companions on top of the other (see Section 6.1). Thus, it was decided to characterize the companions using the reduced cubes without SDI.

Table 8.1: All observations and corresponding targets. Repeat observations have been highlighted with the same color.

Observation	Target (2MASS J)	Observation	Target (2MASS J)
2022-12-20	12505143-5156353	2023-07-08-2	12185802-5737191
2023-01-28	10065573-6352086	2023-07-08-3	12092655-4923487
2023-03-03-1	10065573-6352086	2023-07-08-4	13065439-4541313
2023-03-03-2	10065573-6352086	2023-07-14-1	12383556-5916438
2023-04-20-1	11445217-6438548	2023-07-14-2	12374883-5209463
2023-04-20-2	11454278-5739285	2023-07-22-1	12160114-5614068
2023-05-16	13015069-5304581	2023-07-22-2	12454884-5410583
2023-05-27	12182762-5943128	2023-07-22-3	13055087-5304181
2023-05-28-1	12333381-5714066	2023-07-22-4	13334410-6359345
2023-05-28-2	12264842-5215070	2023-07-23-1	12113142-5816533
2023-05-28-3	12240975-6003416	2023-07-23-2	12472196-6808397
2023-05-30-1	12405458-5031550	2023-07-23-3	13095880-4527388
2023-05-30-2	12404664-5211046	2023-07-23-4	13335481-6536414
2023-05-30-3	12391404-5454469	2023-07-26-1	13130714-4537438
2023-06-15-1	12560830-6926539	2023-07-26-2	13444279-6347495
2023-06-15-2	13064012-5159386	2023-08-07-1	12483152-5944493
2023-06-16	13334410-6359345	2023-08-07-2	13015435-4249422
2023-06-17-1	12210808-5212226	2023-08-07-3	13343188-4209305
2023-06-17-2	12195938-5018404	2023-08-07-4	13444279-6347495
2023-06-17-3	12192161-6454101	2023-08-20	12205449-6457242
2023-07-08-1	12210499-7116493		

8.2.1. 2023-05-27: 2MASS J12182762-5943128

An image of the coadded cube of this observation before and after subtraction can be seen in Figure 8.1. There are two candidate companions. The first (referred to as candidate or companion "1") is at a separation of 0.61", and an angle of 271° (measured counterclockwise from north); it is around one magnitude fainter than the host star. The second candidate (candidate or companion "2") is at a separation of 0.644" and angle of 278°, and is slightly fainter at 1.5 magnitudes less than the host star.

The SNR of these two candidates is shown in Figure 8.2. Candidate 1 has an FPF of 1.72e-24, and for candidate 2 this is 2.58e-10. This puts both of them well above the detection threshold of 3e-7. This means that these point sources are real astrophysical objects. However it does not prove that they are gravitationally bound to the host star. To test this the next step is to look at the spectra.

Figure 8.3 plots the spectra of the two candidates alongside the spectra of the host star and various representative models. These spectra have been corrected for the earth atmosphere by adjusting the host spectra to match up with the corresponding model, and adjusting the candidate spectra the same way. One notable thing is that the spectra of the two candidates have almost identical shapes, and candidate 1 is about twice as bright as candidate 2: 1.8 times brighter to be exact. This suggests that candidate 1 may be an unresolved binary which forms a triple system with candidate 2. This would explain how it can be twice as bright but be the same kind of object. The best fit spectra for these two (displayed in Figure 8.4) also shows that they are similar types, although candidate 1 is potentially hotter which could also explain the difference in brightness. These are the two possible hypotheses: that candidate 1 is an unresolved binary and this is a triple system, or that candidate 1 is just brighter than candidate 2.

The difference in brightness between the best fit models is much larger than between the candidates (after adjusting for 1 being a binary), as can be seen in Figure 8.5. This would suggest the triple system hypothesis, as this can only be explained by the fits being incorrect (due to noise or other issues), by candidate 1 being an unresolved binary, or by candidate 2 being around 10pc further away than candidate 2 (which is unlikely). The NRMSE of the candidates compared to each other is 0.027, which is comparable to the error of the companions with their respective best fit spectra. This does not lend much support to either hypothesis.
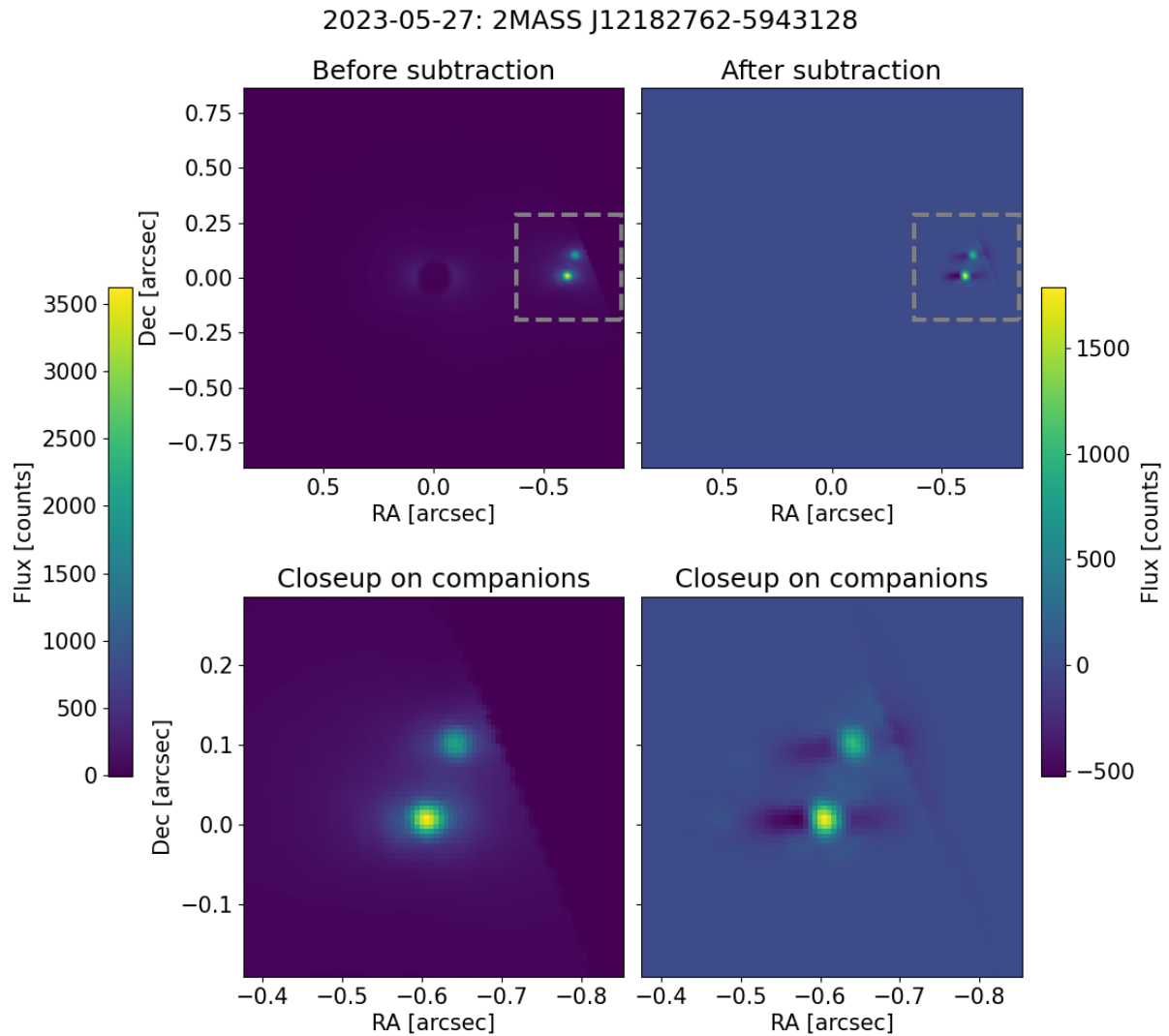
Figure 8.1: Observation of 2MASS J12182762-5943128 (2023-05-27) with SPHERE/IFS before (left) and after (right) SDI. There are two point sources in the images, which are shown in more detail in the second row. The images are rotated such that north is up and east is left.
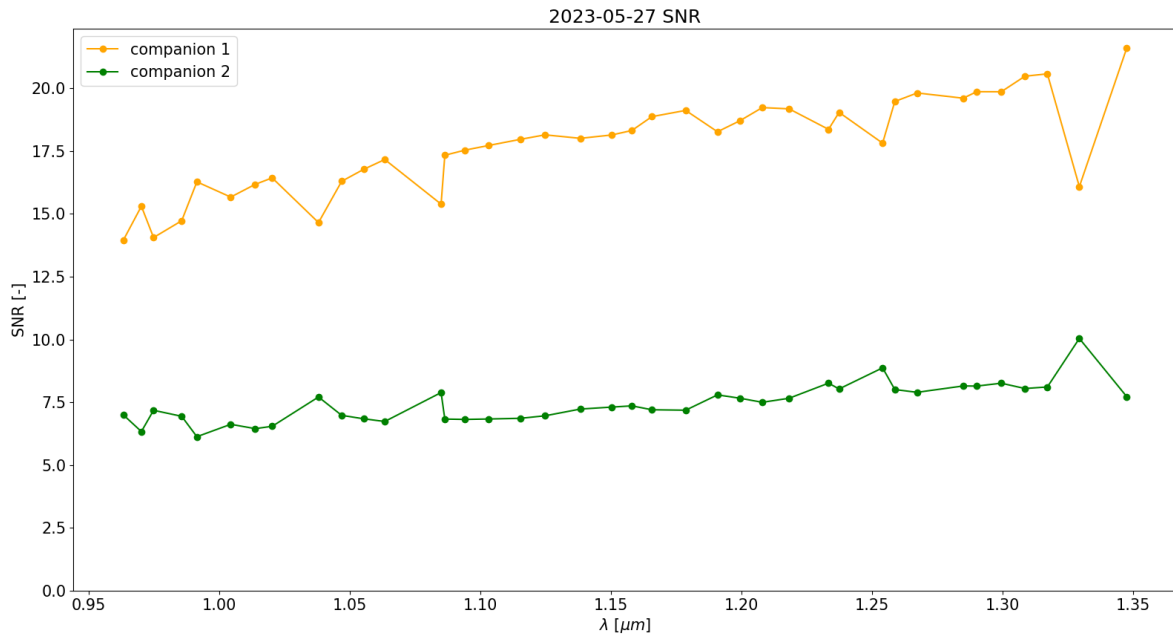
Figure 8.2: SNR of candidate companion to 2MASS J12182762-5943128 (2023-05-27) vs λ.
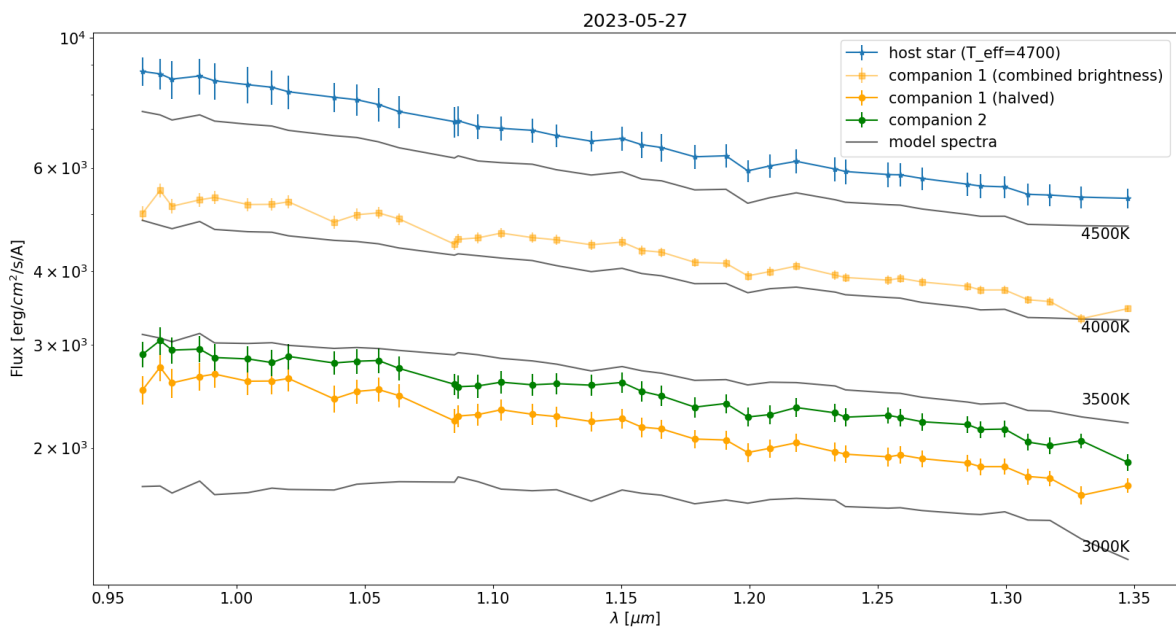
Figure 8.3: Spectra of candidate companion to 2MASS J12182762-5943128 (2023-05-27) with model spectra of various temperatures.
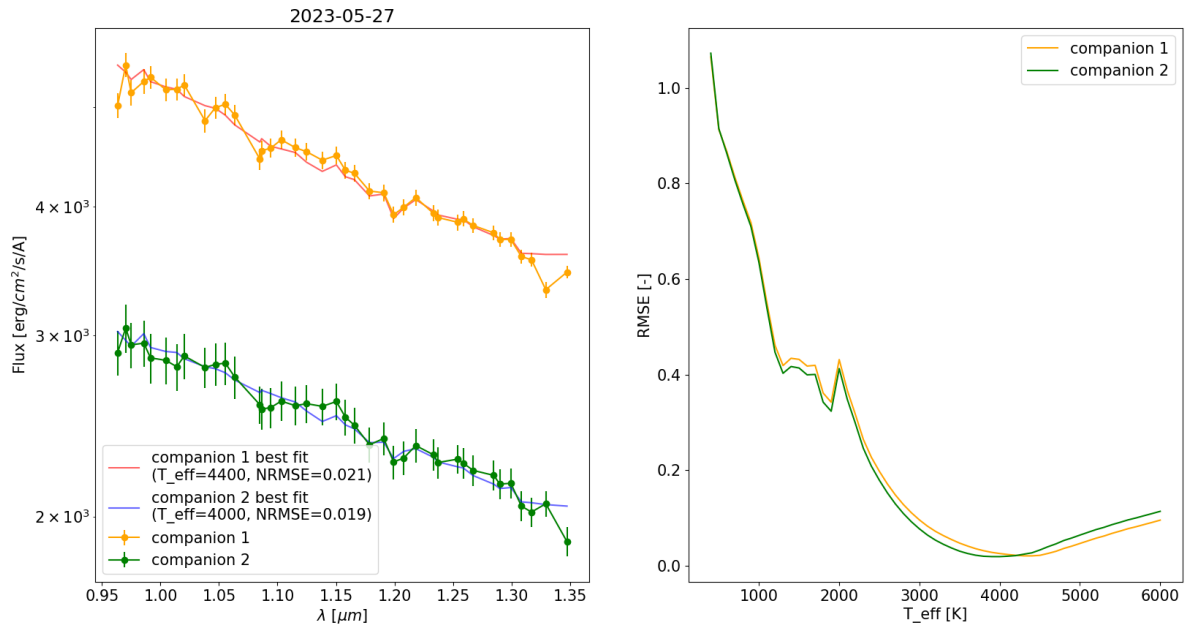
Figure 8.4: Best fit spectra for the candidate companions to 2MASS J12182762-5943128 (2023-05-27). Left shows the spectra and the best fitting models, right shows the NRMSE of each model compared to the candidates' spectra.
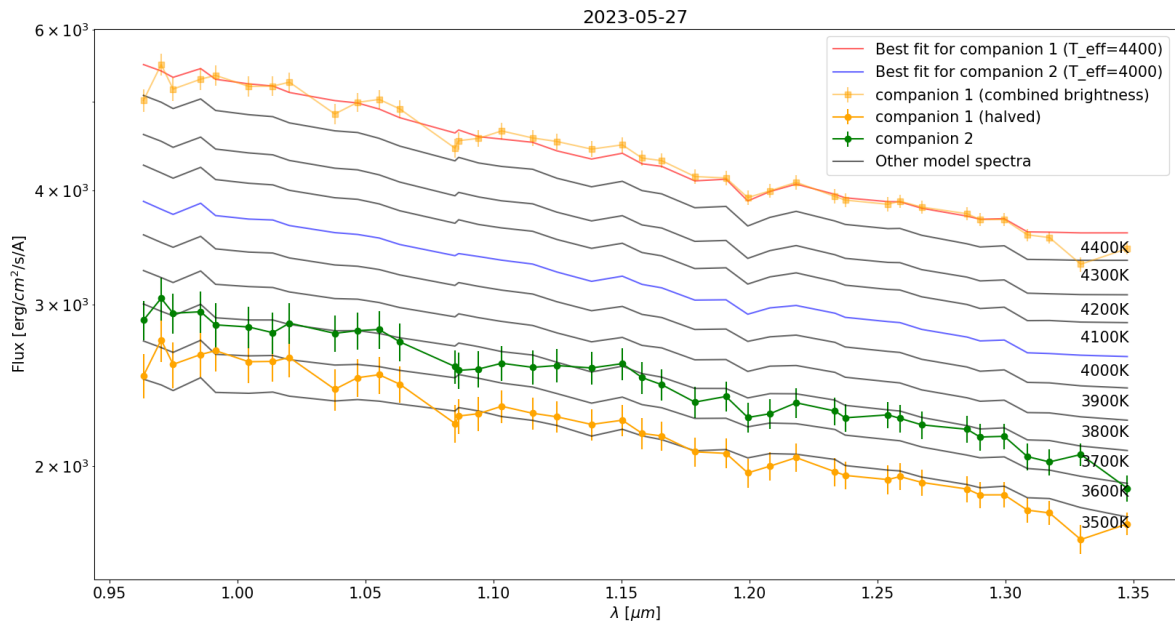
Figure 8.5: Candidate companions to 2MASS J12182762-5943128 (2023-05-27) compared to select spectral models near their best fit temperature. If companion 1 is not an unresolved binary it should be at the same brightness as the 4400K model, and companion 2 should be around the same brightness as the 4000K model, however companion 2 is significantly dimmer. When halved, companion 1 is much closer to companion 2, suggesting it is likely an unresolved binary.
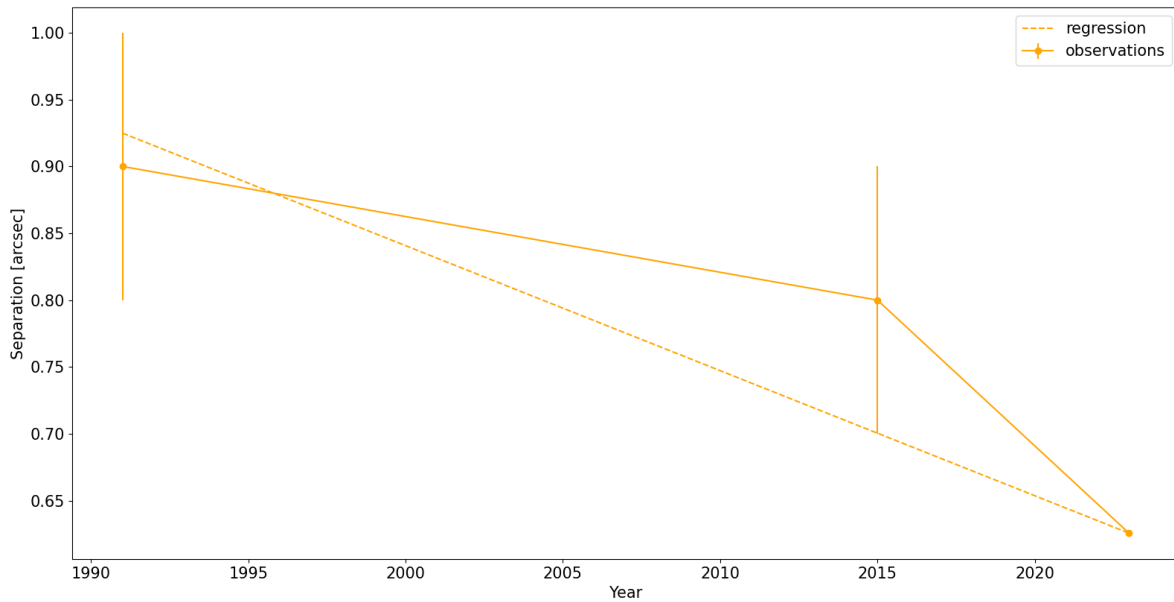
Figure 8.6: Proper motion of candidate companions relative to 2MASS J12182762-5943128 (2023-05-27). The first two observations are from the Washington Double Stars Catalog, and the error is assumed at 0.1".(Mason et al., 2023) The third observation is the one analyzed for this thesis. The regression is just an example showing that it is possible to fit a straight line through these three observations when considering the error.

From this observation alone it is impossible to prove whether the candidates form an equal mass triple system or an unequal mass binary system where candidate 1 is slightly brighter. This uncertainty is compounded by the fact that the AO system was not functioning correctly for the observation of the host star, introducing additional noise which could have affected the atmospheric corrections applied to the candidate spectra. Based on the spectra as analyzed here, the most likely scenario seems to be that they form an equal mass triple system. To conclusively delineate between these hypotheses, it would be necessary to perform follow up observations to look for orbital motion of the objects relative to each other.

The spectra of the companions seem to line up with the models at around 3500K, but the best fit is that the companions are brighter, hotter objects at around 4000–4400K. This suggests that these candidates are likely unrelated background stars, and that is why they appear slightly fainter. Assuming that the candidates are a triple system with temperature of 4200K (the average of the two best fits), that would put them at a distance of around 170pc from Earth. The distance to the host star is only 90pc.(Pecaut and Mamajek, 2016)

This system has two previous observations from the Washington Visual Double Star Catalog.(Mason et al., 2023) These candidates were previously incorrectly assumed to be an equal mass binary companion to the host star. This is due to the fact that the triple system combined appears roughly as bright as the host. The previous observations were not using high contrast imaging and thus could not resolve the candidates into separate sources. The previous observations noted the separation of the host and this triple system, so the proper motion of the candidates relative to the host can be assessed. This is plotted in Figure 8.6.

8.2.2. 2023-05-30-2: 2MASS J12404664-5211046

An image of this observation before and after subtraction is presented in Figure 8.7. There is one faint point source visible in the images at a separation of 0.43" and angle of 295° (measured counterclockwise from north), which is six magnitudes fainter than the host star. The signal to noise of this candidate was measured at each wavelength and is shown in Figure 8.8. This SNR corresponds to an FPF of

3.26e-9, which is below the detection threshold of 3e-7. This means that this point source is a real astrophysical object, however it does not prove that it is gravitationally bound to the host star.
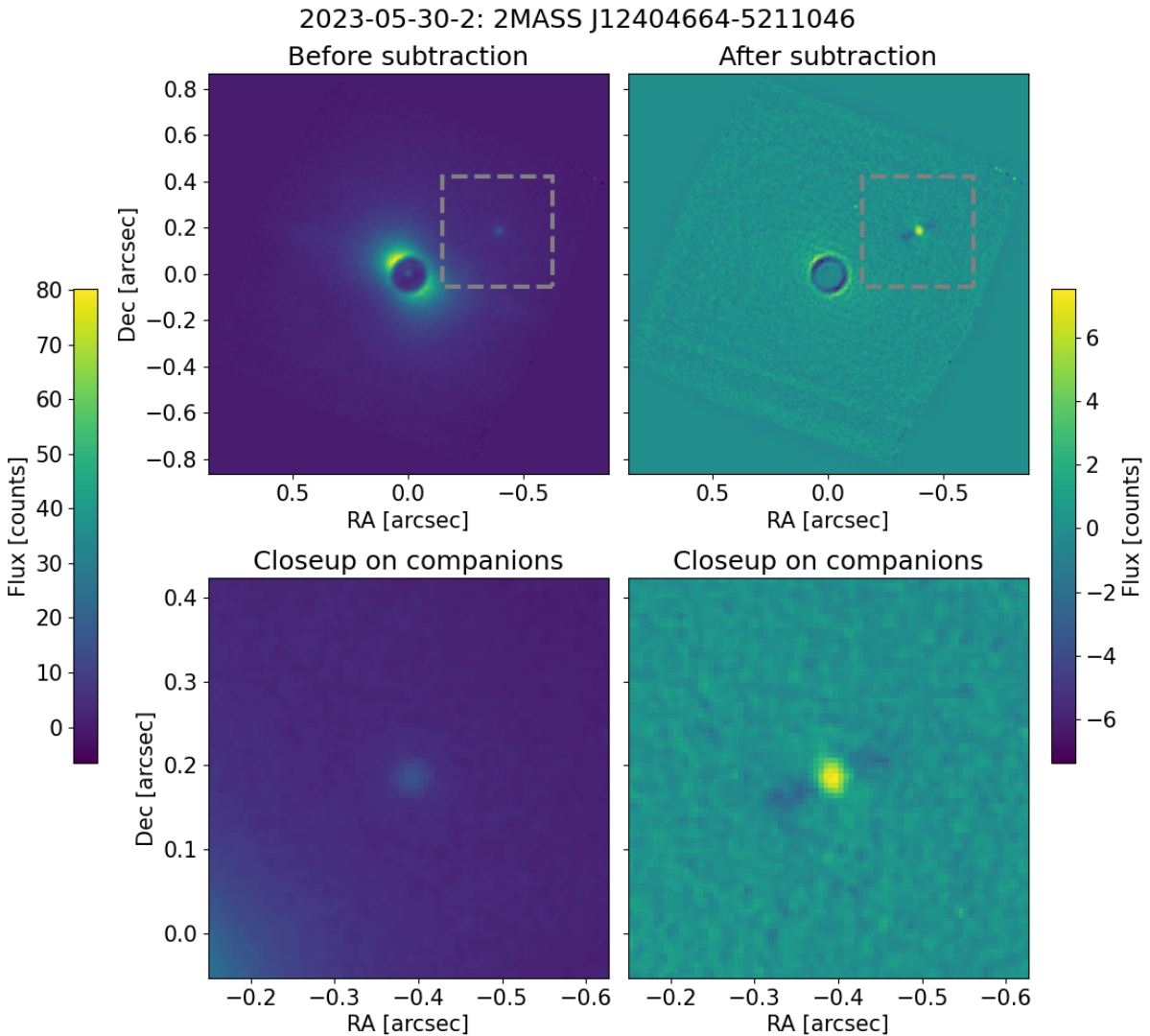
Figure 8.7: Observation of 2MASS J12404664-5211046 (2023-05-30-2) with SPHERE/IFS before (left) and after (right) SDI. There is one point source which is shown in more detail in the second row. The images are rotated such that north is up and east is left. The shape visible in the background after subtraction is the detector with a cut off due to the offset with the IFU.

The next step is to look at the candidate's spectra. This will give an idea of what kind of object it is, and whether it is possible for it to be gravitationally bound to the host star. Figure 8.9 shows the spectra of the companion plotted together with the spectra of the host star and model spectra of several different temperatures. The spectra of both the host star and the companion have been corrected for the Earth atmosphere by matching the host star to the corresponding model spectrum as described in Section 7.3.

The candidate's brightness is consistent with a temperature of 1000K, however the shape of the spectrum is different from the models at this temperature, with an opposite slope that matches better with higher temperature spectra. Checking the NRMSE of the companion spectrum compared to the models gives the best fit as T_{eff}=6000K, as can be seen from Figure 8.10. The models used for fitting only go up to 6000K, so the object may be even hotter. This proves the object is an unrelated background star not gravitationally bound to the host star. For such an object with T_{eff}=6000K to appear this faint, it would need to be located at a distance of 4400pc. The host star is at a distance of 160pc.(Pecaut and Mamajek, 2016)
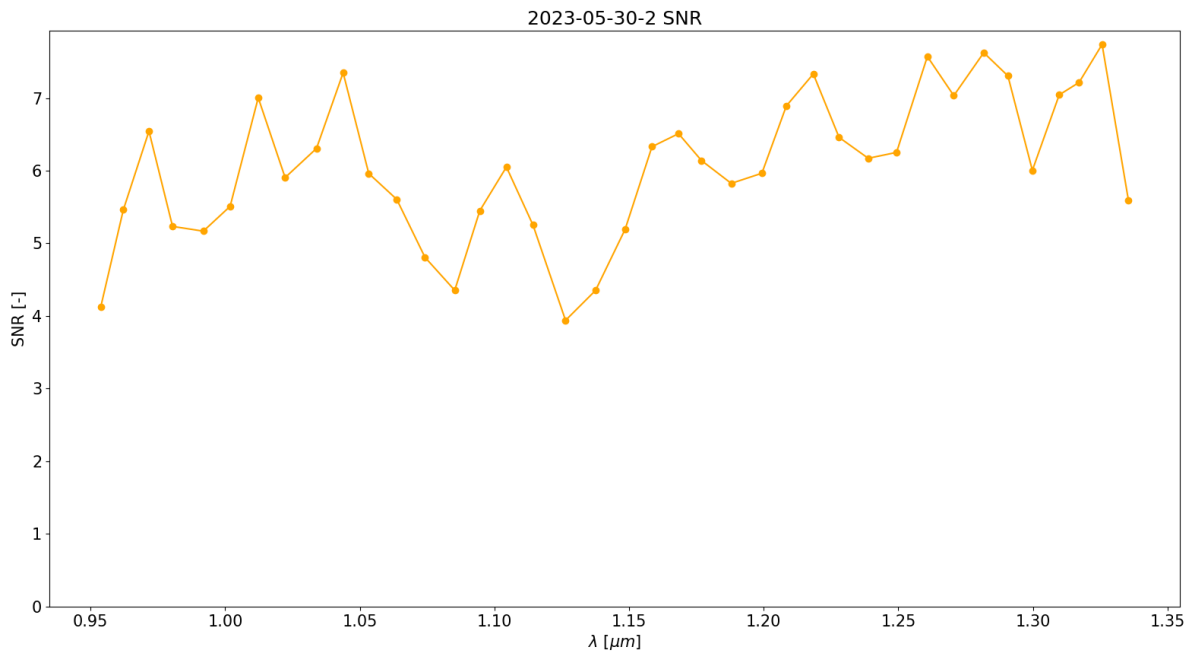
Figure 8.8: SNR of candidate companion to 2MASS J12404664-5211046 (2023-05-30-2) vs λ.
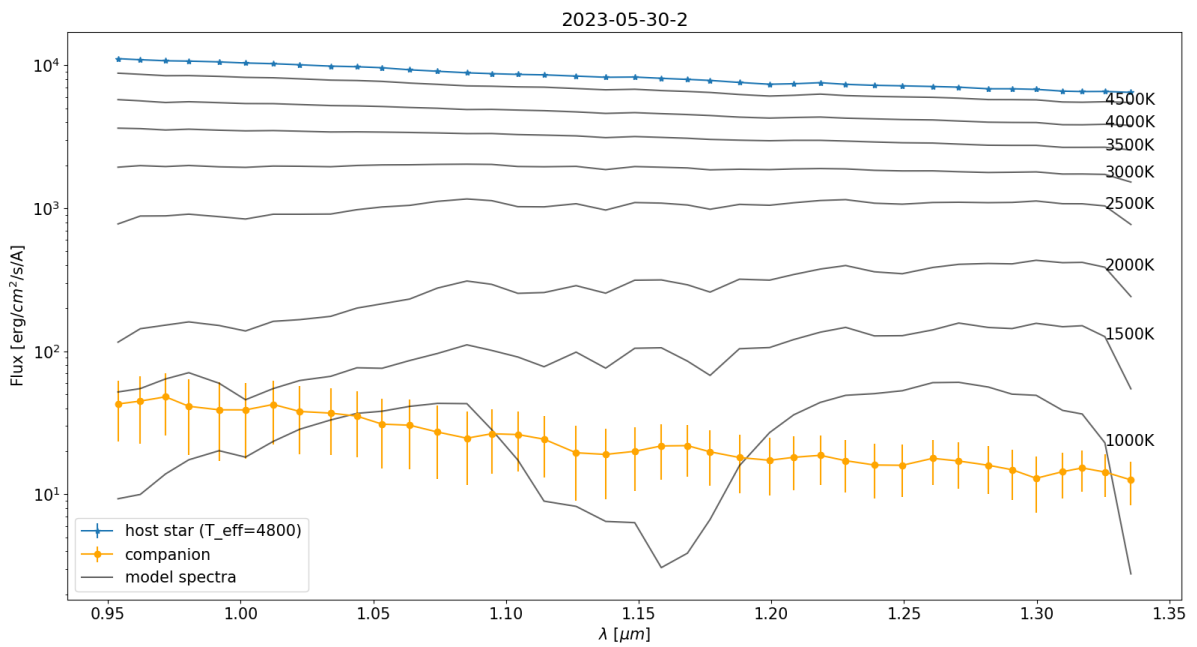
Figure 8.9: Spectra of candidate companion to 2MASS J12404664-5211046 (2023-05-30-2) with model spectra of various temperatures.
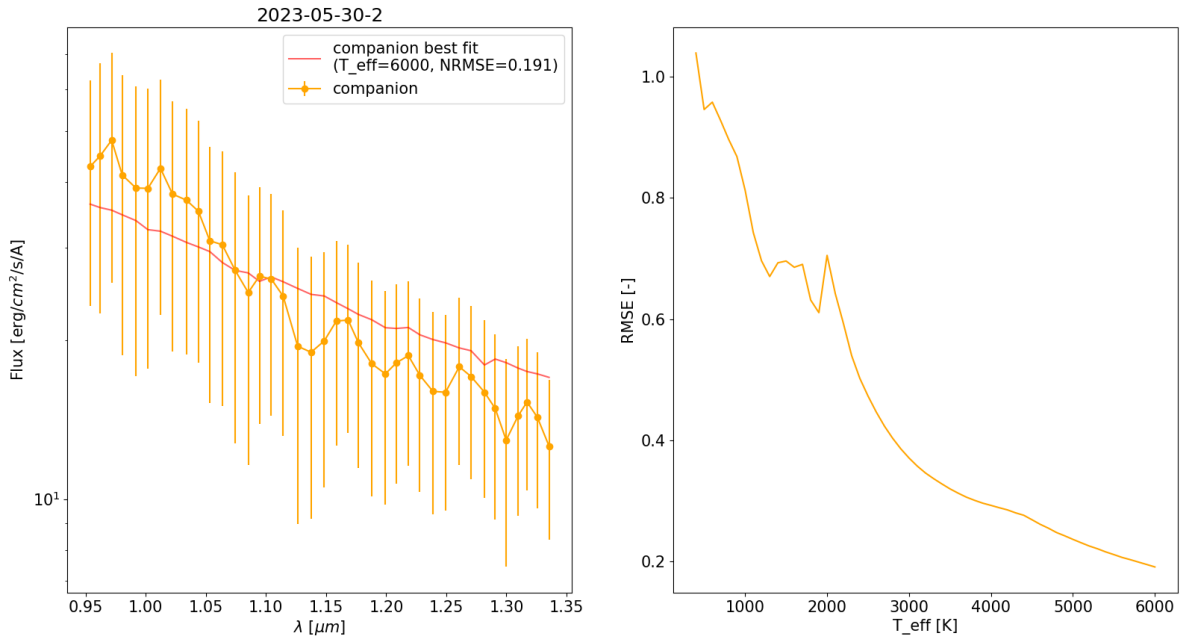
Figure 8.10: Best fit spectra for the candidate companion to 2MASS J12404664-5211046 (2023-05-30-2). Left shows the spectra and the best fitting model, right shows the NRMSE of each model compared to the candidate's spectra.

8.2.3. 2023-06-15-1: 2MASS J12560830-6926539

The coadded observation is shown in Figure 8.11, with one candidate that has been circled. This candidate has an extended shape compared to the other candidate companions, which means it is very likely a binary object, with two different sources orbiting each other. Due to this extended shape, a larger aperture of 0.5" was used to measure its brightness, vs. the 0.35" aperture used for the other candidate companions. The center of the pair is at a separation of around 0.19" and an angle of $39°$ (measured counterclockwise from north), and their combined brightness is around one magnitude fainter than the host star. The SNR is plotted in Figure 8.12, and gives an FPF of 4.67e-9, which is well below the threshold for detection, proving this signal is from a real object and not just noise.

To investigate the relative masses of the two halves of the binary, the average frame of the cube was subtracted from each wavelength slice. If one of the objects had a different spectral slope than the other then one half of the object would be brighter at some wavelengths and the other half would be brighter at others. However, both halves of the object showed roughly equal brightness at all wavelengths. This means that both halves of the binary have the same spectral slope, and thus are equal in size. This is the most commonly seen type of binary.(Duchêne and Kraus, 2013)

The spectra of the object is plotted in Figure 8.13 with models of various temperatures. The candidate's spectrum has been divided by two to scale it for the fact that it is a binary. Its brightness compared to the host puts it near 2500K, however the slope does not match up with these models. The best fit temperature is a hotter 3400K, as can be seen from Figure 8.14. This suggests the binary is in the background of the image and not a bound companion to the host star. An equal mass binary of 3400K and this apparent brightness would need to be located at around 170pc away. The host star is at a distance of 100pc.(Pecaut and Mamajek, 2016)
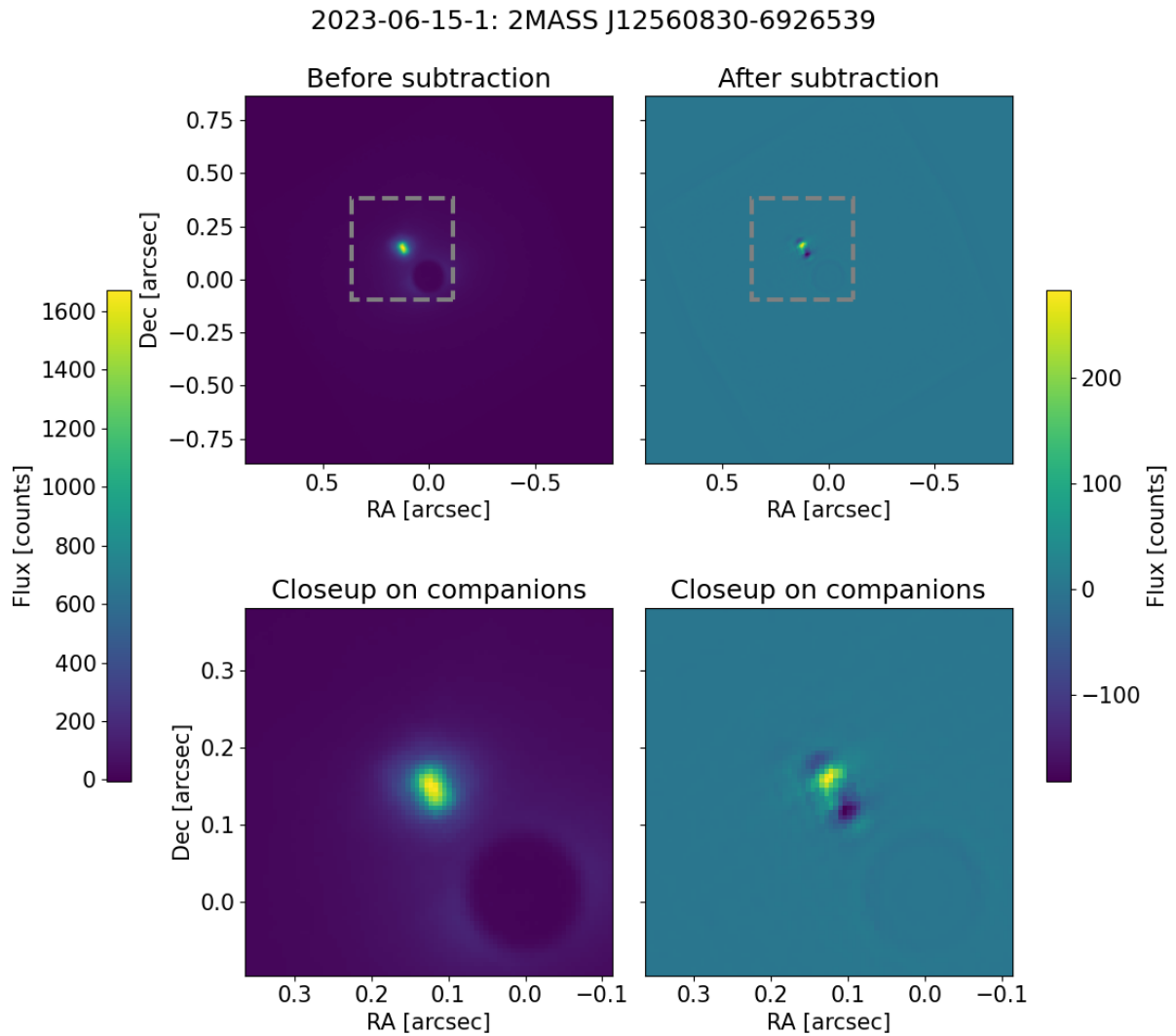
Figure 8.11: Observation of 2MASS J13130714-4537438 (2023-06-15-1) with SPHERE/IFS before (left) and after (right) SDI. There is one (slightly extended) source in the images, which is shown in more detail in the second row. The images are rotated such that north is up and east is left.
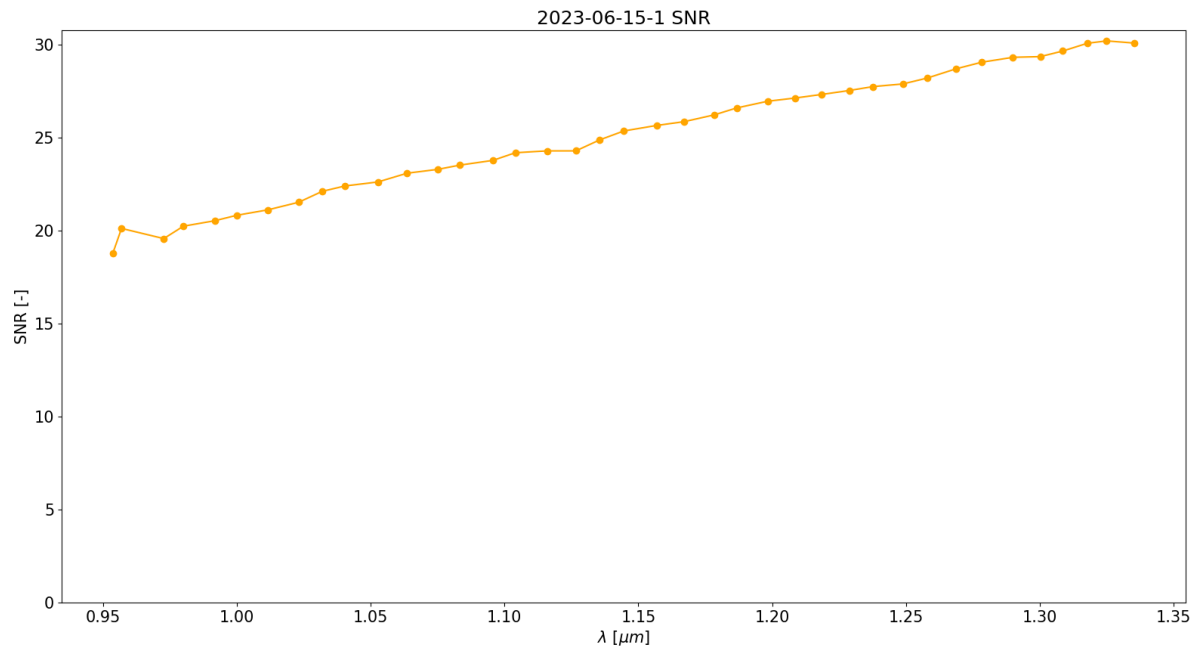
Figure 8.12: SNR of candidate companion to 2MASS J12560830-6926539 (2023-06-15-1) vs λ.
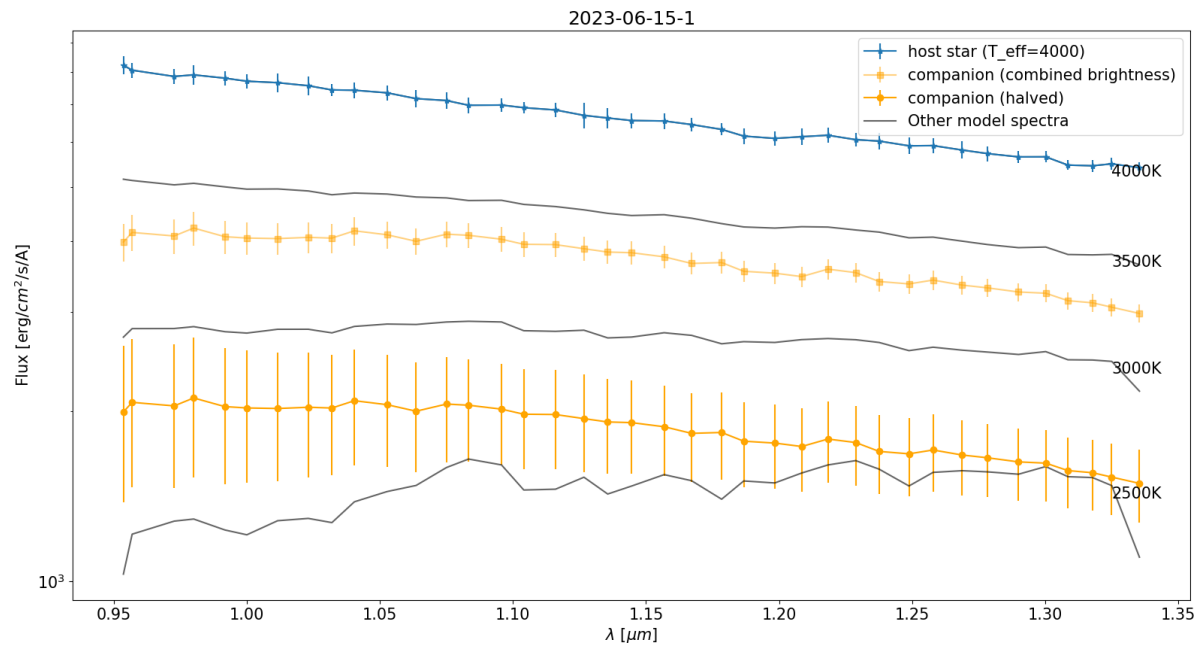
Figure 8.13: Spectra of candidate companion to 2MASS J12560830-6926539 (2023-06-15-1) with model spectra of various temperatures.
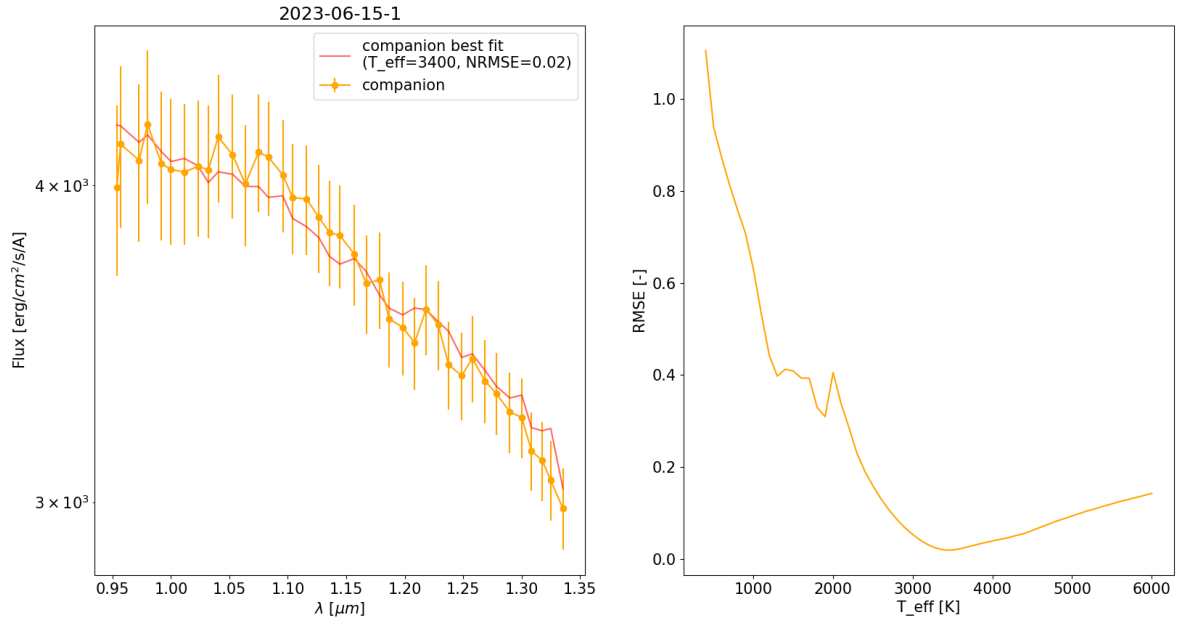
Figure 8.14: Best fit spectra for the candidate companion to 2MASS J13130714-4537438 (2023-06-15-1). Left shows the spectra and the best fitting model, right shows the NRMSE of each model compared to the candidate's spectra.

8.2.4. 2023-07-26-1: 2MASS J13130714-4537438

The observation of 2023-07-26-1 has one very bright point source, visible in Figure 8.15. It is almost exactly the same apparent magnitude as its host star, and is located at a separation of 0.56" and angle of 158°. It has an extremely high SNR (as can be seen in Figure 8.16), with corresponding FPF of 4.73e-37. This leaves no doubt that this is a real astrophysical object.

Figure 8.17 shows the spectrum of the candidate companion plotted alongside the host star and models of various temperatures. At these wavelengths, the candidate is actually slightly brighter than the host star, once the sky background is subtracted from the host star spectrum. There was an issue with the AO system of the telescope when making the observation of the host star, so this observation is extremely noisy and bad quality. This could have a big effect on the host star spectrum, and thus the atmospheric correction applied to the candidate. Assuming that these spectra are correct, there are a couple possibilities for why the candidate may be brighter than the host star. The telescope operator may have accidentally centered the observation on the wrong star, which is definitely possible given that they are both quite bright and both very close together. Alternatively, the candidate may be dimmer in visible light (which is used to point the telescope), but brighter at these NIR wavelengths. This could be the case if the companion is a background star with dust in front of it, as the dust would cause more extinction at shorter wavelengths.

Comparing the spectra of the companion with the models of equal brightness show that the slope of the candidate is slightly steeper, which suggests it may be a hotter background object. Checking the fit of all the models with the NRMSE shows that the best fit temperature for the candidate is 5600K (see Figure 8.18). This puts the candidate behind the host star at a distance of 260pc from Earth, whereas the target star is at around 140pc according to Pecaut and Mamajek (2016).
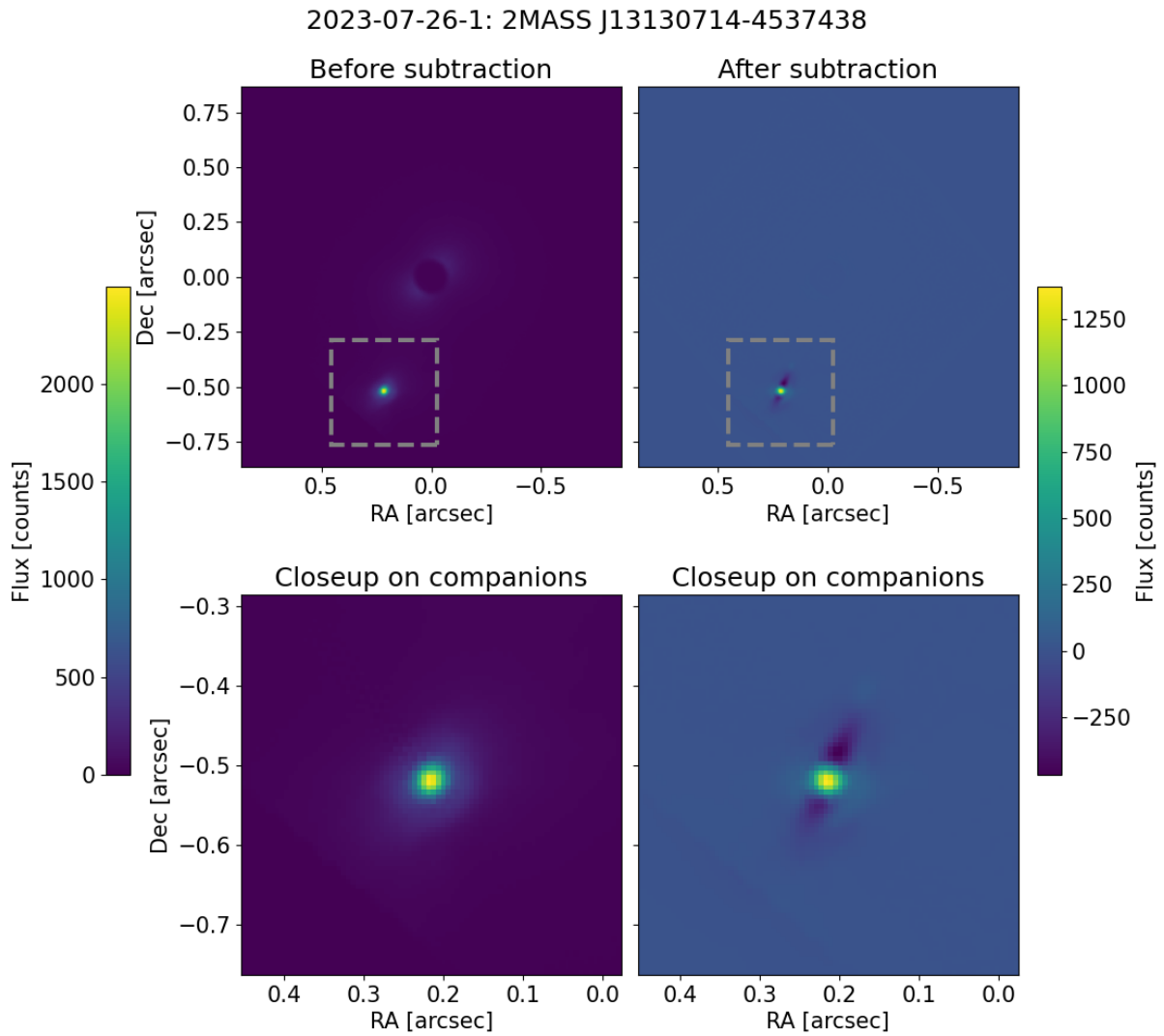
Figure 8.15: Observation of 2MASS J13130714-4537438 (2023-07-26-1) with SPHERE/IFS before (left) and after (right) SDI. There is one point source in the images, which is shown in more detail in the second row. The images are rotated such that north is up and east is left.
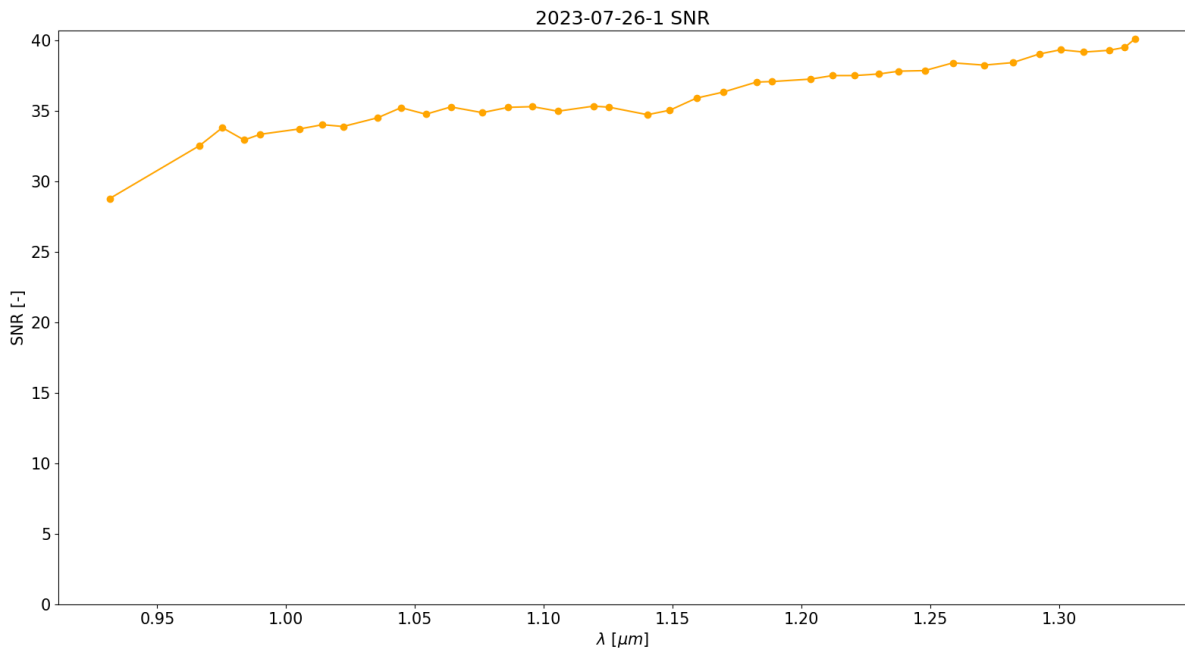
Figure 8.16: SNR of candidate companion to 2MASS J13130714-4537438 (2023-07-26-1) vs λ.
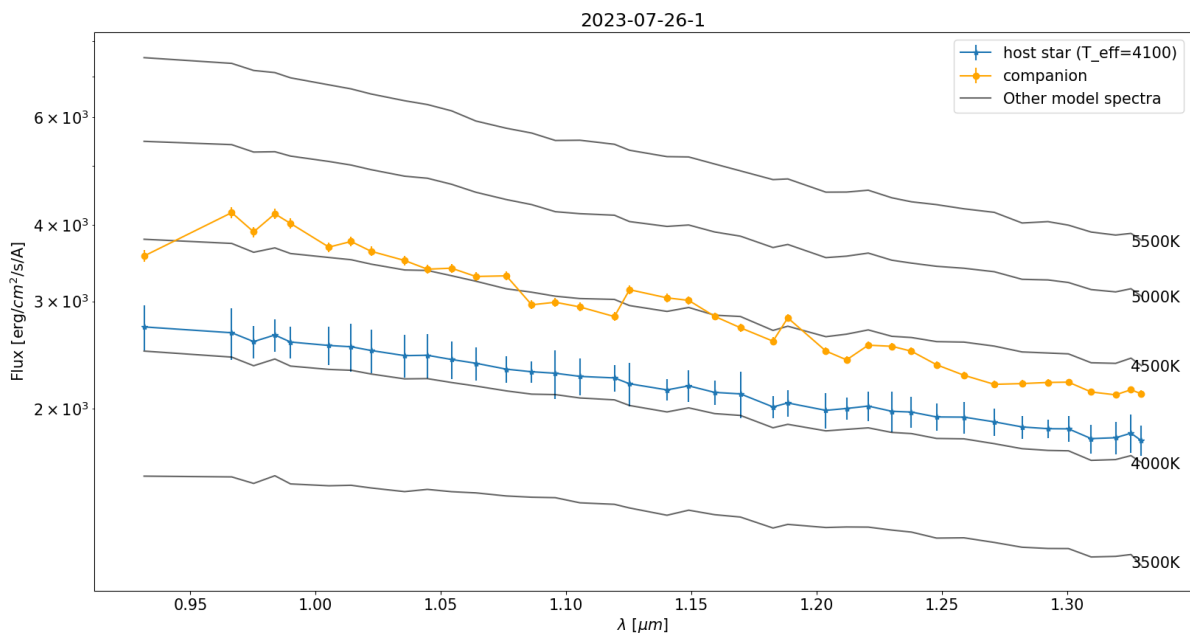
Figure 8.17: Spectra of candidate companion to 2MASS J13130714-4537438 (2023-07-26-1) with model spectra of various temperatures.
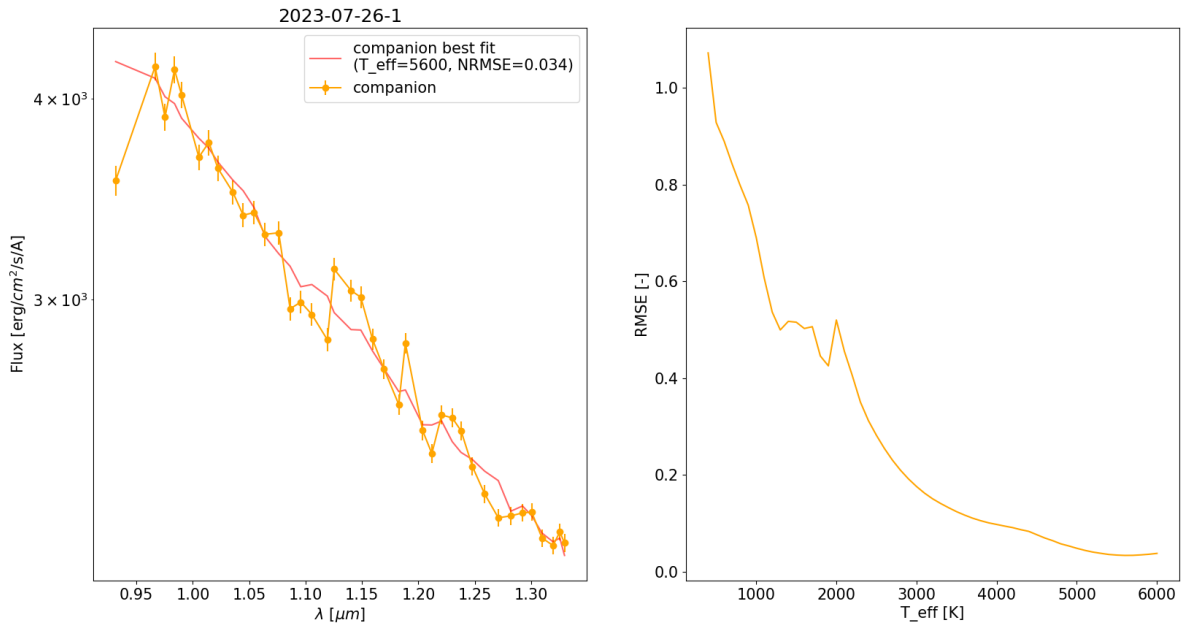
Figure 8.18: Best fit spectra for the candidate companion to 2MASS J13130714-4537438 (2023-07-26-1). Left shows the spectra and the best fitting model, right shows the NRMSE of each model compared to the candidate's spectra.

8.2.5. 2023-08-07-2: 2MASS J13015435-4249422

An image of the observation of this system is shown in Figure 8.19. There are two point sources here. The SNR for both is plotted in Figure 8.20. The closer candidate (hereby referred to as candidate or companion "1") is located at a separation of 0.52" and angle of 231°, and is 2.5 magnitudes fainter than the host star, with an FPF of 1.48e-39. The further candidate is at a separation of 0.59" and angle of 233°, and is slightly fainter, being three magnitudes below the host star, and with an FPF of 1.37e-37.

Looking at the spectra for both candidates (which is shown in Figure 8.21), the two appear to be background stars as the shape of their spectra do not match the models of equivalent brightness. Also, both seem to have very similar shapes for the spectra, and candidate 1 is a little less than two times as bright as candidate 2. (1.6 times as bright to be precise.) This suggests that candidate 1 may actually be an unresolved binary which is together in a triple system with candidate 2. The fact that the two candidates appear so close together in the images lends support to this idea. That the brightness of 1 is slightly less than double 2 could be explained by one of the stars partially eclipsing the other. The NRMSE of both candidates compared to each other is 0.01, which shows the two spectra are nearly identical. Looking at the best fitting model spectra for each candidate in Figure 8.22 provides further evidence: both candidates have almost exactly the same best fit temperature, despite the difference in brightness. This can only be explained if candidate 1 is an unresolved binary, or if candidate 2 is further away and thus appears dimmer. Given the very high occurrence rates of multiple star systems (see Duchêne and Kraus, 2013), it seems more likely that this represents a triple star system, compared to the alternative that candidate 2 is an unrelated star even further away which happens to be the same type as candidate 1. To prove this definitively, additional observations should be made to look for orbital motion of the candidates relative to each other.

Given that this is a triple system with all three stars at T_{eff} around 3400K, that puts the candidates at a distance of around 360pc. The host star is at a distance of 130pc.(Pecaut and Mamajek, 2016)
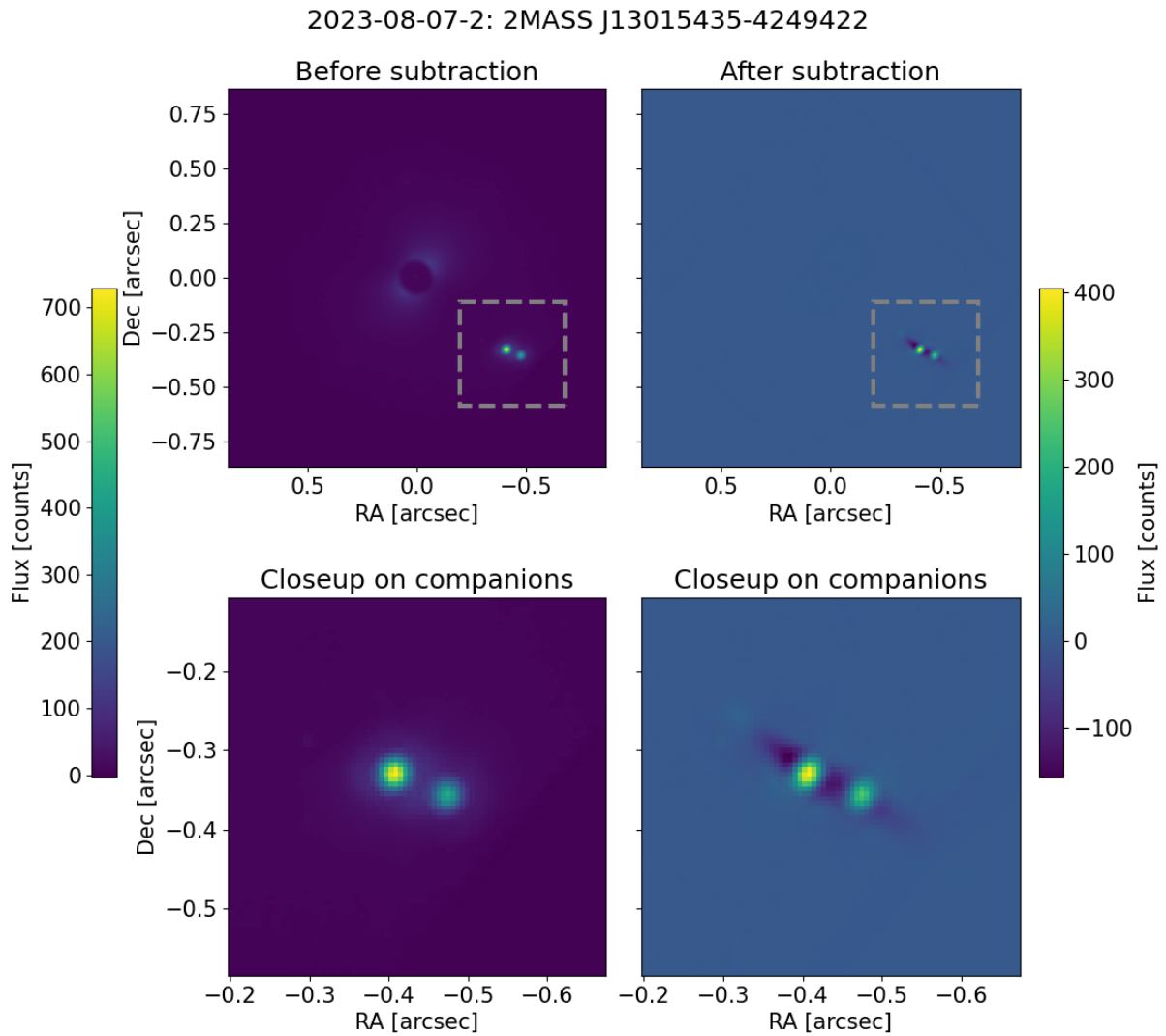
Figure 8.19: Observation of 2MASS J13015435-4249422 (2023-08-07-2) with SPHERE/IFS before (left) and after (right) SDI. There are two point sources in the images, which are shown in more detail in the second row. The images are rotated such that north is up and east is left.
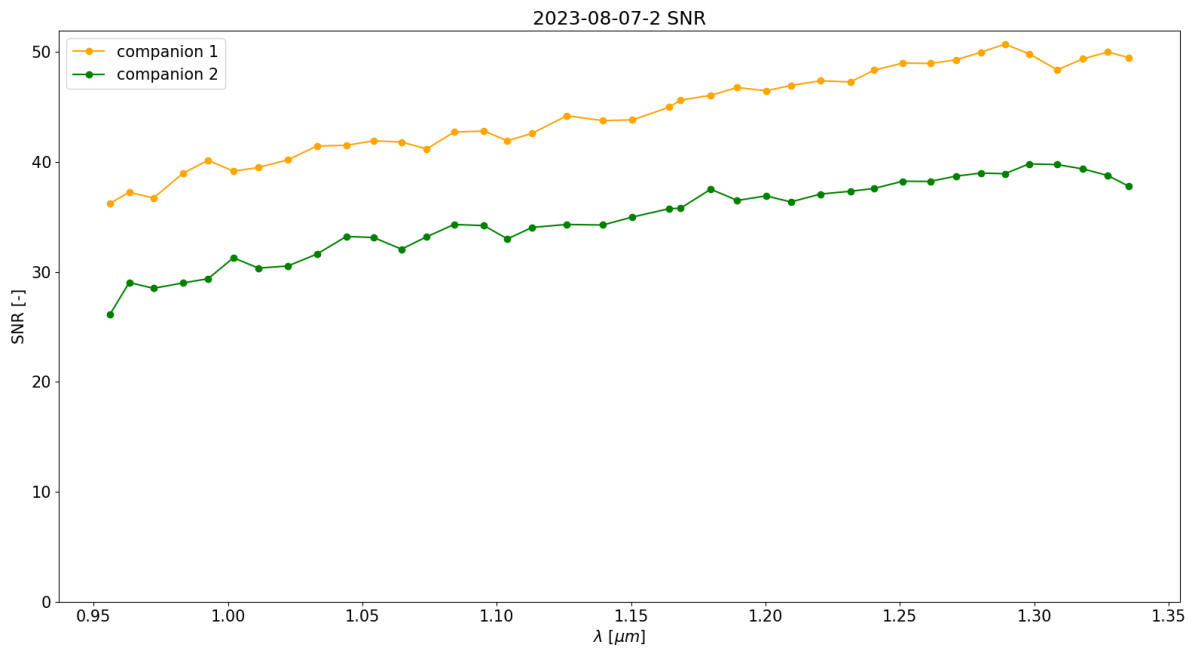
Figure 8.20: SNR of candidate companions to 2MASS J13015435-4249422 (2023-08-07-2) vs λ.
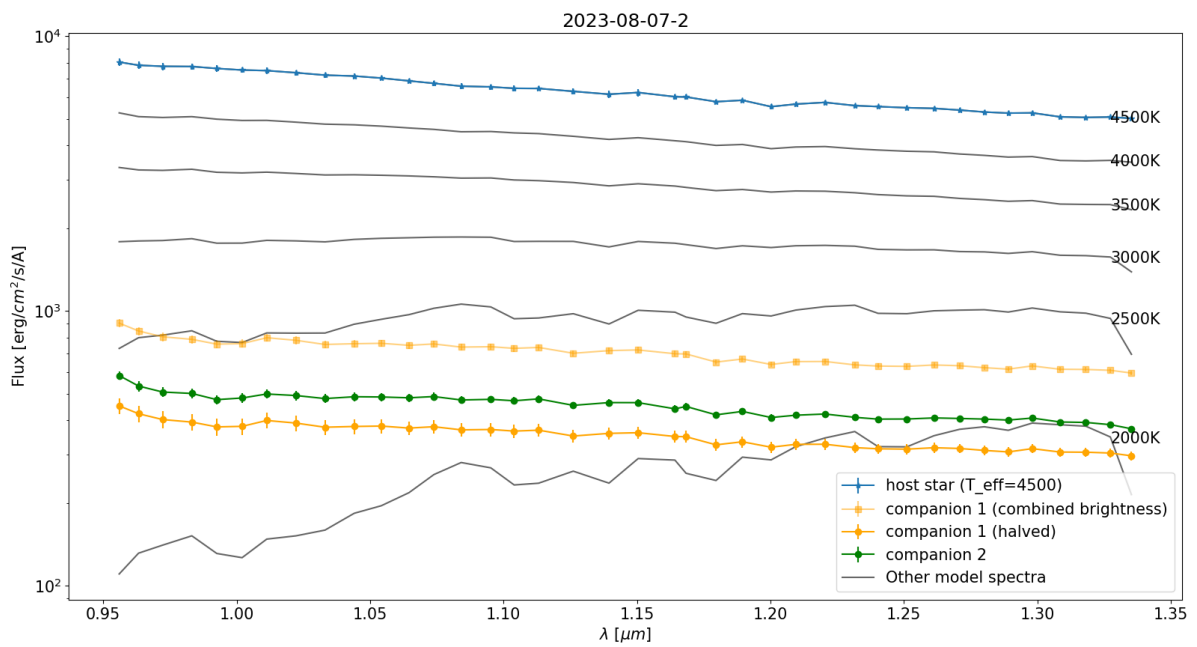
Figure 8.21: Spectra of candidate companions to 2MASS J13015435-4249422 (2023-08-07-2) with model spectra of various temperatures.
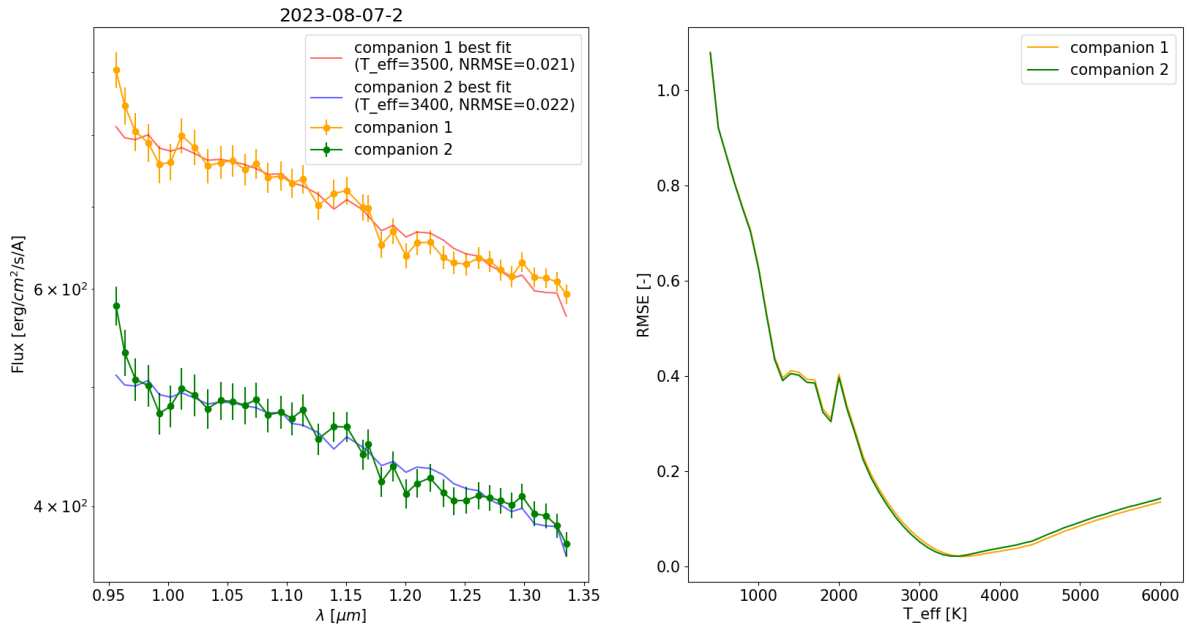
Figure 8.22: Best fit spectra for the candidate companions to 2MASS J13015435-4249422 (2023-08-07-2). Left shows the spectra and the best fitting model, right shows the NRMSE of each model compared to the candidate's spectra.

8.2.6. Final Companion Determination

For all the systems with candidates, these were determined to be unrelated background objects. Table 8.2 summarizes some of the key properties of the target systems and the candidate companions.

8.3. Detection Limits

Detection limits for each system were also computed. These give a rough idea of what planets may still exist in these systems that could not be detected. Curves for all the observations together are plotted in Figure 8.23. Individual curves for every system can be seen in Appendix B, with curves for both before and after SDI.

Anything above the curve is bright enough that it would have been detectable in these observations, and below the line would be too faint to be confidently detectable in these observations. Thus there is still the possibility that fainter objects may be detected when looking with other instruments in the future.

It can be seen that in almost all the contrast curves, after around 0.5", the post SDI contrast becomes much worse. This is because 1" (thus 0.5" separation in any direction) is the effective FOV for the IFS after SDI, as this is the portion of the PSF that is visible at all wavelengths. See Section 6.1 for more detail.

The contrast limits have not been computed for those systems with candidate companions, as the candidates interfere with the computation of these curves. Figure 8.24 shows an example of a contrast curve which has been (incorrectly) computed for a system with candidates. The true contrast limits for these systems can be assumed to be similar to the systems without candidates.

Figure 8.25 puts these detection limits in context by overplotting them on a graph of all exoplanets that have thus far been detected. The search space that this work is sensitive to is only massive, wide orbit planets, however this is a region that is still very under-represented compared to the multitude of detections of close in planets by other methods. The same figure is shown zoomed in on the region of interest in Figure 8.26

Table 8.2: Key properties of systems with candidate companions.

(a) Systems with one candidate.

Observation		2023-05-30-2	2023-06-15-1	2023-07-26-1
Host star name	2MASS J	12404664-5211046	12560830-6926539	13130714-4537438
Separation	[arcsec]	0.43	0.19	0.56
Angle	[deg]	295	39	158
FPF	-	3.3e-9	4.7e-9	4.7e-37
Best fit temp.	[K]	6000+	3500	5600
Host star distance	[pc]	160	100	140
Candidate distance	[pc]	4400+	170	260
Candidate determination	-	Background star	Background binary system	Background star

(b) Systems with multiple candidates.

Observation		2023-05-27		2023-08-07-2	
Host star name	2MASS J	12182762-5943128		13015435-4249422	
Candidate	-	1	2	1	2
Separation	[arcsec]	0.61	0.64	0.52	0.59
Angle	[deg]	271	278	231	233
FPF	-	1.7e-24	2.6e-10	1.48e-39	1.37e-37
Best fit temp.	[K]	4400	4000	3500	3400
Host star distance	[pc]	90	90	130	130
Candidate distance	[pc]	170	170	360	360
Candidate determination	-	Background triple system		Background triple system	
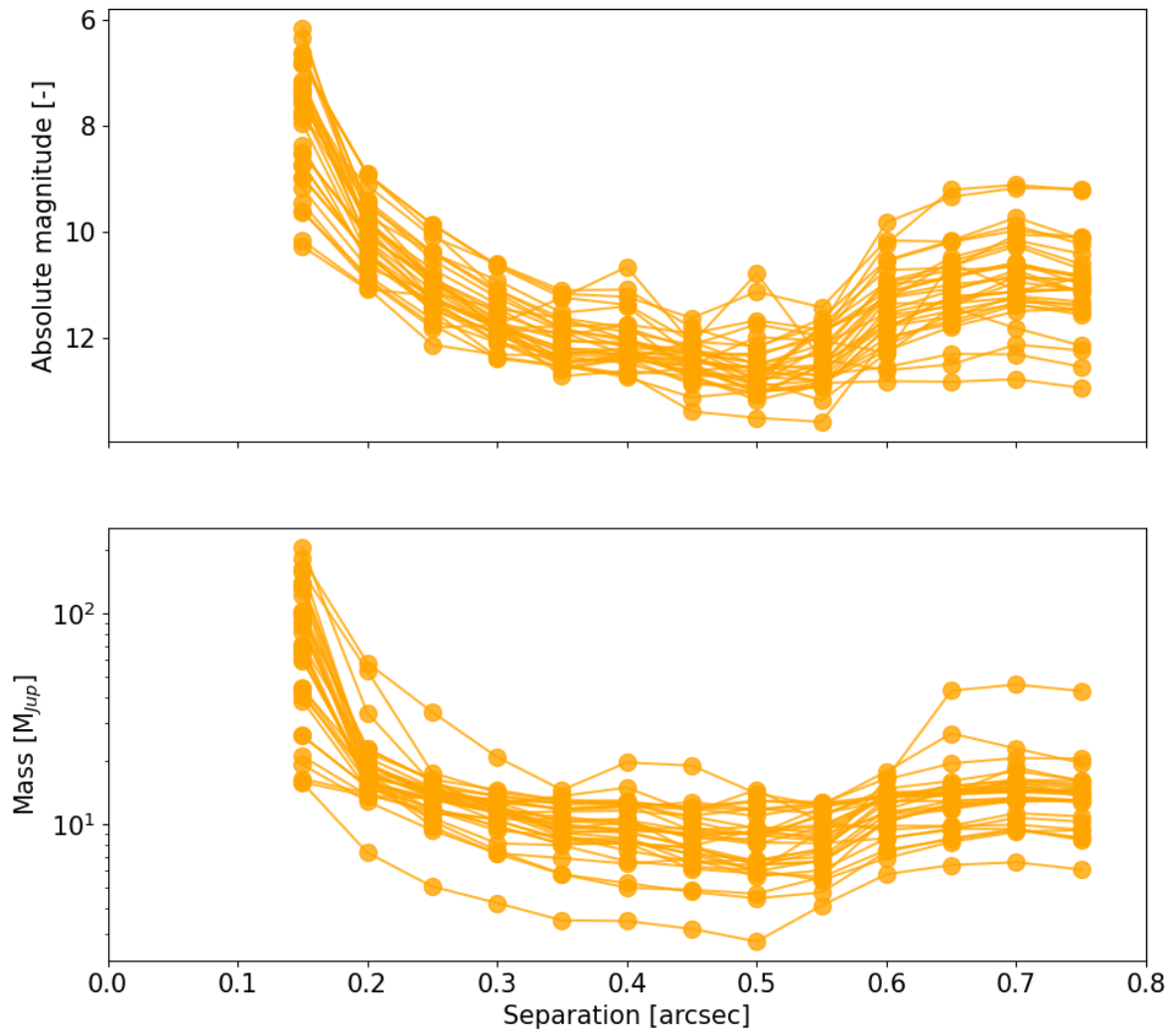
Figure 8.23: Contrast curves for all observations after SDI has been applied. Systems with candidate companions have been excluded.
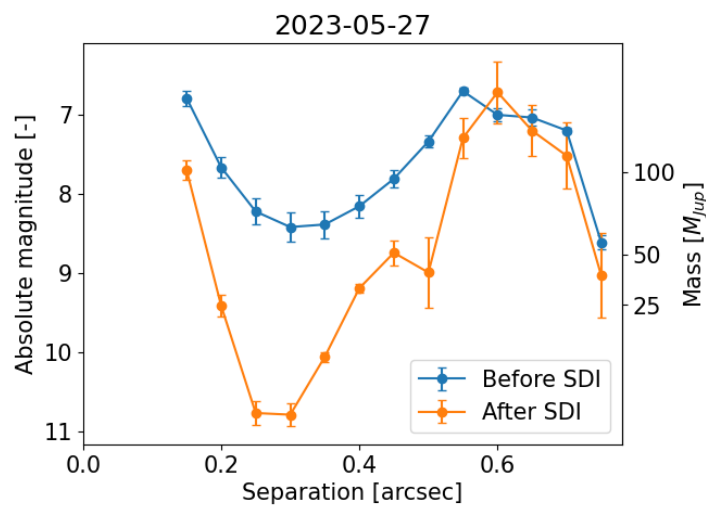
Figure 8.24: Contrast curve for 2MASS J12182762-5943128 (2023-05-27). This system has two bright candidate companions at around 0.61" and 0.64", which interfere with the estimation of the contrast limits. This prevents the limits from being accurately determined for this system and others with candidate companions.
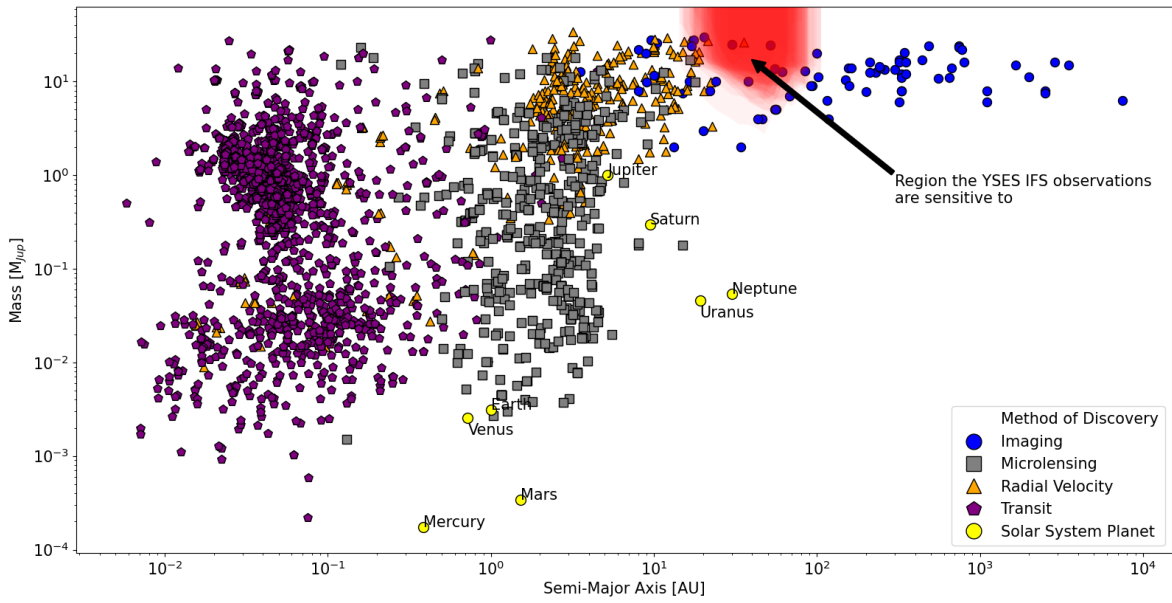
Figure 8.25: Detection limits for these observations plotted on top of a graph of most exoplanets that have been discovered thus far. The red region shows the region these observations would be sensitive to after SDI has been applied. The darkness of the region corresponds to what percentage of the observations shown here are sensitive to that part of the search space.
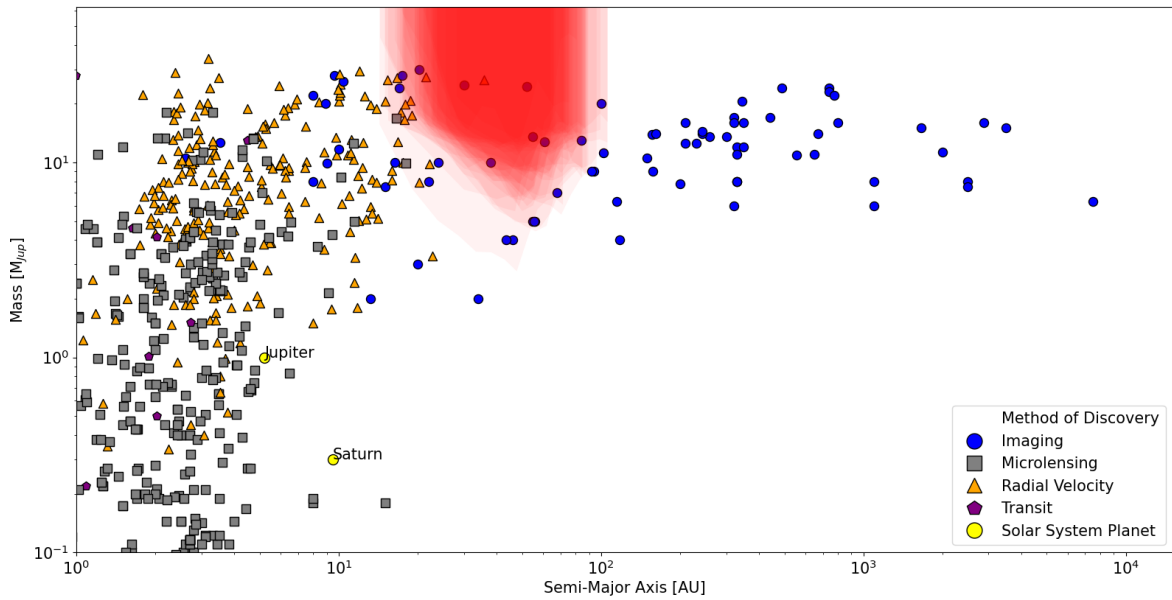
Figure 8.26: Detection limits for these observations plotted on top of a graph of most exoplanets that have been discovered thus far, zoomed in on the region of interest. Again, the red region shows the region these observations are sensitive to after SDI. In this figure it can be seen that this region represents a good portion of the full direct imaging search space, but is shifted closer in than most direct imaging detections because of the small FOV of the IFS instrument.

9

Conclusion

This thesis followed the process of analyzing 41 observations from YSES taken with SPHERE/IFS. The ultimate goal was to aid this survey and the broader scientific community by detecting new wide orbit giant planets which would help the understanding of how these objects form. The main research question for this thesis was as follows:

What companions can be identified in the IFS data from YSES, and what are the characteristics of these companions?

During this thesis, the 41 YSES observations were reduced, post processed by applying SDI, and carefully examined. On this specific dataset the SDI unfortunately did not reveal any fainter objects for study. However, it still pushes the contrast limit deeper and shows that if any wide orbit giant planets were in the images, they likely would have been seen. Detection limits were computed for all the observed systems, and for most systems the result is that planets down to around $5–10M_J$ at a separation of 0.3"–0.5".

The reduced cubes revealed eight candidate companions in five systems. These candidates were then characterized by measuring their SNR and spectra. All eight candidates were well above the detection threshold, and are real astrophysical objects. All the candidates were determined to be unrelated background stars which are not gravitationally bound to the host star. These candidates range in effective temperature from around 3500K up to 6000K, with the majority of candidates being M or K type stars. In two separate systems with two candidates each (the observations of 2023-05-27 and 2023-08-07-2), these candidates proved to be a triple system, with one of the point sources being an unresolved binary. One of these triple systems was previously identified as an equal mass binary object to the host star, however this thesis has proved that this is not the case. In addition one other binary system was discovered (in 2023-06-15-1), and two other bright background stars were found.

The IFS was particularly useful for this work, as having low resolution spectra of the objects made it possible to estimate whether the object is a background star or a companion without needing to perform follow-up observations.

Although no planetary mass objects were detected, and indeed no gravitationally bound companions were detected, these results are still beneficial to the scientific community. Non-detections can help refine occurrence estimates for planets around these types of stars, which is one of the goals of YSES. Additionally, one of the systems that was once thought to be a binary system was proved to be a single star. This system may have been understudied because binary systems are usually ignored when hunting for planets. This work shows that it is still useful to do follow up observations on such systems to be sure. This work has also shown what kind of objects may still exist in these systems, and that they are worth performing follow-up observations on to look for fainter planetary mass companions. The two background triple systems warrant further study to verify these observations as these are somewhat unusual objects. Additional observations will be able to confirm if these are indeed triple systems by

looking for orbital motion of the objects relative to each other.

That no new planets were detected is not unusual. Meta-analysis of other surveys puts the occurrence rate of wide orbit giant planets and brown dwarfs around sun-like stars at around 1%.(Bowler and Nielsen, 2018) This work only had a sample of 37 stars; not finding any planetary mass companions in that sample is consistent with this occurrence rate.

Bibliography

F. Allard, D. Homeier, B. Freytag, W. Schaffenberger, and A. S. Rajpurohit. Progress in modeling very low mass stars, brown dwarfs, and planetary mass objects. *MSAIS*, 24:128, January 2013. doi: 10.48550/arXiv.1302.6559.

Adam Amara and Sascha P. Quanz. PYNPOINT: an image processing package for finding exoplanets. *MNRAS*, 427(2):948–955, December 2012. doi: 10.1111/j.1365-2966.2012.21918.x.

Jacopo Antichi, Kjetil Dohlen, Raffaele G. Gratton, Dino Mesa, Riccardo U. Claudi, Enrico Giro, Anthony Boccaletti, David Mouillet, Pascal Puget, and Jean-Luc Beuzit. BIGRE: A Low Cross-Talk Integral Field Unit Tailored for Extrasolar Planets Imaging Spectroscopy. *ApJ*, 695(2):1042–1057, April 2009. doi: 10.1088/0004-637X/695/2/1042.

Etienne Artigau, Rebecca A. Bernstein, Timothy Brandt, Jeffrey Chilcote, Laird Close, Ian Crossfield, Jacques-Robert Delorme, Courtney Dressing, Michael P. Fitzgerald, Jonathan Fortney, Andrew Howard, Richard Frazin, Nemanja Jovanovic, Quinn Konopacky, Julien Lozi, Jared R. Males, Christian Marois, Benjamin A. Mazin, Max A. Millar-Blanchaer, Katie M. Morzinski, Lewis Roberts, Eugene Serabyn, Gautam Vasisht, J. Kent Wallace, and Ji Wang. Direct Imaging in Reflected Light: Characterization of Older, Temperate Exoplanets With 30-m Telescopes. *arXiv*, art. arXiv:1808.09632, August 2018. doi: 10.48550/arXiv.1808.09632.

R. Asensio-Torres, M. Janson, M. Bonavita, S. Desidera, C. Thalmann, M. Kuzuhara, Th. Henning, F. Marzari, M. R. Meyer, P. Calissendorff, and T. Uyama. SPOTS: The Search for Planets Orbiting Two Stars. III. Complete sample and statistical analysis. *A&A*, 619:A43, October 2018. doi: 10.1051/0004-6361/201833349.

D. Barbato, A. Sozzetti, S. Desidera, M. Damasso, A. S. Bonomo, P. Giacobbe, L. S. Colombo, C. Lazzoni, R. Claudi, R. Gratton, G. LoCurto, F. Marzari, and C. Mordasini. Exploring the realm of scaled solar system analogues with HARPS. *A&A*, 615:A175, August 2018. doi: 10.1051/0004-6361/201832791.

J. L. Beuzit, A. Vigan, D. Mouillet, K. Dohlen, R. Gratton, A. Boccaletti, J. F. Sauvage, H. M. Schmid, M. Langlois, C. Petit, A. Baruffolo, M. Feldt, J. Milli, Z. Wahhaj, L. Abe, U. Anselmi, J. Antichi, R. Barette, J. Baudrand, P. Baudoz, A. Bazzon, P. Bernardi, P. Blanchard, R. Brast, P. Bruno, T. Buey, M. Carbillet, M. Carle, E. Cascone, F. Chapron, J. Charton, G. Chauvin, R. Claudi, A. Costille, V. De Caprio, J. de Boer, A. Delboulbé, S. Desidera, C. Dominik, M. Downing, O. Dupuis, C. Fabron, D. Fantinel, G. Farisato, P. Feautrier, E. Fedrigo, T. Fusco, P. Gigan, C. Ginski, J. Girard, E. Giro, D. Gisler, L. Gluck, C. Gry, T. Henning, N. Hubin, E. Hugot, S. Incorvaia, M. Jaquet, M. Kasper, E. Lagadec, A. M. Lagrange, H. Le Coroller, D. Le Mignant, B. Le Ruyet, G. Lessio, J. L. Lizon, M. Llored, L. Lundin, F. Madec, Y. Magnard, M. Marteaud, P. Martinez, D. Maurel, F. Ménard, D. Mesa, O. Möller-Nilsson, T. Moulin, C. Moutou, A. Origné, J. Parisot, A. Pavlov, D. Perret, J. Pragt, P. Puget, P. Rabou, J. Ramos, J. M. Reess, F. Rigal, S. Rochat, R. Roelfsema, G. Rousset, A. Roux, M. Saisse, B. Salasnich, E. Santambrogio, S. Scuderi, D. Segransan, A. Sevin, R. Siebenmorgen, C. Soenke, E. Stadler, M. Suarez, D. Tiphène, M. Turatto, S. Udry, F. Vakili, L. B. F. M. Waters, L. Weber, F. Wildi, G. Zins, and A. Zurlo. SPHERE: the exoplanet imager for the Very Large Telescope. *A&A*, 631:A155, November 2019. doi: 10.1051/0004-6361/201935251.

A. J. Bohn, M. A. Kenworthy, C. Ginski, M. Benisty, J. de Boer, C. U. Keller, E. E. Mamajek, T. Meshkat, G. A. Muro-Arena, M. J. Pecaut, F. Snik, S. G. Wolff, and M. Reggiani. Discovery of a directly imaged disk in scattered light around the Sco-Cen member Wray 15-788. *A&A*, 624:A87, April 2019. doi: 10.1051/0004-6361/201834523.

A. J. Bohn, M. A. Kenworthy, C. Ginski, C. F. Manara, M. J. Pecaut, J. de Boer, C. U. Keller, E. E. Mamajek, T. Meshkat, M. Reggiani, K. O. Todorov, and F. Snik. The Young Suns Exoplanet Survey: Detection of a wide-orbit planetary-mass companion to a solar-type Sco-Cen member. *MNRAS*, 492 (1):431–443, February 2020a. doi: 10.1093/mnras/stz3462.

Alexander J. Bohn, Matthew A. Kenworthy, Christian Ginski, Steven Rieder, Eric E. Mamajek, Tiffany Meshkat, Mark J. Pecaut, Maddalena Reggiani, Jozua de Boer, Christoph U. Keller, Frans Snik, and John Southworth. Two Directly Imaged, Wide-orbit Giant Planets around the Young, Solar Analog TYC 8998-760-1. *ApJL*, 898(1):L16, July 2020b. doi: 10.3847/2041-8213/aba27e.

Alexander J. Bohn, Christian Ginski, Matthew A. Kenworthy, Eric E. Mamajek, Mark J. Pecaut, Markus Mugrauer, Nikolaus Vogt, Christian Adam, Tiffany Meshkat, Maddalena Reggiani, and Frans Snik. Discovery of a directly imaged planet to the young solar analog YSES 2. *A&A*, 648:A73, April 2021. doi: 10.1051/0004-6361/202140508.

Markus Bonse, Emily Garvin, Timothy Gebhard, Felix Dannert, Gabriele Cugno, and Sascha Quanz. Comparing Apples with Apples: Statistically sound Detection Limits for Exoplanet High Contrast Imaging. In *Bulletin of the American Astronomical Society*, volume 54, page 102.392, June 2022.

Brendan P. Bowler and Eric L. Nielsen. Occurrence Rates from Direct Imaging Surveys. In Hans J. Deeg and Juan Antonio Belmonte, editors, *Handbook of Exoplanets*, page 155. Springer, 2018. doi: 10.1007/978-3-319-55333-7_155.

Marcel Carbillet, Philippe Bendjoya, Lyu Abe, Géraldine Guerri, Anthony Boccaletti, Jean-Baptiste Daban, Kjetil Dohlen, André Ferrari, Sylvie Robbe-Dubois, Richard Douet, and Farrokh Vakili. Apodized Lyot coronagraph for SPHERE/VLT. I. Detailed numerical study. *ExA*, 30(1):39–58, May 2011. doi: 10.1007/s10686-011-9219-4.

G. Chauvin, A. M. Lagrange, C. Dumas, B. Zuckerman, D. Mouillet, I. Song, J. L. Beuzit, and P. Lowrance. A giant planet candidate near a young brown dwarf. Direct VLT/NACO observations using IR wavefront sensing. *A&A*, 425:L29–L32, October 2004. doi: 10.1051/0004-6361:200400056.

G. Chauvin, A. M. Lagrange, C. Dumas, B. Zuckerman, D. Mouillet, I. Song, J. L. Beuzit, and P. Lowrance. Giant planet companion to 2MASSW J1207334-393254. *A&A*, 438(2):L25–L28, August 2005. doi: 10.1051/0004-6361:200500116.

R. U. Claudi, M. Turatto, J. Antichi, R. Gratton, S. Scuderi, E. Cascone, D. Mesa, S. Desidera, A. Baruffolo, A. Berton, P. Bagnara, E. Giro, P. Bruno, D. Fantinel, J. L. Beuzit, P. Puget, and K. Dohlen. The integral field spectrograph of SPHERE: the planet finder for VLT. In Ian S. McLean and Masanori Iye, editors, *Ground-based and Airborne Instrumentation for Astronomy*, volume 6269 of *Society of Photo-Optical Instrumentation Engineers (SPIE) Conference Series*, page 62692Y, June 2006. doi: 10.1117/12.671949.

R. U. Claudi, M. Turatto, R. G. Gratton, J. Antichi, M. Bonavita, P. Bruno, E. Cascone, V. De Caprio, S. Desidera, E. Giro, D. Mesa, S. Scuderi, K. Dohlen, J. L. Beuzit, and P. Puget. SPHERE IFS: the spectro differential imager of the VLT for exoplanets search. In Ian S. McLean and Mark M. Casali, editors, *Ground-based and Airborne Instrumentation for Astronomy II*, volume 7014 of *Society of Photo-Optical Instrumentation Engineers (SPIE) Conference Series*, page 70143E, July 2008. doi: 10.1117/12.788366.

T. Currie, B. Biller, A. Lagrange, C. Marois, O. Guyon, E. L. Nielsen, M. Bonnefoy, and R. J. De Rosa. Direct Imaging and Spectroscopy of Extrasolar Planets. In S. Inutsuka, Y. Aikawa, T. Muto, K. Tomida, and M. Tamura, editors, *Protostars and Planets VII*, volume 534 of *Astronomical Society of the Pacific Conference Series*, page 799, July 2023. doi: 10.48550/arXiv.2205.05696.

Thayne Currie, Timothy D. Brandt, Masayuki Kuzuhara, Jeffrey Chilcote, Olivier Guyon, Christian Marois, Tyler D. Groff, Julien Lozi, Sebastien Vievard, Ananya Sahoo, Vincent Deo, Nemanja Jovanovic, Frantz Martinache, Kevin Wagner, Trent Dupuy, Matthew Wahl, Michael Letawsky, Yiting Li, Yunlin Zeng, G. Mirek Brandt, Daniel Michalik, Carol Grady, Markus Janson, Gillian R. Knapp,

Jungmi Kwon, Kellen Lawson, Michael W. McElwain, Taichi Uyama, John Wisniewski, and Moto-hide Tamura. SCExAO/CHARIS Direct Imaging Discovery of a 20 au Separation, Low-mass Ratio Brown Dwarf Companion to an Accelerating Sun-like Star. *ApJL*, 904(2):L25, December 2020. doi: 10.3847/2041-8213/abc631.

Thayne Currie, Timothy D. Brandt, Masayuki Kuzuhara, Jeffrey Chilcote, Edward Cashman, R. Y. Liu, Kellen Lawson, Taylor Tobin, G. Mirek Brandt, Olivier Guyon, Julien Lozi, Vincent Deo, Sebastien Vievard, Kyoohun Ahn, and Nour Skaf. A new type of exoplanet direct imaging search: a SCExAO/CHARIS survey of accelerating stars. In Stuart B. Shaklan and Garreth J. Ruane, editors, *Techniques and Instrumentation for Detection of Exoplanets X*, volume 11823 of *Society of Photo-Optical Instrumentation Engineers (SPIE) Conference Series*, page 1182304, September 2021. doi: 10.1117/12.2595001.

P. T. de Zeeuw, R. Hoogerwerf, J. H. J. de Bruijne, A. G. A. Brown, and A. Blaauw. A HIPPARCOS Census of the Nearby OB Associations. *AJ*, 117(1):354–399, January 1999. doi: 10.1086/300682.

S. Desidera, R. Gratton, R. Claudi, J. Antichi, D. Mesa, M. Turatto, P. Bruno, E. Cascone, V. De Caprio, E. Giro, S. Scuderi, M. Feldt, A. Pavlov, O. Moeller-Nilsson, K. Dohlen, J. L. Beuzit, D. Mouillet, P. Puget, and F. Wildi. Calibration and data reduction for planet detection with SPHERE-IFS. In Ian S. McLean and Mark M. Casali, editors, *Ground-based and Airborne Instrumentation for Astronomy II*, volume 7014 of *Society of Photo-Optical Instrumentation Engineers (SPIE) Conference Series*, page 70143M, July 2008. doi: 10.1117/12.789153.

S. Desidera, G. Chauvin, M. Bonavita, S. Messina, H. LeCoroller, T. Schmidt, R. Gratton, C. Lazzoni, M. Meyer, J. Schlieder, A. Cheetham, J. Hagelberg, M. Bonnefoy, M. Feldt, A. M. Lagrange, M. Langlois, A. Vigan, T. G. Tan, F. J. Hambsch, M. Millward, J. Alcalá, S. Benatti, W. Brandner, J. Carson, E. Covino, P. Delorme, V. D'Orazi, M. Janson, E. Rigliaco, J. L. Beuzit, B. Biller, A. Boccaletti, C. Dominik, F. Cantalloube, C. Fontanive, R. Galicher, Th. Henning, E. Lagadec, R. Ligi, A. L. Maire, F. Menard, D. Mesa, A. Müller, M. Samland, H. M. Schmid, E. Sissa, M. Turatto, S. Udry, A. Zurlo, R. Asensio-Torres, T. Kopytova, E. Rickman, L. Abe, J. Antichi, A. Baruffolo, P. Baudoz, J. Baudrand, P. Blanchard, A. Bazzon, T. Buey, M. Carbillet, M. Carle, J. Charton, E. Cascone, R. Claudi, A. Costille, A. Deboulbé, V. De Caprio, K. Dohlen, D. Fantinel, P. Feautrier, T. Fusco, P. Gigan, E. Giro, D. Gisler, L. Gluck, N. Hubin, E. Hugot, M. Jaquet, M. Kasper, F. Madec, Y. Magnard, P. Martinez, D. Maurel, D. Le Mignant, O. Möller-Nilsson, M. Llored, T. Moulin, A. Origné, A. Pavlov, D. Perret, C. Petit, J. Pragt, P. Puget, P. Rabou, J. Ramos, F. Rigal, S. Rochat, R. Roelfsema, G. Rousset, A. Roux, B. Salasnich, J. F. Sauvage, A. Sevin, C. Soenke, E. Stadler, M. Suarez, L. Weber, and F. Wildi. The SPHERE infrared survey for exoplanets (SHINE). I. Sample definition and target characterization. *A&A*, 651:A70, July 2021. doi: 10.1051/0004-6361/202038806.

Kjetil Dohlen, Maud Langlois, Michel Saisse, Lucien Hill, Alain Origne, Marc Jacquet, Christophe Fabron, Jean-Claude Blanc, Marc Llored, Michael Carle, Claire Moutou, Arthur Vigan, Anthony Boccaletti, Marcel Carbillet, David Mouillet, and Jean-Luc Beuzit. The infra-red dual imaging and spectrograph for SPHERE: design and performance. In Ian S. McLean and Mark M. Casali, editors, *Ground-based and Airborne Instrumentation for Astronomy II*, volume 7014 of *Society of Photo-Optical Instrumentation Engineers (SPIE) Conference Series*, page 70143L, July 2008. doi: 10.1117/12.789786.

Gaspard Duchêne and Adam Kraus. Stellar Multiplicity. *ARA&A*, 51(1):269–310, August 2013. doi: 10.1146/annurev-astro-081710-102602.

E. D. Feigelson, W. A. Lawson, M. Stark, L. Townsley, and G. P. Garmire. 51 Eridani and GJ 3305: A 10-15 Myr old Binary Star System at 30 Parsecs. *AJ*, 131(3):1730–1739, March 2006. doi: 10.1086/499923.

W. Freudling, M. Romaniello, D. M. Bramich, P. Ballester, V. Forchi, C. E. García-Dabló, S. Moehler, and M. J. Neeser. Automated data reduction workflows for astronomy. The ESO Reflex environment. *A&A*, 559:A96, November 2013. doi: 10.1051/0004-6361/201322494.

T. Fusco, J. F. Sauvage, D. Mouillet, A. Costille, C. Petit, J. L. Beuzit, K. Dohlen, J. Milli, J. Girard, M. Kasper, A. Vigan, M. Suarez, C. Soenke, M. Downing, M. N'Diaye, P. Baudoz, A. Sevin, A. Baruffolo, H. M. Schmid, B. Salasnich, E. Hugot, and N. Hubin. SAXO, the SPHERE extreme AO system:

on-sky final performance and future improvements. In Enrico Marchetti, Laird M. Close, and Jean-Pierre Véran, editors, *Adaptive Optics Systems V*, volume 9909 of *Society of Photo-Optical Instrumentation Engineers (SPIE) Conference Series*, page 99090U, July 2016. doi: 10.1117/12.2233319.

Alexandra Z. Greenbaum, Laurent Pueyo, Jean-Baptiste Ruffio, Jason J. Wang, Robert J. De Rosa, Jonathan Aguilar, Julien Rameau, Travis Barman, Christian Marois, Mark S. Marley, Quinn Konopacky, Abhijith Rajan, Bruce Macintosh, Megan Ansdell, Pauline Arriaga, Vanessa P. Bailey, Joanna Bulger, Adam S. Burrows, Jeffrey Chilcote, Tara Cotten, Rene Doyon, Gaspard Duchêne, Michael P. Fitzgerald, Katherine B. Follette, Benjamin Gerard, Stephen J. Goodsell, James R. Graham, Pascale Hibon, Li-Wei Hung, Patrick Ingraham, Paul Kalas, James E. Larkin, Jérôme Maire, Franck Marchis, Stanimir Metchev, Maxwell A. Millar-Blanchaer, Eric L. Nielsen, Andrew Norton, Rebecca Oppenheimer, David Palmer, Jennifer Patience, Marshall D. Perrin, Lisa Poyneer, Fredrik T. Rantakyrö, Dmitry Savransky, Adam C. Schneider, Anand Sivaramakrishnan, Inseok Song, Rémi Soummer, Sandrine Thomas, J. Kent Wallace, Kimberly Ward-Duong, Sloane Wiktorowicz, and Schuyler Wolff. GPI Spectra of HR 8799 c, d, and e from 1.5 to 2.4 μm with KLIP Forward Modeling. *AJ*, 155(6):226, June 2018. doi: 10.3847/1538-3881/aabcb8.

S. Y. Haffert, A. J. Bohn, J. de Boer, I. A. G. Snellen, J. Brinchmann, J. H. Girard, C. U. Keller, and R. Bacon. Two accreting protoplanets around the young star PDS 70. *NatAs*, 3:749–754, June 2019. doi: 10.1038/s41550-019-0780-5.

Yoichi Itoh, Masahiko Hayashi, Motohide Tamura, Takashi Tsuji, Yumiko Oasa, Misato Fukagawa, Saeko S. Hayashi, Takahiro Naoi, Miki Ishii, Satoshi Mayama, Jun-ichi Morino, Takuya Yamashita, Tae-Soo Pyo, Takayuki Nishikawa, Tomonori Usuda, Koji Murakawa, Hiroshi Suto, Shin Oya, Naruhisa Takato, Hiroyasu Ando, Shoken M. Miyama, Naoto Kobayashi, and Norio Kaifu. A Young Brown Dwarf Companion to DH Tauri. *ApJ*, 620(2):984–993, February 2005. doi: 10.1086/427086.

J. C. Kapteyn. On the individual parallaxes of the brighter galactic helium stars in the southern hemisphere, together with considerations on the parallax of stars in general. *ApJ*, 40:43–126, July 1914. doi: 10.1086/142098.

Matthew Kenworthy, Alexander Bohn, Christian Ginski, Maddalena Reggiani, Tiffany Meshkat, Eric Mamajek, Mark Pecaut, and Frans Snik. The Young Suns Exoplanet Survey: imaging infant planets around young, solar analogs. In *European Planetary Science Congress*, pages EPSC2021–35, September 2021. doi: 10.5194/epsc2021-35.

M. Keppler, M. Benisty, A. Müller, Th. Henning, R. van Boekel, F. Cantalloube, C. Ginski, R. G. van Holstein, A. L. Maire, A. Pohl, M. Samland, H. Avenhaus, J. L. Baudino, A. Boccaletti, J. de Boer, M. Bonnefoy, G. Chauvin, S. Desidera, M. Langlois, C. Lazzoni, G. D. Marleau, C. Mordasini, N. Pawellek, T. Stolker, A. Vigan, A. Zurlo, T. Birnstiel, W. Brandner, M. Feldt, M. Flock, J. Girard, R. Gratton, J. Hagelberg, A. Isella, M. Janson, A. Juhasz, J. Kemmer, Q. Kral, A. M. Lagrange, R. Launhardt, A. Matter, F. Ménard, J. Milli, P. Mollière, J. Olofsson, L. Pérez, P. Pinilla, C. Pinte, S. P. Quanz, T. Schmidt, S. Udry, Z. Wahhaj, J. P. Williams, E. Buenzli, M. Cudel, C. Dominik, R. Galicher, M. Kasper, J. Lannier, D. Mesa, D. Mouillet, S. Peretti, C. Perrot, G. Salter, E. Sissa, F. Wildi, L. Abe, J. Antichi, J. C. Augereau, A. Baruffolo, P. Baudoz, A. Bazzon, J. L. Beuzit, P. Blanchard, S. S. Brems, T. Buey, V. De Caprio, M. Carbillet, M. Carle, E. Cascone, A. Cheetham, R. Claudi, A. Costille, A. Delboulbé, K. Dohlen, D. Fantinel, P. Feautrier, T. Fusco, E. Giro, L. Gluck, C. Gry, N. Hubin, E. Hugot, M. Jaquet, D. Le Mignant, M. Llored, F. Madec, Y. Magnard, P. Martinez, D. Maurel, M. Meyer, O. Möller-Nilsson, T. Moulin, L. Mugnier, A. Origné, A. Pavlov, D. Perret, C. Petit, J. Pragt, P. Puget, P. Rabou, J. Ramos, F. Rigal, S. Rochat, R. Roelfsema, G. Rousset, A. Roux, B. Salasnich, J. F. Sauvage, A. Sevin, C. Soenke, E. Stadler, M. Suarez, M. Turatto, and L. Weber. Discovery of a planetary-mass companion within the gap of the transition disk around PDS 70. *A&A*, 617:A44, September 2018. doi: 10.1051/0004-6361/201832957.

S. Kiefer, A. J. Bohn, S. P. Quanz, M. Kenworthy, and T. Stolker. Spectral and angular differential imaging with SPHERE/IFS. Assessing the performance of various PCA-based approaches to PSF subtraction. *A&A*, 652:A33, August 2021. doi: 10.1051/0004-6361/202140285.

Q. M. Konopacky, C. Marois, B. A. Macintosh, R. Galicher, T. S. Barman, S. A. Metchev, and B. Zuckerman. Astrometric Monitoring of the HR 8799 Planets: Orbit Constraints from Self-consistent Measurements. *AJ*, 152(2):28, August 2016. doi: 10.3847/0004-6256/152/2/28.

M. Kuzuhara, M. Tamura, T. Kudo, M. Janson, R. Kandori, T. D. Brandt, C. Thalmann, D. Spiegel, B. Biller, J. Carson, Y. Hori, R. Suzuki, A. Burrows, T. Henning, E. L. Turner, M. W. McElwain, A. Moro-Martín, T. Suenaga, Y. H. Takahashi, J. Kwon, P. Lucas, L. Abe, W. Brandner, S. Egner, M. Feldt, H. Fujiwara, M. Goto, C. A. Grady, O. Guyon, J. Hashimoto, Y. Hayano, M. Hayashi, S. S. Hayashi, K. W. Hodapp, M. Ishii, M. Iye, G. R. Knapp, T. Matsuo, S. Mayama, S. Miyama, J. I. Morino, J. Nishikawa, T. Nishimura, T. Kotani, N. Kusakabe, T. S. Pyo, E. Serabyn, H. Suto, M. Takami, N. Takato, H. Terada, D. Tomono, M. Watanabe, J. P. Wisniewski, T. Yamada, H. Takami, and T. Usuda. Direct Imaging of a Cold Jovian Exoplanet in Orbit around the Sun-like Star GJ 504. *ApJ*, 774(1):11, September 2013. doi: 10.1088/0004-637X/774/1/11.

David Lafrenière, Christian Marois, René Doyon, and Travis Barman. HST/NICMOS Detection of HR 8799 b in 1998. *ApJL*, 694(2):L148–L152, April 2009. doi: 10.1088/0004-637X/694/2/L148.

A. M. Lagrange, D. Gratadour, G. Chauvin, T. Fusco, D. Ehrenreich, D. Mouillet, G. Rousset, D. Rouan, F. Allard, É. Gendron, J. Charton, L. Mugnier, P. Rabou, J. Montri, and F. Lacombe. A probable giant planet imaged in the β Pictoris disk. VLT/NaCo deep L'-band imaging. *A&A*, 493(2):L21–L25, January 2009. doi: 10.1051/0004-6361:200811325.

A. M. Lagrange, M. Bonnefoy, G. Chauvin, D. Apai, D. Ehrenreich, A. Boccaletti, D. Gratadour, D. Rouan, D. Mouillet, S. Lacour, and M. Kasper. A Giant Planet Imaged in the Disk of the Young Star β Pictoris. *Sci*, 329(5987):57, July 2010. doi: 10.1126/science.1187187.

A. M. Lagrange, Nadège Meunier, Pascal Rubini, Miriam Keppler, Franck Galland, Eric Chapellier, Eric Michel, Luis Balona, Hervé Beust, Tristan Guillot, Antoine Grandjean, Simon Borgniet, Djamel Mékarnia, Paul Anthony Wilson, Flavien Kiefer, Mickael Bonnefoy, Jorge Lillo-Box, Blake Pantoja, Matias Jones, Daniela Paz Iglesias, Laetitia Rodet, Matias Diaz, Abner Zapata, Lyu Abe, and François-Xavier Schmider. Evidence for an additional planet in the β Pictoris system. *NatAs*, 3:1135–1142, August 2019. doi: 10.1038/s41550-019-0857-1.

M. Langlois, R. Gratton, A. M. Lagrange, P. Delorme, A. Boccaletti, M. Bonnefoy, A. L. Maire, D. Mesa, G. Chauvin, S. Desidera, A. Vigan, A. Cheetham, J. Hagelberg, M. Feldt, M. Meyer, P. Rubini, H. Le Coroller, F. Cantalloube, B. Biller, M. Bonavita, T. Bhowmik, W. Brandner, S. Daemgen, V. D'Orazi, O. Flasseur, C. Fontanive, R. Galicher, J. Girard, P. Janin-Potiron, M. Janson, M. Keppler, T. Kopytova, E. Lagadec, J. Lannier, C. Lazzoni, R. Ligi, N. Meunier, A. Perreti, C. Perrot, L. Rodet, C. Romero, D. Rouan, M. Samland, G. Salter, E. Sissa, T. Schmidt, A. Zurlo, D. Mouillet, L. Denis, E. Thiébaut, J. Milli, Z. Wahhaj, J. L. Beuzit, C. Dominik, Th. Henning, F. Ménard, A. Müller, H. M. Schmid, M. Turatto, S. Udry, L. Abe, J. Antichi, F. Allard, A. Baruffolo, P. Baudoz, J. Baudrand, A. Bazzon, P. Blanchard, M. Carbillet, M. Carle, E. Cascone, J. Charton, R. Claudi, A. Costille, V. De Caprio, A. Delboulbé, K. Dohlen, D. Fantinel, P. Feautrier, T. Fusco, P. Gigan, E. Giro, D. Gisler, L. Gluck, C. Gry, N. Hubin, E. Hugot, M. Jaquet, M. Kasper, D. Le Mignant, M. Llored, F. Madec, Y. Magnard, P. Martinez, D. Maurel, S. Messina, O. Möller-Nilsson, L. Mugnier, T. Moulin, A. Origné, A. Pavlov, D. Perret, C. Petit, J. Pragt, P. Puget, P. Rabou, J. Ramos, F. Rigal, S. Rochat, R. Roelfsema, G. Rousset, A. Roux, B. Salasnich, J. F. Sauvage, A. Sevin, C. Soenke, E. Stadler, M. Suarez, L. Weber, F. Wildi, and E. Rickman. The SPHERE infrared survey for exoplanets (SHINE). II. Observations, data reduction and analysis, detection performances, and initial results. *A&A*, 651:A71, July 2021. doi: 10.1051/0004-6361/202039753.

B. Macintosh, J. R. Graham, T. Barman, R. J. De Rosa, Q. Konopacky, M. S. Marley, C. Marois, E. L. Nielsen, L. Pueyo, A. Rajan, J. Rameau, D. Saumon, J. J. Wang, J. Patience, M. Ammons, P. Arriaga, E. Artigau, S. Beckwith, J. Brewster, S. Bruzzone, J. Bulger, B. Burningham, A. S. Burrows, C. Chen, E. Chiang, J. K. Chilcote, R. I. Dawson, R. Dong, R. Doyon, Z. H. Draper, G. Duchêne, T. M. Esposito, D. Fabrycky, M. P. Fitzgerald, K. B. Follette, J. J. Fortney, B. Gerard, S. Goodsell, A. Z. Greenbaum, P. Hibon, S. Hinkley, T. H. Cotten, L. W. Hung, P. Ingraham, M. Johnson-Groh, P. Kalas, D. Lafreniere, J. E. Larkin, J. Lee, M. Line, D. Long, J. Maire, F. Marchis, B. C. Matthews, C. E. Max, S. Metchev, M. A. Millar-Blanchaer, T. Mittal, C. V. Morley, K. M. Morzinski, R. Murray-Clay, R. Oppenheimer,

D. W. Palmer, R. Patel, M. D. Perrin, L. A. Poyneer, R. R. Rafikov, F. T. Rantakyrö, E. L. Rice, P. Rojo, A. R. Rudy, J. B. Ruffio, M. T. Ruiz, N. Sadakuni, L. Saddlemyer, M. Salama, D. Savransky, A. C. Schneider, A. Sivaramakrishnan, I. Song, R. Soummer, S. Thomas, G. Vasisht, J. K. Wallace, K. Ward-Duong, S. J. Wiktorowicz, S. G. Wolff, and B. Zuckerman. Discovery and spectroscopy of the young jovian planet 51 Eri b with the Gemini Planet Imager. *Sci*, 350(6256):64–67, October 2015. doi: 10.1126/science.aac5891.

A. L. Maire, L. Rodet, F. Cantalloube, R. Galicher, W. Brandner, S. Messina, C. Lazzoni, D. Mesa, D. Melnick, J. Carson, M. Samland, B. A. Biller, A. Boccaletti, Z. Wahhaj, H. Beust, M. Bonnefoy, G. Chauvin, S. Desidera, M. Langlois, T. Henning, M. Janson, J. Olofsson, D. Rouan, F. Ménard, A. M. Lagrange, R. Gratton, A. Vigan, M. R. Meyer, A. Cheetham, J. L. Beuzit, K. Dohlen, H. Avenhaus, M. Bonavita, R. Claudi, M. Cudel, S. Daemgen, V. D'Orazi, C. Fontanive, J. Hagelberg, H. Le Coroller, C. Perrot, E. Rickman, T. Schmidt, E. Sissa, S. Udry, A. Zurlo, L. Abe, A. Origné, F. Rigal, G. Rousset, A. Roux, and L. Weber. Hint of curvature in the orbital motion of the exoplanet 51 Eridani b using 3 yr of VLT/SPHERE monitoring. *A&A*, 624:A118, April 2019. doi: 10.1051/0004-6361/201935031.

Mark S. Marley, Jonathan J. Fortney, Olenka Hubickyj, Peter Bodenheimer, and Jack J. Lissauer. On the Luminosity of Young Jupiters. *ApJ*, 655(1):541–549, January 2007. doi: 10.1086/509759.

Christian Marois, Bruce Macintosh, Travis Barman, B. Zuckerman, Inseok Song, Jennifer Patience, David Lafrenière, and René Doyon. Direct Imaging of Multiple Planets Orbiting the Star HR 8799. *Sci*, 322(5906):1348, November 2008. doi: 10.1126/science.1166585.

Christian Marois, B. Zuckerman, Quinn M. Konopacky, Bruce Macintosh, and Travis Barman. Images of a fourth planet orbiting HR 8799. *Natur*, 468(7327):1080–1083, December 2010. doi: 10.1038/nature09684.

Rebecca G. Martin and Mario Livio. The Solar System as an Exoplanetary System. *ApJ*, 810(2):105, September 2015. doi: 10.1088/0004-637X/810/2/105.

B. D. Mason, G. L. Wycoff, W. I. Hartkopf, G. G. Douglass, and C. E. Worley. VizieR Online Data Catalog: The Washington Visual Double Star Catalog (Mason+ 2001-2020). *yCat*, art. B/wds, September 2023.

D. Mawet, J. Milli, Z. Wahhaj, D. Pelat, O. Absil, C. Delacroix, A. Boccaletti, M. Kasper, M. Kenworthy, C. Marois, B. Mennesson, and L. Pueyo. Fundamental Limitations of High Contrast Imaging Set by Small Sample Statistics. *ApJ*, 792(2):97, September 2014. doi: 10.1088/0004-637X/792/2/97.

D. Mesa, R. Gratton, A. Zurlo, A. Vigan, R. U. Claudi, M. Alberi, J. Antichi, A. Baruffolo, J. L. Beuzit, A. Boccaletti, M. Bonnefoy, A. Costille, S. Desidera, K. Dohlen, D. Fantinel, M. Feldt, T. Fusco, E. Giro, T. Henning, M. Kasper, M. Langlois, A. L. Maire, P. Martinez, O. Moeller-Nilsson, D. Mouillet, C. Moutou, A. Pavlov, P. Puget, B. Salasnich, J. F. Sauvage, E. Sissa, M. Turatto, S. Udry, F. Vakili, R. Waters, and F. Wildi. Performance of the VLT Planet Finder SPHERE. II. Data analysis and results for IFS in laboratory. *A&A*, 576:A121, April 2015. doi: 10.1051/0004-6361/201423910.

P. Mollière, T. Stolker, S. Lacour, G. P. P. L. Otten, J. Shangguan, B. Charnay, T. Molyarova, M. Nowak, Th. Henning, G. D. Marleau, D. A. Semenov, E. van Dishoeck, F. Eisenhauer, P. Garcia, R. Garcia Lopez, J. H. Girard, A. Z. Greenbaum, S. Hinkley, P. Kervella, L. Kreidberg, A. L. Maire, E. Nasedkin, L. Pueyo, I. A. G. Snellen, A. Vigan, J. Wang, P. T. de Zeeuw, and A. Zurlo. Retrieving scattering clouds and disequilibrium chemistry in the atmosphere of HR 8799e. *A&A*, 640:A131, August 2020. doi: 10.1051/0004-6361/202038325.

Alessandro Morbidelli and Sean N. Raymond. Challenges in planet formation. *JGRE*, 121(10):1962–1980, October 2016. doi: 10.1002/2016JE005088.

R. Neuhäuser, E. W. Guenther, G. Wuchterl, M. Mugrauer, A. Bedalov, and P. H. Hauschildt. Evidence for a co-moving sub-stellar companion of GQ Lup. *A&A*, 435(1):L13–L16, May 2005. doi: 10.1051/0004-6361:200500104.

Eric L. Nielsen, Robert J. De Rosa, Bruce Macintosh, Jason J. Wang, Jean-Baptiste Ruffio, Eugene Chiang, Mark S. Marley, Didier Saumon, Dmitry Savransky, S. Mark Ammons, Vanessa P. Bailey, Travis Barman, Célia Blain, Joanna Bulger, Adam Burrows, Jeffrey Chilcote, Tara Cotten, Ian Czekala, Rene Doyon, Gaspard Duchêne, Thomas M. Esposito, Daniel Fabrycky, Michael P. Fitzgerald, Katherine B. Follette, Jonathan J. Fortney, Benjamin L. Gerard, Stephen J. Goodsell, James R. Graham, Alexandra Z. Greenbaum, Pascale Hibon, Sasha Hinkley, Lea A. Hirsch, Justin Hom, Li-Wei Hung, Rebekah Ilene Dawson, Patrick Ingraham, Paul Kalas, Quinn Konopacky, James E. Larkin, Eve J. Lee, Jonathan W. Lin, Jérôme Maire, Franck Marchis, Christian Marois, Stanimir Metchev, Maxwell A. Millar-Blanchaer, Katie M. Morzinski, Rebecca Oppenheimer, David Palmer, Jennifer Patience, Marshall Perrin, Lisa Poyneer, Laurent Pueyo, Roman R. Rafikov, Abhijith Rajan, Julien Rameau, Fredrik T. Rantakyrö, Bin Ren, Adam C. Schneider, Anand Sivaramakrishnan, Inseok Song, Remi Soummer, Melisa Tallis, Sandrine Thomas, Kimberly Ward-Duong, and Schuyler Wolff. The Gemini Planet Imager Exoplanet Survey: Giant Planet and Brown Dwarf Demographics from 10 to 100 au. *AJ*, 158(1):13, July 2019. doi: 10.3847/1538-3881/ab16e9.

M. Nowak, S. Lacour, A. M. Lagrange, P. Rubini, J. Wang, T. Stolker, R. Abuter, A. Amorim, R. Asensio-Torres, M. Bauböck, M. Benisty, J. P. Berger, H. Beust, S. Blunt, A. Boccaletti, M. Bonnefoy, H. Bonnet, W. Brandner, F. Cantalloube, B. Charnay, E. Choquet, V. Christiaens, Y. Clénet, V. Coudé Du Foresto, A. Cridland, P. T. de Zeeuw, R. Dembet, J. Dexter, A. Drescher, G. Duvert, A. Eckart, F. Eisenhauer, F. Gao, P. Garcia, R. Garcia Lopez, T. Gardner, E. Gendron, R. Genzel, S. Gillessen, J. Girard, A. Grandjean, X. Haubois, G. Heißel, T. Henning, S. Hinkley, S. Hippler, M. Horrobin, M. Houllé, Z. Hubert, A. Jiménez-Rosales, L. Jocou, J. Kammerer, P. Kervella, M. Keppler, L. Kreidberg, M. Kulikauskas, V. Lapeyrère, J. B. Le Bouquin, P. Léna, A. Mérand, A. L. Maire, P. Mollière, J. D. Monnier, D. Mouillet, A. Müller, E. Nasedkin, T. Ott, G. Otten, T. Paumard, C. Paladini, K. Perraut, G. Perrin, L. Pueyo, O. Pfuhl, J. Rameau, L. Rodet, G. Rodríguez-Coira, G. Rousset, S. Scheithauer, J. Shangguan, J. Stadler, O. Straub, C. Straubmeier, E. Sturm, L. J. Tacconi, E. F. van Dishoeck, A. Vigan, F. Vincent, S. D. von Fellenberg, K. Ward-Duong, F. Widmann, E. Wieprecht, E. Wiezorrek, J. Woillez, and GRAVITY Collaboration. Direct confirmation of the radial-velocity planet β Pictoris c. *A&A*, 642:L2, October 2020. doi: 10.1051/0004-6361/202039039.

Mark Pecaut and E. Mamajek. The Star-formation History and Accretion Disk Fraction Among the F-Type Members of the Scorpius-Centaurus OB Association. In *American Astronomical Society Meeting Abstracts #215*, volume 215 of *American Astronomical Society Meeting Abstracts*, page 455.30, January 2010.

Mark J. Pecaut and Eric E. Mamajek. The star formation history and accretion-disc fraction among the K-type members of the Scorpius-Centaurus OB association. *MNRAS*, 461(1):794–815, September 2016. doi: 10.1093/mnras/stw1300.

M. W. Phillips, P. Tremblin, I. Baraffe, G. Chabrier, N. F. Allard, F. Spiegelman, J. M. Goyal, B. Drummond, and E. Hébrard. A new set of atmosphere and evolution models for cool T-Y brown dwarfs and giant exoplanets. *A&A*, 637:A38, May 2020. doi: 10.1051/0004-6361/201937381.

Lisa A. Poyneer and Bruce A. Macintosh. Wavefront control for extreme adaptive optics. In Robert K. Tyson and Michael Lloyd-Hart, editors, *Astronomical Adaptive Optics Systems and Applications*, volume 5169 of *Society of Photo-Optical Instrumentation Engineers (SPIE) Conference Series*, pages 190–200, December 2003. doi: 10.1117/12.506456.

Anand Sivaramakrishnan, Christopher D. Koresko, Russell B. Makidon, Thomas Berkefeld, and Marc J. Kuchner. Ground-based Coronagraphy with High-order Adaptive Optics. *ApJ*, 552(1):397–408, May 2001. doi: 10.1086/320444.

B. A. Smith and R. J. Terrile. A Circumstellar Disk around β Pictoris. *Sci*, 226(4681):1421–1424, December 1984. doi: 10.1126/science.226.4681.1421.

T. Stolker, M. J. Bonse, S. P. Quanz, A. Amara, G. Cugno, A. J. Bohn, and A. Boehle. PynPoint: a modular pipeline architecture for processing and analysis of high-contrast imaging data. *A&A*, 621: A59, January 2019. doi: 10.1051/0004-6361/201834136.

Ronald C. Stone. A Comparison of Digital Centering Algorithms. *AJ*, 97:1227, April 1989. doi: 10.1086/115066.

K. Y. L. Su, G. H. Rieke, K. R. Stapelfeldt, R. Malhotra, G. Bryden, P. S. Smith, K. A. Misselt, A. Moro-Martin, and J. P. Williams. The Debris Disk Around HR 8799. *ApJ*, 705(1):314–327, November 2009. doi: 10.1088/0004-637X/705/1/314.

C. Thalmann, G. D. Mulders, M. Janson, J. Olofsson, M. Benisty, H. Avenhaus, S. P. Quanz, H. M. Schmid, T. Henning, E. Buenzli, F. Ménard, J. C. Carson, A. Garufi, S. Messina, C. Dominik, J. Leisenring, G. Chauvin, and M. R. Meyer. Optical Imaging Polarimetry of the LkCa 15 Protoplanetary Disk with SPHERE ZIMPOL. *ApJL*, 808(2):L41, August 2015. doi: 10.1088/2041-8205/808/2/L41.

Christian Thalmann, Hans M. Schmid, Anthony Boccaletti, David Mouillet, Kjetil Dohlen, Ronald Roelfsema, Marcel Carbillet, Daniel Gisler, Jean-Luc Beuzit, Markus Feldt, Raffaele Gratton, Franco Joos, Christoph U. Keller, II Kragt, Jan, Johan H. Pragt, Pascal Puget, Florence Rigal, Frans Snik, Rens Waters, and François Wildi. SPHERE ZIMPOL: overview and performance simulation. In Ian S. McLean and Mark M. Casali, editors, *Ground-based and Airborne Instrumentation for Astronomy II*, volume 7014 of *Society of Photo-Optical Instrumentation Engineers (SPIE) Conference Series*, page 70143F, July 2008. doi: 10.1117/12.789158.

A. Vigan, C. Moutou, M. Langlois, F. Allard, A. Boccaletti, M. Carbillet, D. Mouillet, and I. Smith. Photometric characterization of exoplanets using angular and spectral differential imaging. *MNRAS*, 407 (1):71–82, September 2010. doi: 10.1111/j.1365-2966.2010.16916.x.

A. Vigan, C. Fontanive, M. Meyer, B. Biller, M. Bonavita, M. Feldt, S. Desidera, G. D. Marleau, A. Emsenhuber, R. Galicher, K. Rice, D. Forgan, C. Mordasini, R. Gratton, H. Le Coroller, A. L. Maire, F. Cantalloube, G. Chauvin, A. Cheetham, J. Hagelberg, A. M. Lagrange, M. Langlois, M. Bonnefoy, J. L. Beuzit, A. Boccaletti, V. D'Orazi, P. Delorme, C. Dominik, Th. Henning, M. Janson, E. Lagadec, C. Lazzoni, R. Ligi, F. Menard, D. Mesa, S. Messina, C. Moutou, A. Müller, C. Perrot, M. Samland, H. M. Schmid, T. Schmidt, E. Sissa, M. Turatto, S. Udry, A. Zurlo, L. Abe, J. Antichi, R. Asensio-Torres, A. Baruffolo, P. Baudoz, J. Baudrand, A. Bazzon, P. Blanchard, A. J. Bohn, S. Brown Sevilla, M. Carbillet, M. Carle, E. Cascone, J. Charton, R. Claudi, A. Costille, V. De Caprio, A. Delboulbé, K. Dohlen, N. Engler, D. Fantinel, P. Feautrier, T. Fusco, P. Gigan, J. H. Girard, E. Giro, D. Gisler, L. Gluck, C. Gry, N. Hubin, E. Hugot, M. Jaquet, M. Kasper, D. Le Mignant, M. Llored, F. Madec, Y. Magnard, P. Martinez, D. Maurel, O. Möller-Nilsson, D. Mouillet, T. Moulin, A. Origné, A. Pavlov, D. Perret, C. Petit, J. Pragt, P. Puget, P. Rabou, J. Ramos, E. L. Rickman, F. Rigal, S. Rochat, R. Roelfsema, G. Rousset, A. Roux, B. Salasnich, J. F. Sauvage, A. Sevin, C. Soenke, E. Stadler, M. Suarez, Z. Wahhaj, L. Weber, and F. Wildi. The SPHERE infrared survey for exoplanets (SHINE). III. The demographics of young giant exoplanets below 300 au with SPHERE. *A&A*, 651:A72, July 2021. doi: 10.1051/0004-6361/202038107.

Arthur Vigan. vlt-sphere: Automatic VLT/SPHERE data reduction and analysis. Astrophysics Source Code Library, record ascl:2009.002, September 2020.

Jason J. Wang, James R. Graham, Rebekah Dawson, Daniel Fabrycky, Robert J. De Rosa, Laurent Pueyo, Quinn Konopacky, Bruce Macintosh, Christian Marois, Eugene Chiang, S. Mark Ammons, Pauline Arriaga, Vanessa P. Bailey, Travis Barman, Joanna Bulger, Jeffrey Chilcote, Tara Cotten, Rene Doyon, Gaspard Duchêne, Thomas M. Esposito, Michael P. Fitzgerald, Katherine B. Follette, Benjamin L. Gerard, Stephen J. Goodsell, Alexandra Z. Greenbaum, Pascale Hibon, Li-Wei Hung, Patrick Ingraham, Paul Kalas, James E. Larkin, Jérôme Maire, Franck Marchis, Mark S. Marley, Stanimir Metchev, Maxwell A. Millar-Blanchaer, Eric L. Nielsen, Rebecca Oppenheimer, David Palmer, Jennifer Patience, Marshall Perrin, Lisa Poyneer, Abhijith Rajan, Julien Rameau, Fredrik T. Rantakyrö, Jean-Baptiste Ruffio, Dmitry Savransky, Adam C. Schneider, Anand Sivaramakrishnan, Inseok Song, Remi Soummer, Sandrine Thomas, J. Kent Wallace, Kimberly Ward-Duong, Sloane Wiktorowicz, and Schuyler Wolff. Dynamical Constraints on the HR 8799 Planets with GPI. *AJ*, 156 (5):192, November 2018. doi: 10.3847/1538-3881/aae150.

Zhoujian Zhang, Michael C. Liu, J. J. Hermes, Eugene A. Magnier, Mark S. Marley, Pier-Emmanuel Tremblay, Michael A. Tucker, Aaron Do, Anna V. Payne, and Benjamin J. Shappee. COol Companions ON Ultrawide orbiTS (COCONUTS). I. A High-gravity T4 Benchmark around an Old White

Dwarf and a Re-examination of the Surface-gravity Dependence of the L/T Transition. *ApJ*, 891(2): 171, March 2020. doi: 10.3847/1538-4357/ab765c.

Zhoujian Zhang, Michael C. Liu, Zachary R. Claytor, William M. J. Best, Trent J. Dupuy, and Robert J. Siverd. The Second Discovery from the COCONUTS Program: A Cold Wide-orbit Exoplanet around a Young Field M Dwarf at 10.9 pc. *ApJL*, 916(2):L11, August 2021. doi: 10.3847/2041-8213/ac1123.

Zhoujian Zhang, Michael C. Liu, Caroline V. Morley, Eugene A. Magnier, Michael A. Tucker, Zachary P. Vanderbosch, Aaron Do, and Benjamin J. Shappee. COol Companions ON Ultrawide orbiTS (CO-CONUTS). III. A Very Red L6 Benchmark Brown Dwarf around a Young M5 Dwarf. *ApJ*, 935(1):15, August 2022. doi: 10.3847/1538-4357/ac7ce9.

Part IV

Appendix

A
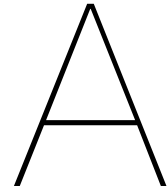
Other Observations

Here the coadded images from the reduced and subtracted cubes are shown for all systems where companions were not detected. For targets that were observed more than once (see Table 8.1) only the latest observation of is shown. However, all of these observations were analyzed, and no candidate companions were visible in the earlier observations either.
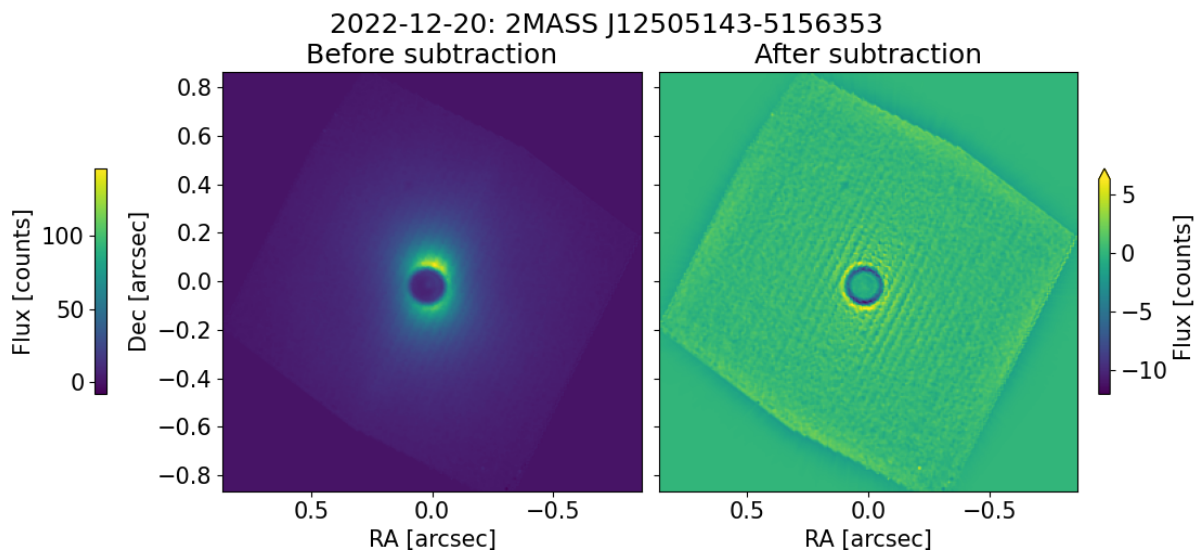
Figure A.1: Coadded cubes for the observation of 2MASS J12505143-5156353. The cubes have been derotated such that north is up and east is left. The square shape visible in the images is the shape of the detector, with part cut off due to the offset of the detector with respect to the IFU.
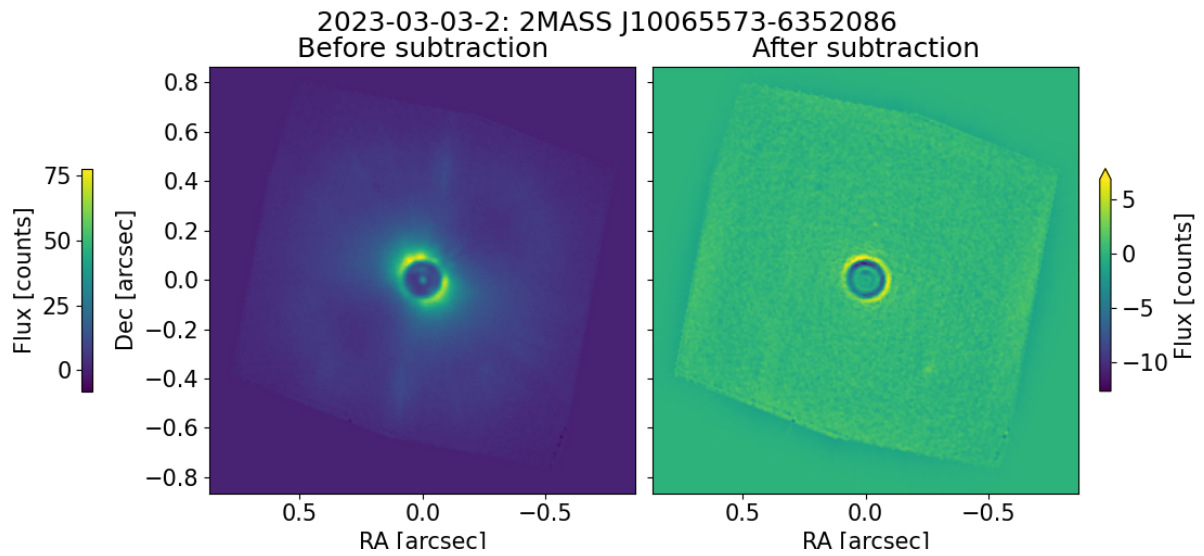
Figure A.2: Coadded cubes for the observation of 2MASS J10065573-6352086. The cubes have been derotated such that north is up and east is left. The square shape visible in the images is the shape of the detector, with part cut off due to the offset of the detector with respect to the IFU.
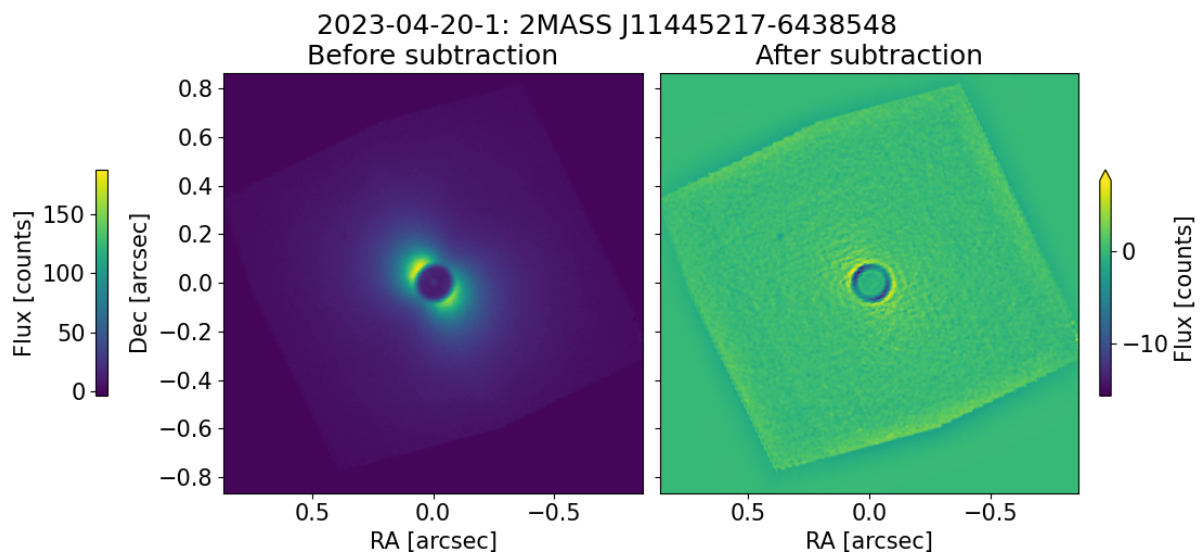
Figure A.3: Coadded cubes for the observation of 2MASS J11445217-6438548. The cubes have been derotated such that north is up and east is left. The square shape visible in the images is the shape of the detector, with part cut off due to the offset of the detector with respect to the IFU.
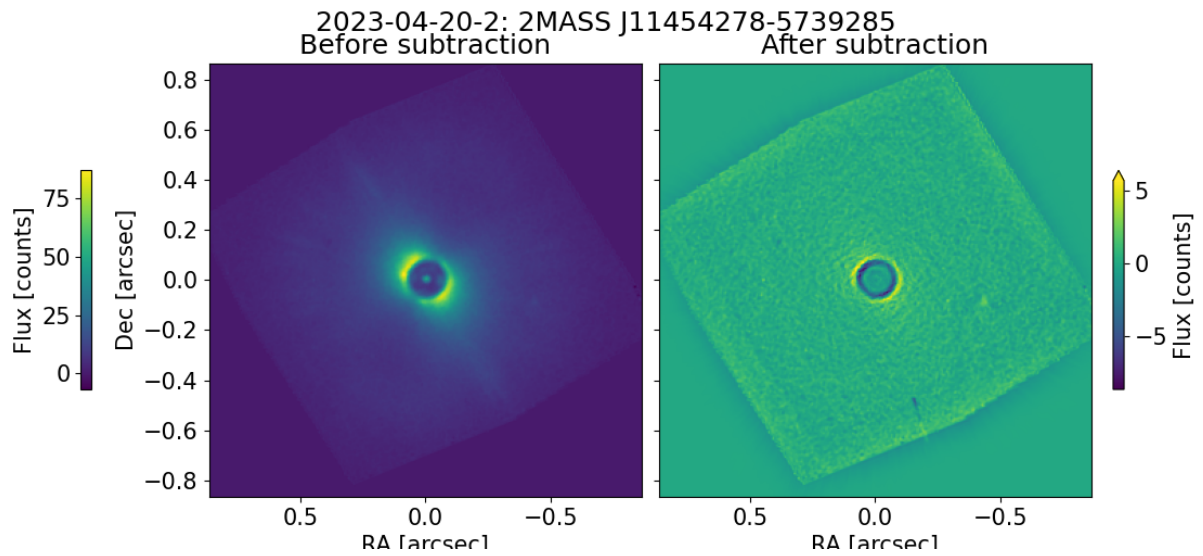
Figure A.4: Coadded cubes for the observation of 2MASS J11454278-5739285. The cubes have been derotated such that north is up and east is left. The square shape visible in the images is the shape of the detector, with part cut off due to the offset of the detector with respect to the IFU.
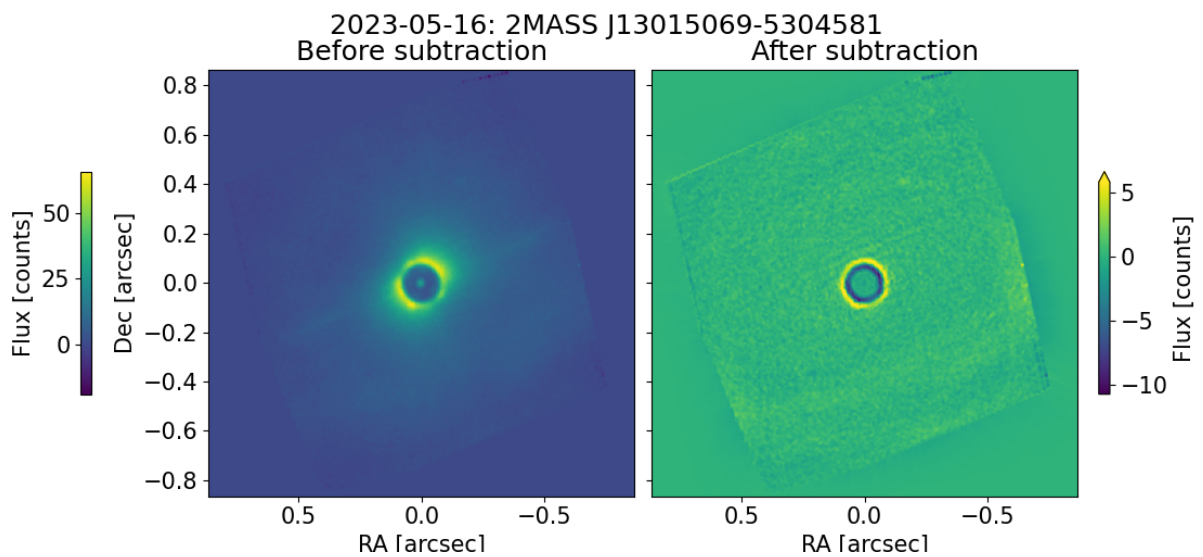
Figure A.5: Coadded cubes for the observation of 2MASS J13015069-5304581. The cubes have been derotated such that north is up and east is left. The square shape visible in the images is the shape of the detector, with part cut off due to the offset of the detector with respect to the IFU.
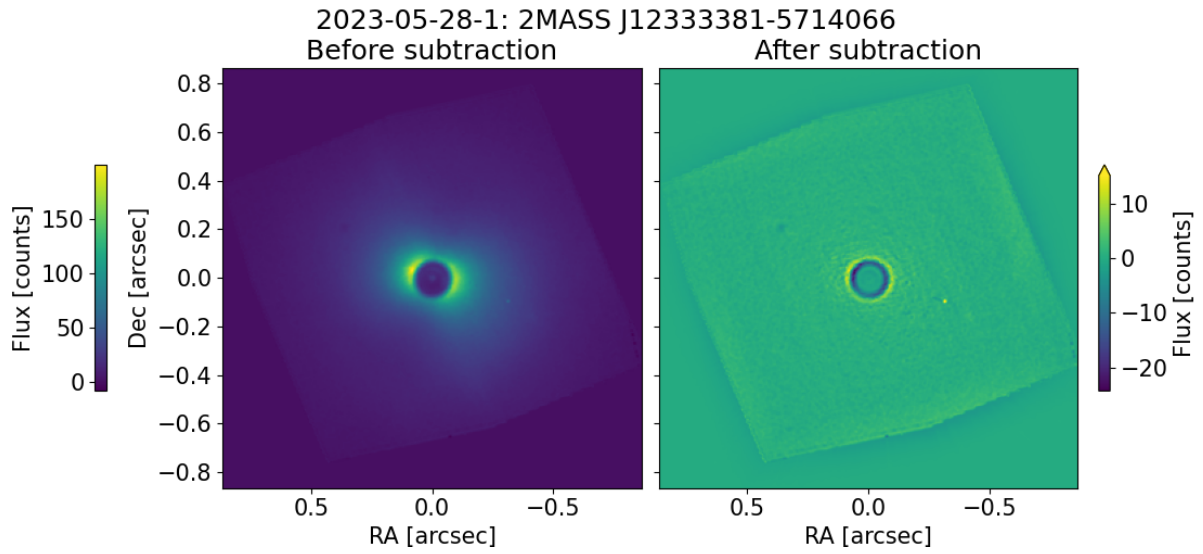
Figure A.6: Coadded cubes for the observation of 2MASS J12333381-5714066. The cubes have been derotated such that north is up and east is left. The square shape visible in the images is the shape of the detector, with part cut off due to the offset of the detector with respect to the IFU.
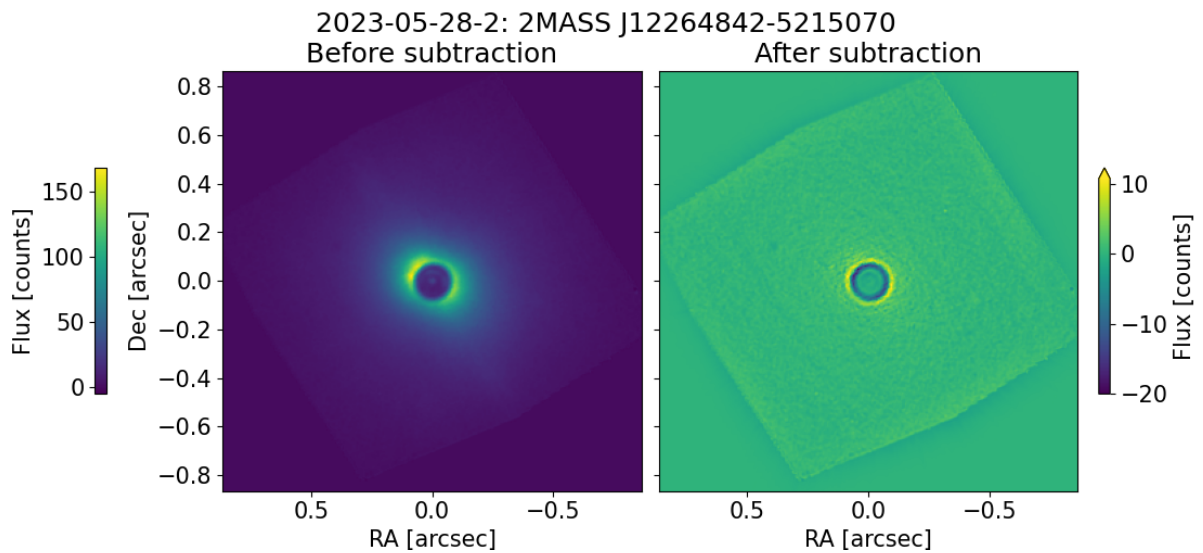
Figure A.7: Coadded cubes for the observation of 2MASS J12264842-5215070. The cubes have been derotated such that north is up and east is left. The square shape visible in the images is the shape of the detector, with part cut off due to the offset of the detector with respect to the IFU.
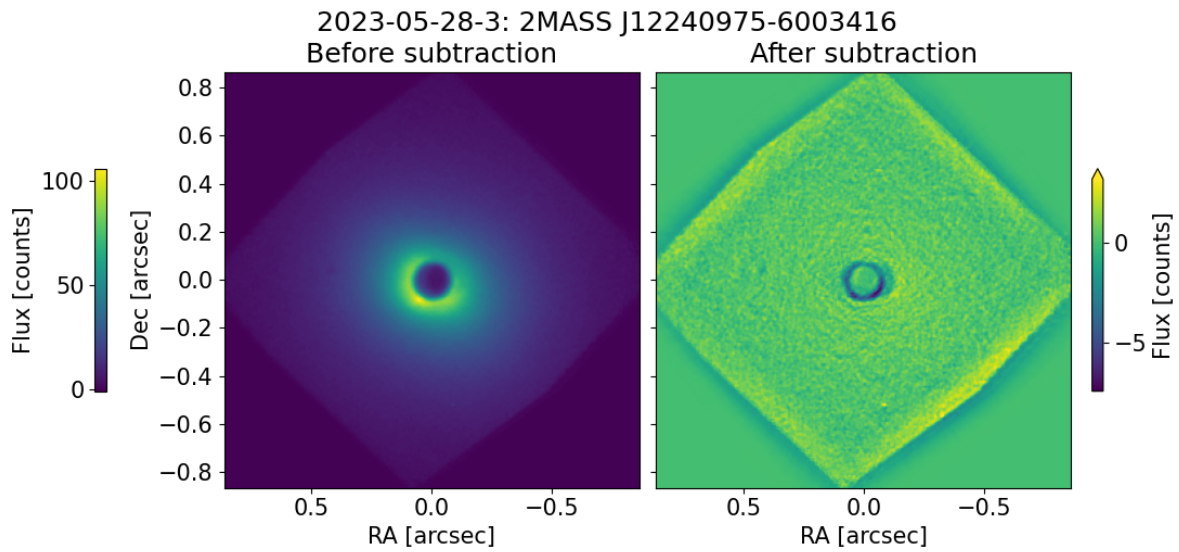
Figure A.8: Coadded cubes for the observation of 2MASS J12240975-6003416. The cubes have been derotated such that north is up and east is left. The square shape visible in the images is the shape of the detector, with part cut off due to the offset of the detector with respect to the IFU.
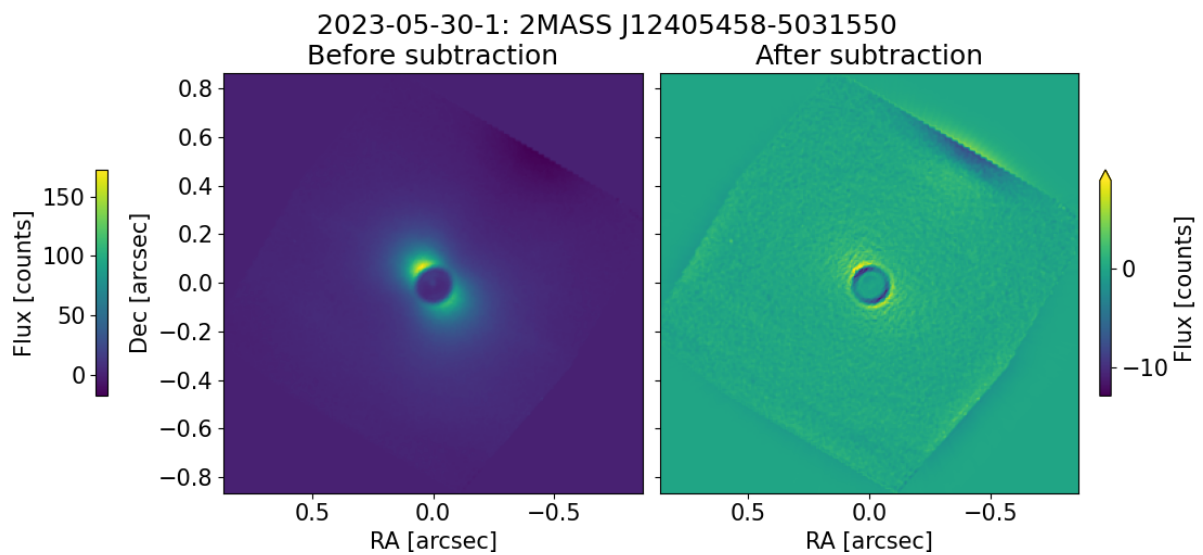
Figure A.9: Coadded cubes for the observation of 2MASS J12405458-5031550. The cubes have been derotated such that north is up and east is left. The square shape visible in the images is the shape of the detector, with part cut off due to the offset of the detector with respect to the IFU.

2023-05-30-3: 2MASS J12391404-5454469
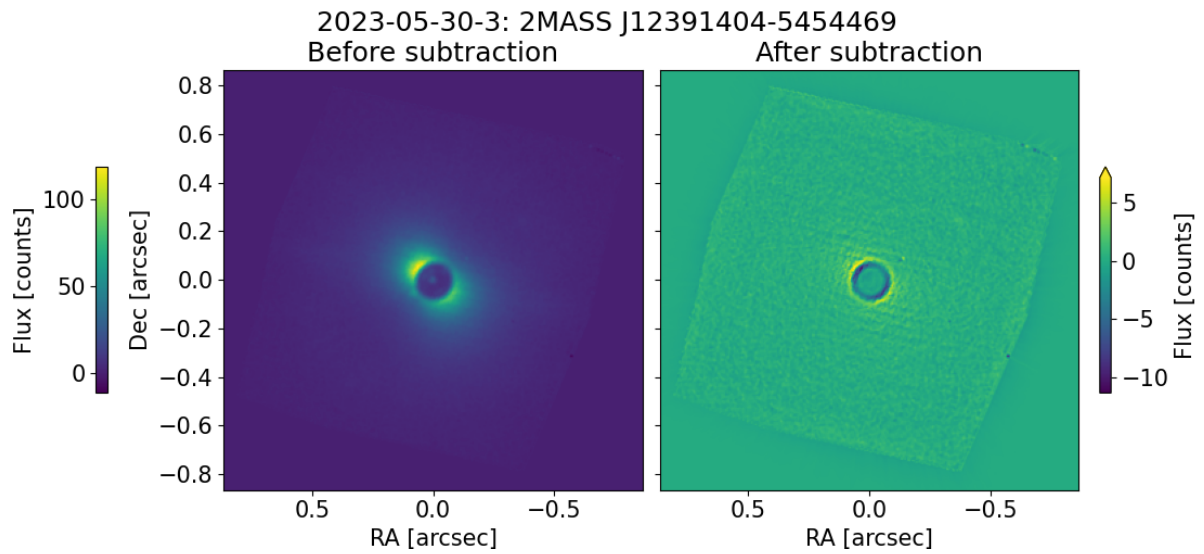
Figure A.10: Coadded cubes for the observation of 2MASS J12391404-5454469. The cubes have been derotated such that north is up and east is left. The square shape visible in the images is the shape of the detector, with part cut off due to the offset of the detector with respect to the IFU.

2023-06-15-2: 2MASS J13064012-5159386
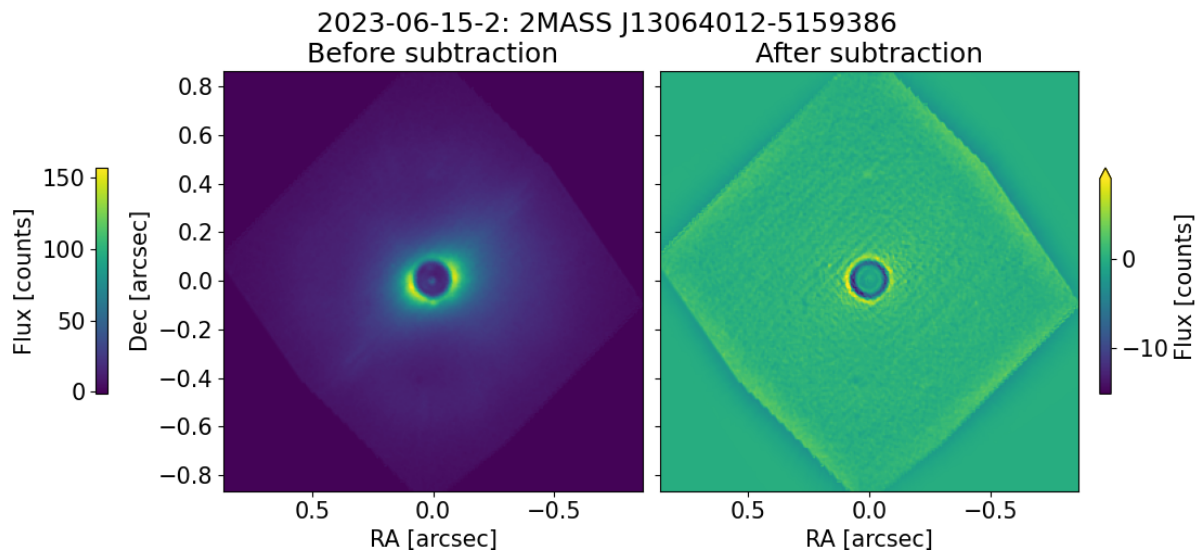
Figure A.11: Coadded cubes for the observation of 2MASS J13064012-5159386. The cubes have been derotated such that north is up and east is left. The square shape visible in the images is the shape of the detector, with part cut off due to the offset of the detector with respect to the IFU.

2023-06-17-1: 2MASS J12210808-5212226
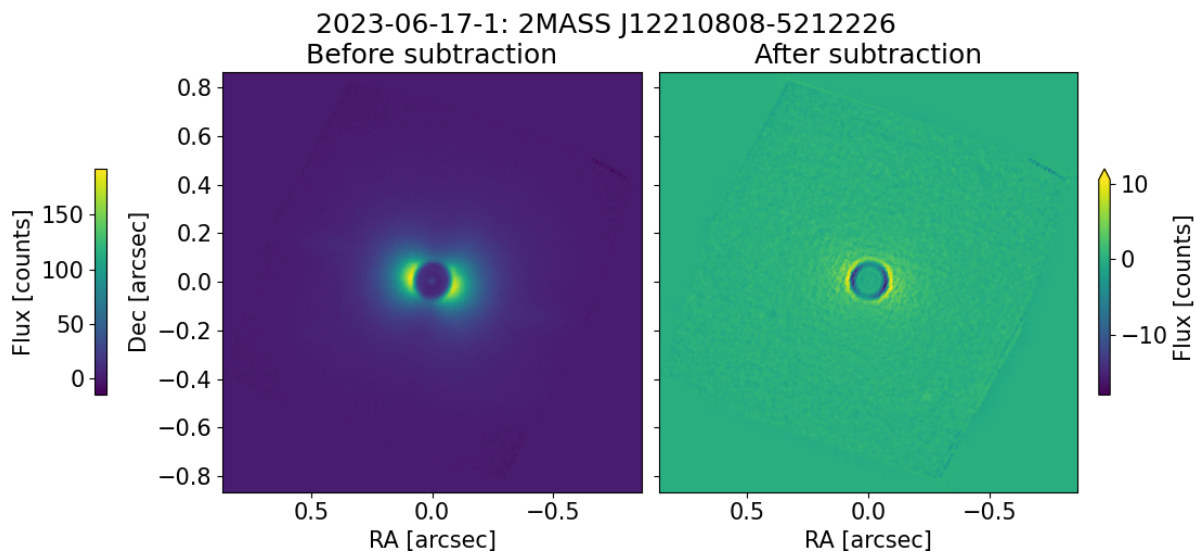
Figure A.12: Coadded cubes for the observation of 2MASS J12210808-5212226. The cubes have been derotated such that north is up and east is left. The square shape visible in the images is the shape of the detector, with part cut off due to the offset of the detector with respect to the IFU.

2023-06-17-2: 2MASS J12195938-5018404
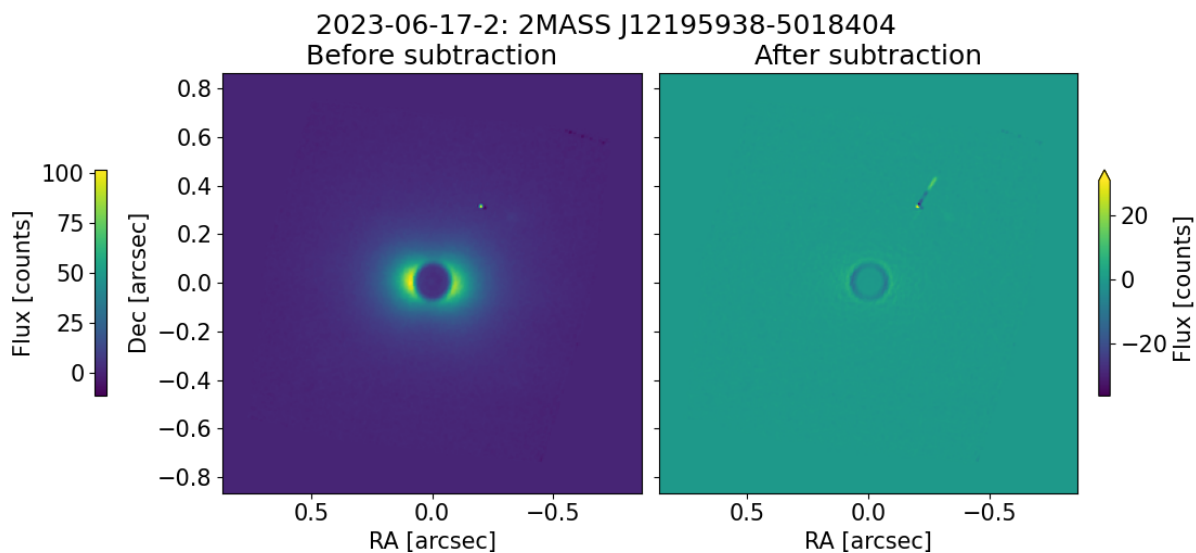
Figure A.13: Coadded cubes for the observation of 2MASS J12195938-5018404. The cubes have been derotated such that north is up and east is left. The square shape visible in the images is the shape of the detector, with part cut off due to the offset of the detector with respect to the IFU.
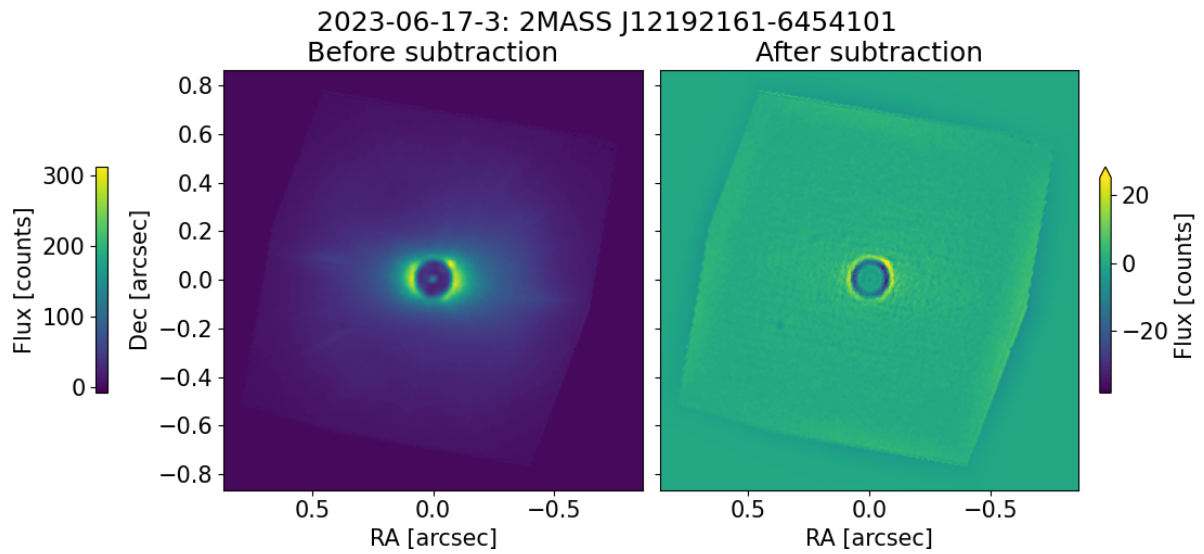
Figure A.14: Coadded cubes for the observation of 2MASS J12192161-6454101. The cubes have been derotated such that north is up and east is left. The square shape visible in the images is the shape of the detector, with part cut off due to the offset of the detector with respect to the IFU.
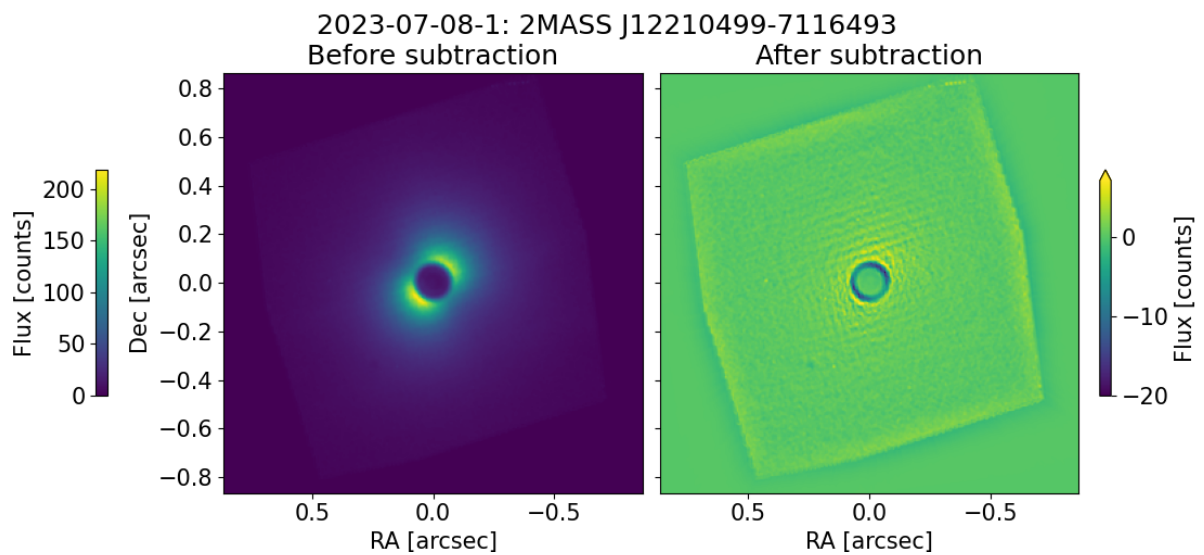
Figure A.15: Coadded cubes for the observation of 2MASS J12210499-7116493. The cubes have been derotated such that north is up and east is left. The square shape visible in the images is the shape of the detector, with part cut off due to the offset of the detector with respect to the IFU.
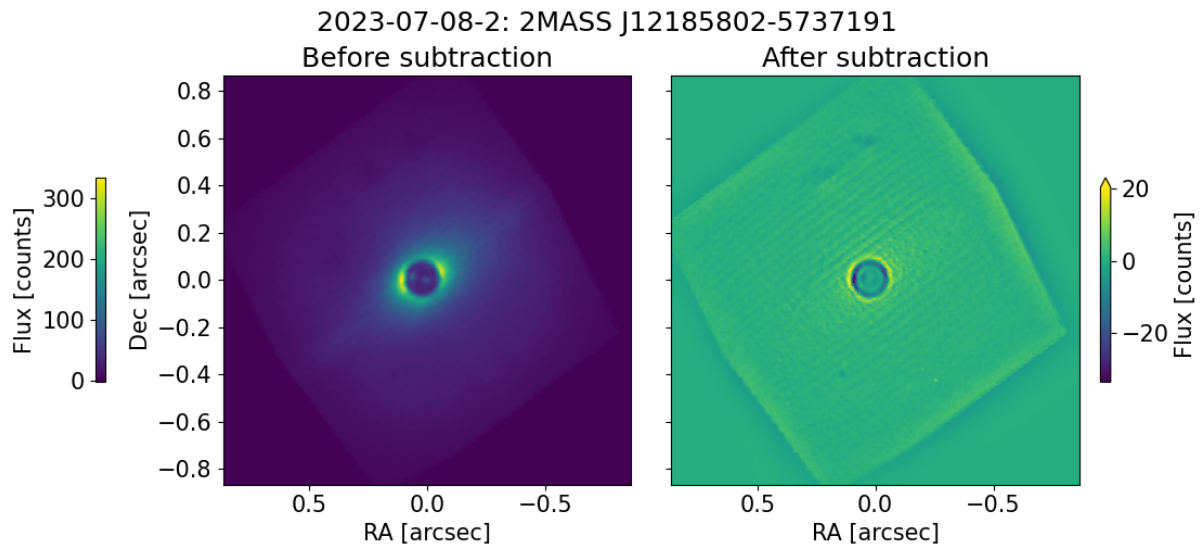
Figure A.16: Coadded cubes for the observation of 2MASS J12185802-5737191. The cubes have been derotated such that north is up and east is left. The square shape visible in the images is the shape of the detector, with part cut off due to the offset of the detector with respect to the IFU.
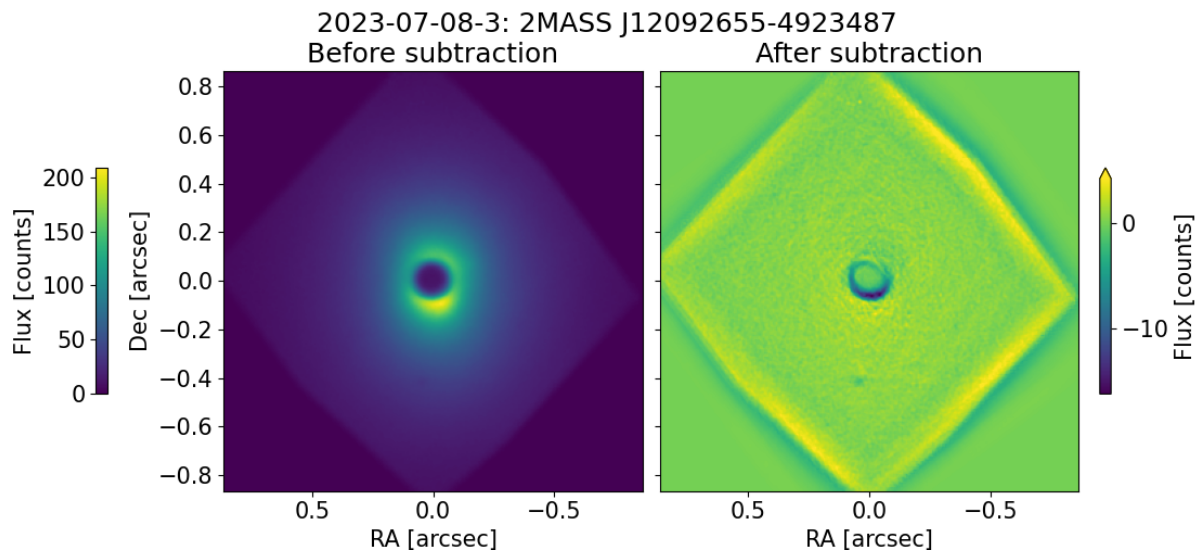
Figure A.17: Coadded cubes for the observation of 2MASS J12092655-4923487. The cubes have been derotated such that north is up and east is left. The square shape visible in the images is the shape of the detector, with part cut off due to the offset of the detector with respect to the IFU.
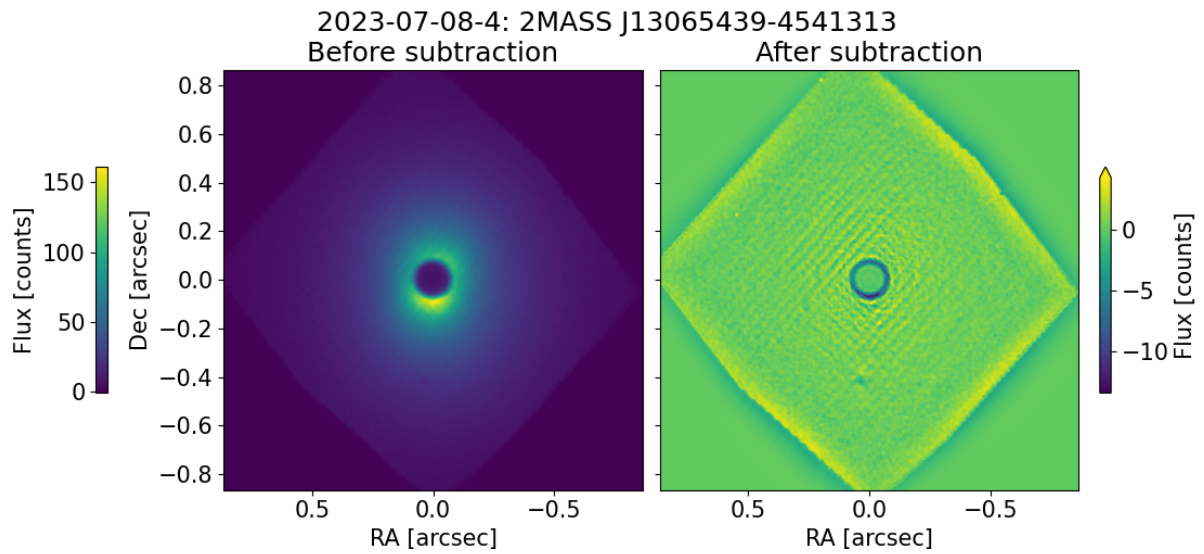
Figure A.18: Coadded cubes for the observation of 2MASS J13065439-4541313. The cubes have been derotated such that north is up and east is left. The square shape visible in the images is the shape of the detector, with part cut off due to the offset of the detector with respect to the IFU.
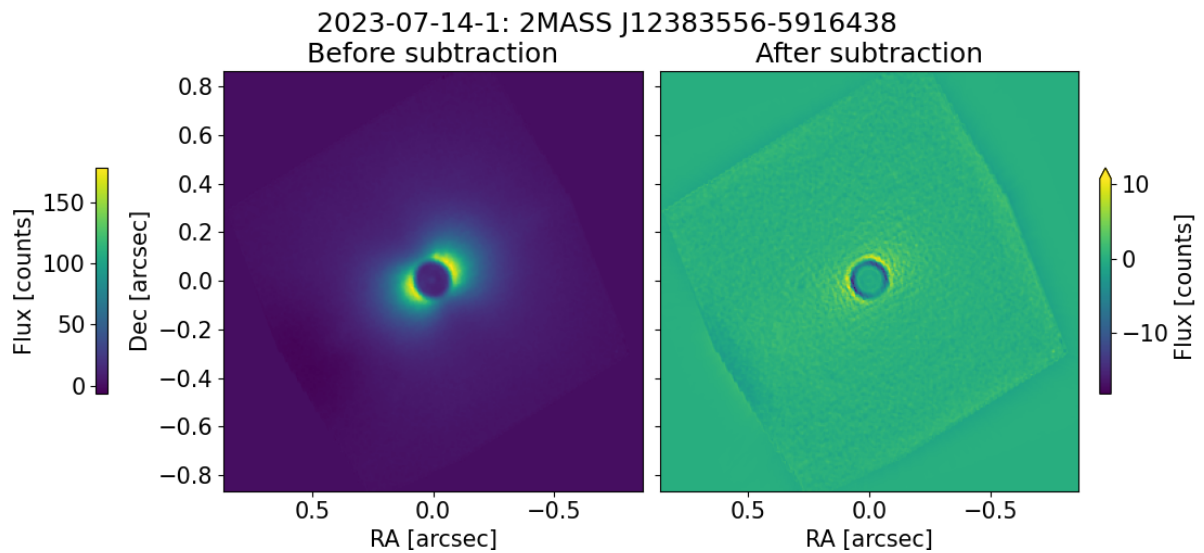
Figure A.19: Coadded cubes for the observation of 2MASS J12383556-5916438. The cubes have been derotated such that north is up and east is left. The square shape visible in the images is the shape of the detector, with part cut off due to the offset of the detector with respect to the IFU.
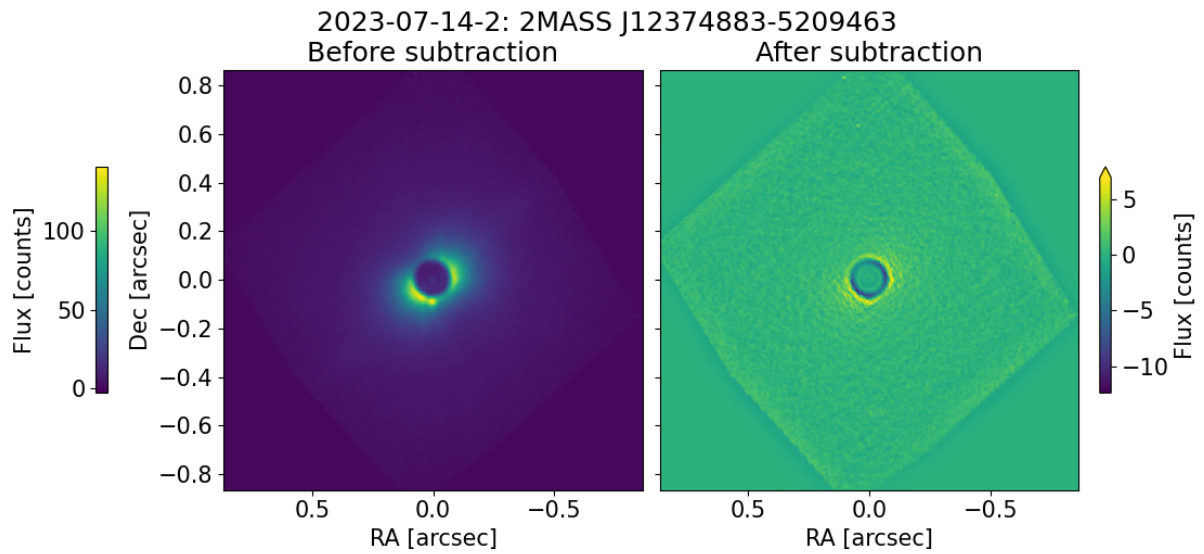
Figure A.20: Coadded cubes for the observation of 2MASS J12374883-5209463. The cubes have been derotated such that north is up and east is left. The square shape visible in the images is the shape of the detector, with part cut off due to the offset of the detector with respect to the IFU.
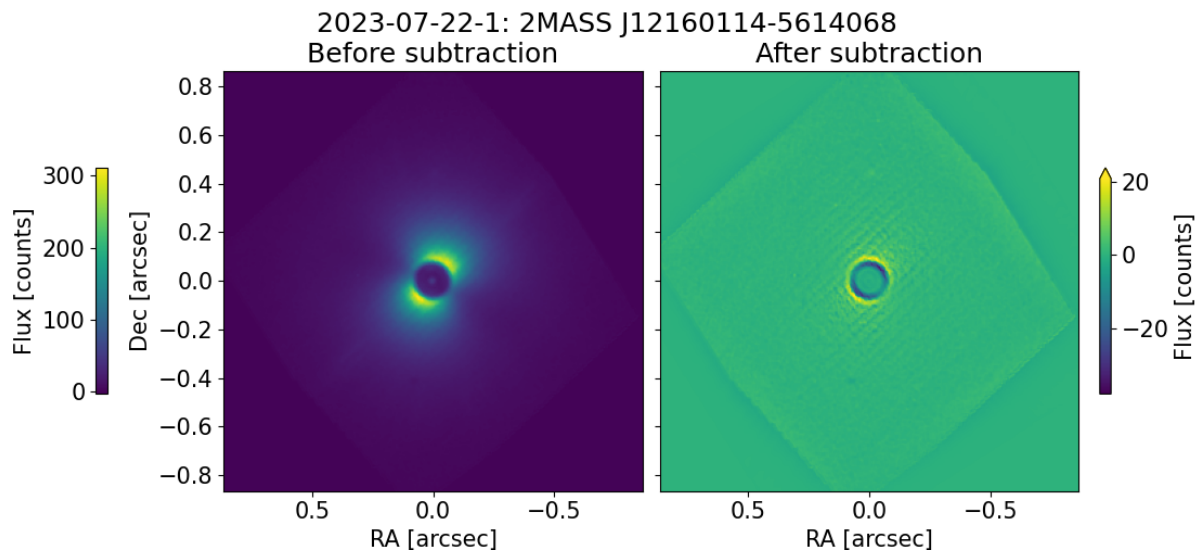
Figure A.21: Coadded cubes for the observation of 2MASS J12160114-5614068. The cubes have been derotated such that north is up and east is left. The square shape visible in the images is the shape of the detector, with part cut off due to the offset of the detector with respect to the IFU.
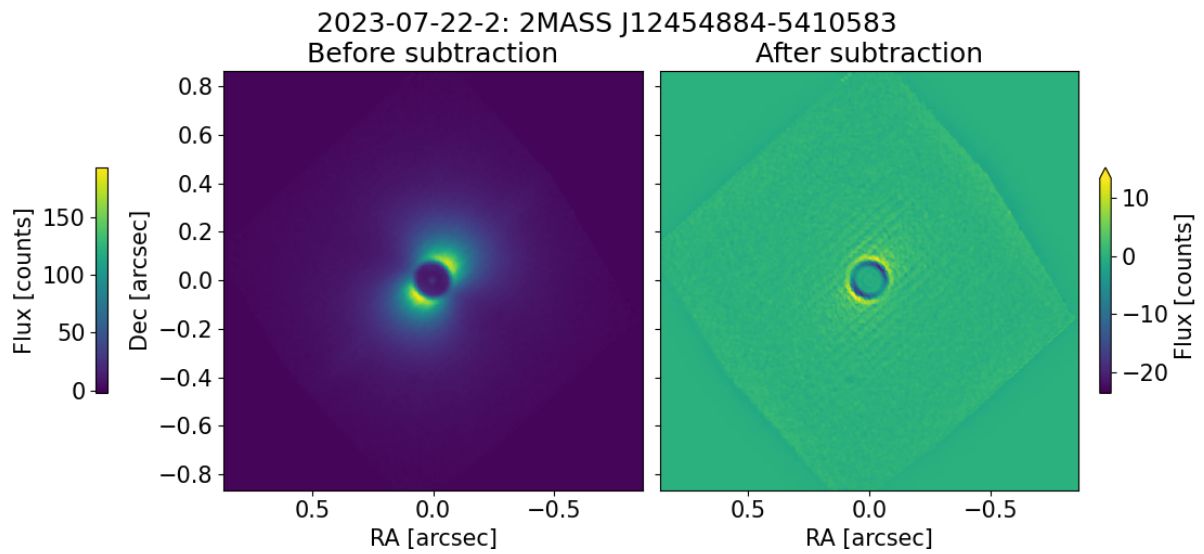
Figure A.22: Coadded cubes for the observation of 2MASS J12454884-5410583. The cubes have been derotated such that north is up and east is left. The square shape visible in the images is the shape of the detector, with part cut off due to the offset of the detector with respect to the IFU.
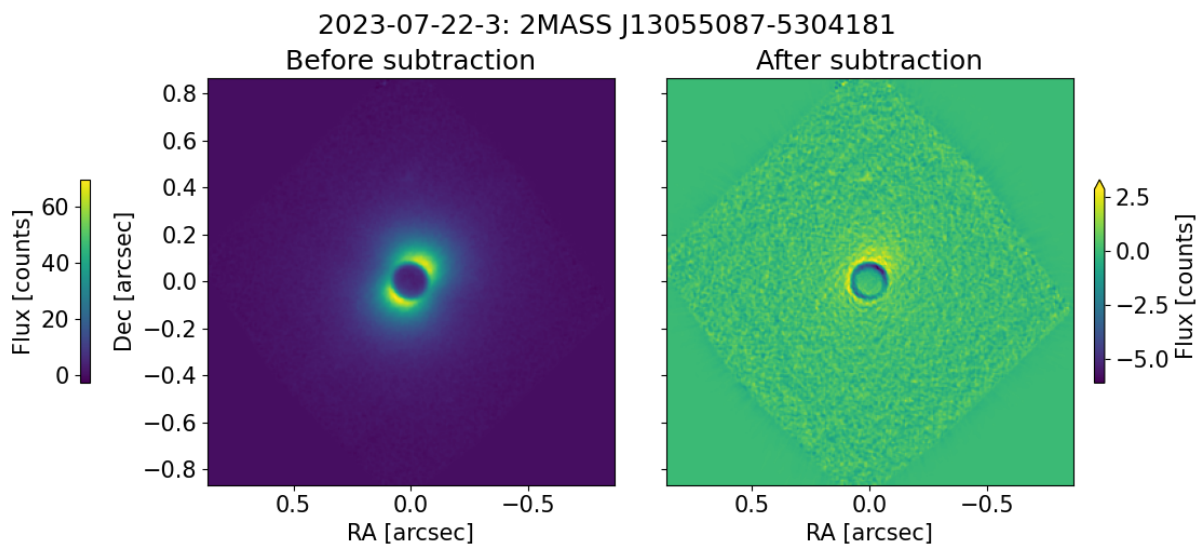
Figure A.23: Coadded cubes for the observation of 2MASS J13055087-5304181. The cubes have been derotated such that north is up and east is left. The square shape visible in the images is the shape of the detector, with part cut off due to the offset of the detector with respect to the IFU.
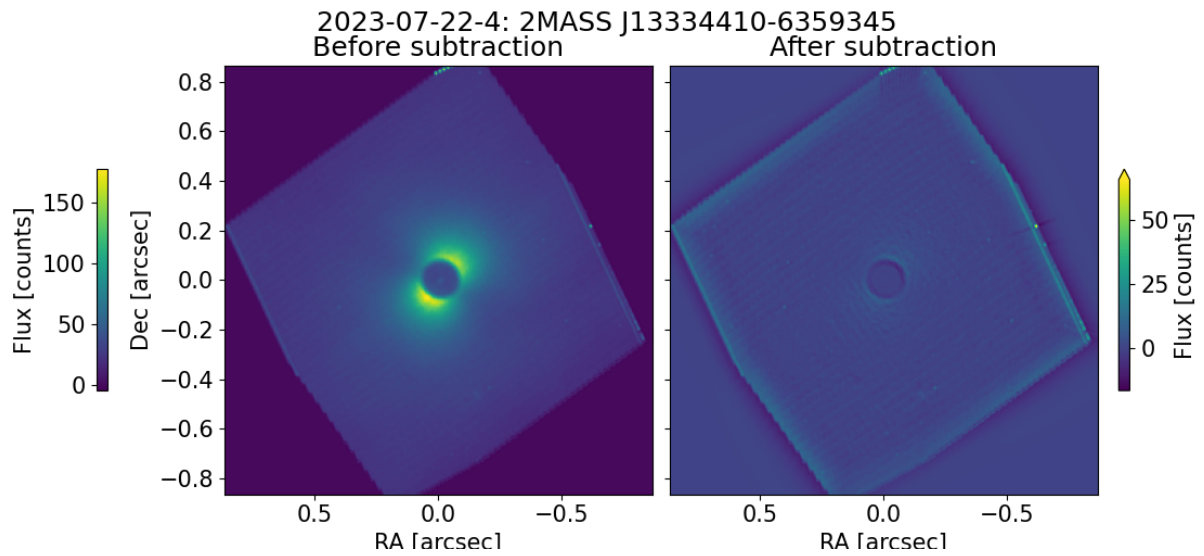
Figure A.24: Coadded cubes for the observation of 2MASS J13334410-6359345. The cubes have been derotated such that north is up and east is left. The square shape visible in the images is the shape of the detector, with part cut off due to the offset of the detector with respect to the IFU.
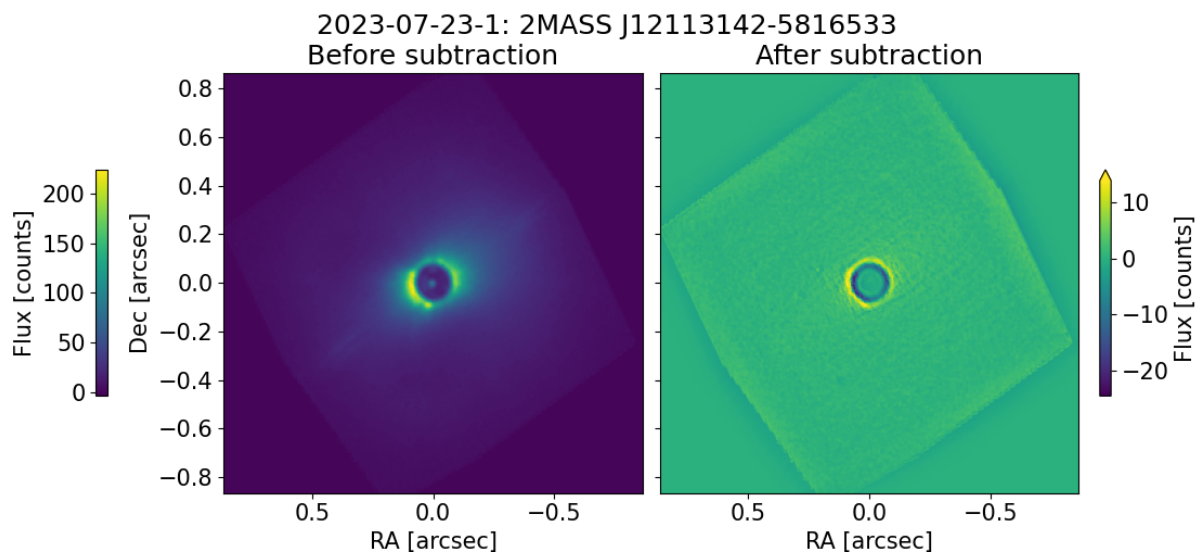
Figure A.25: Coadded cubes for the observation of 2MASS J12113142-5816533. The cubes have been derotated such that north is up and east is left. The square shape visible in the images is the shape of the detector, with part cut off due to the offset of the detector with respect to the IFU.
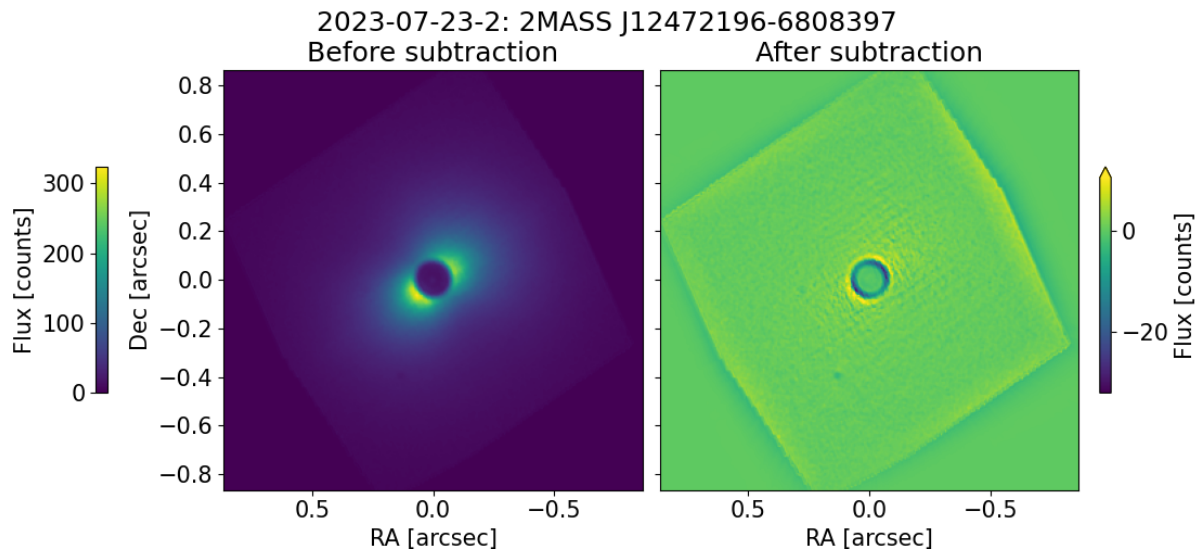
Figure A.26: Coadded cubes for the observation of 2MASS J12472196-6808397. The cubes have been derotated such that north is up and east is left. The square shape visible in the images is the shape of the detector, with part cut off due to the offset of the detector with respect to the IFU.
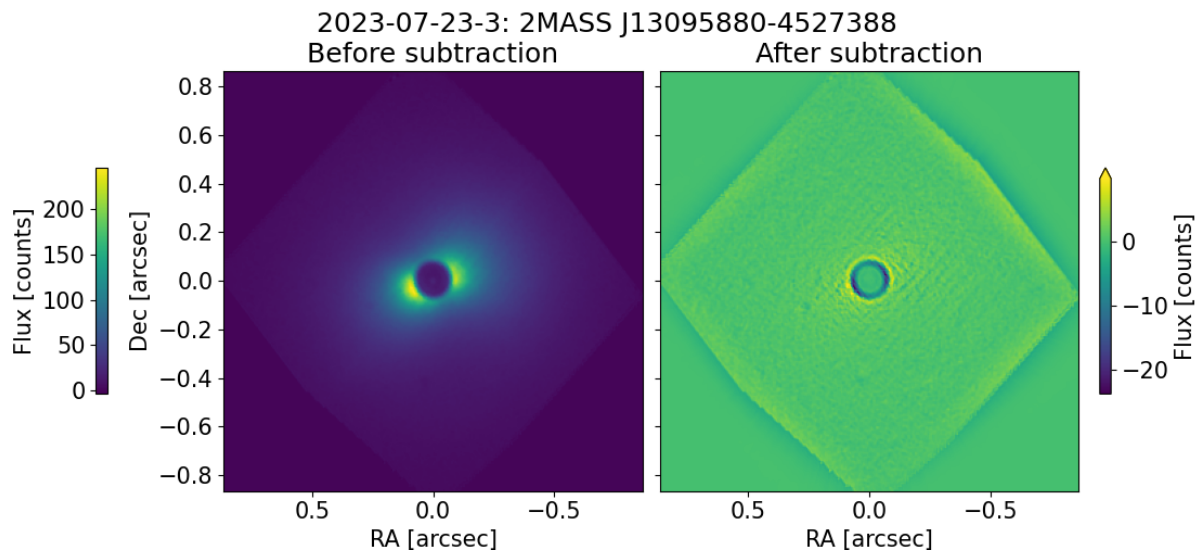
Figure A.27: Coadded cubes for the observation of 2MASS J13095880-4527388. The cubes have been derotated such that north is up and east is left. The square shape visible in the images is the shape of the detector, with part cut off due to the offset of the detector with respect to the IFU.
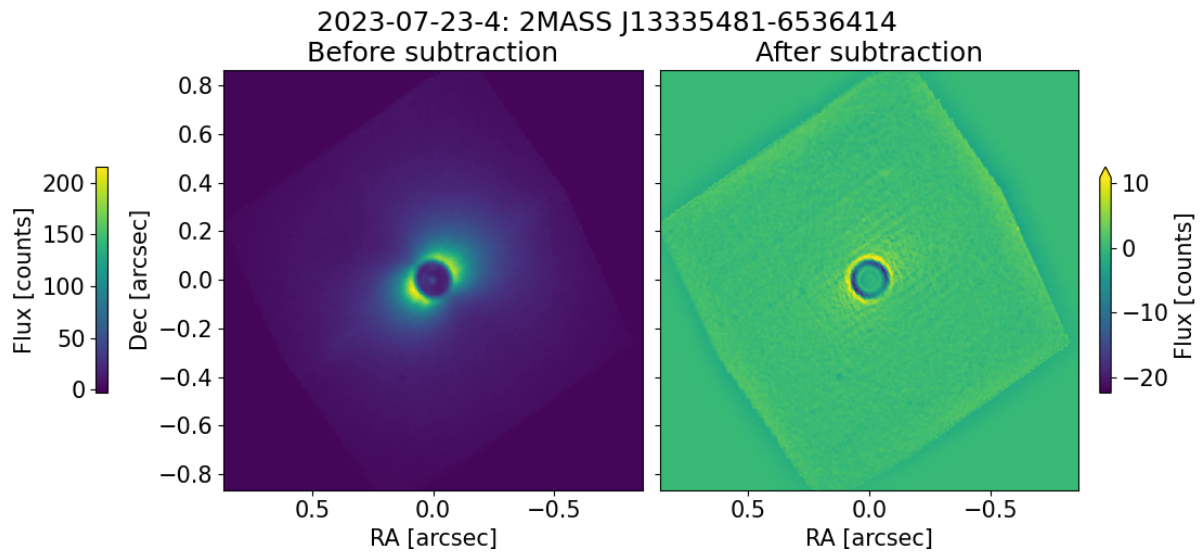
Figure A.28: Coadded cubes for the observation of 2MASS J13335481-6536414. The cubes have been derotated such that north is up and east is left. The square shape visible in the images is the shape of the detector, with part cut off due to the offset of the detector with respect to the IFU.
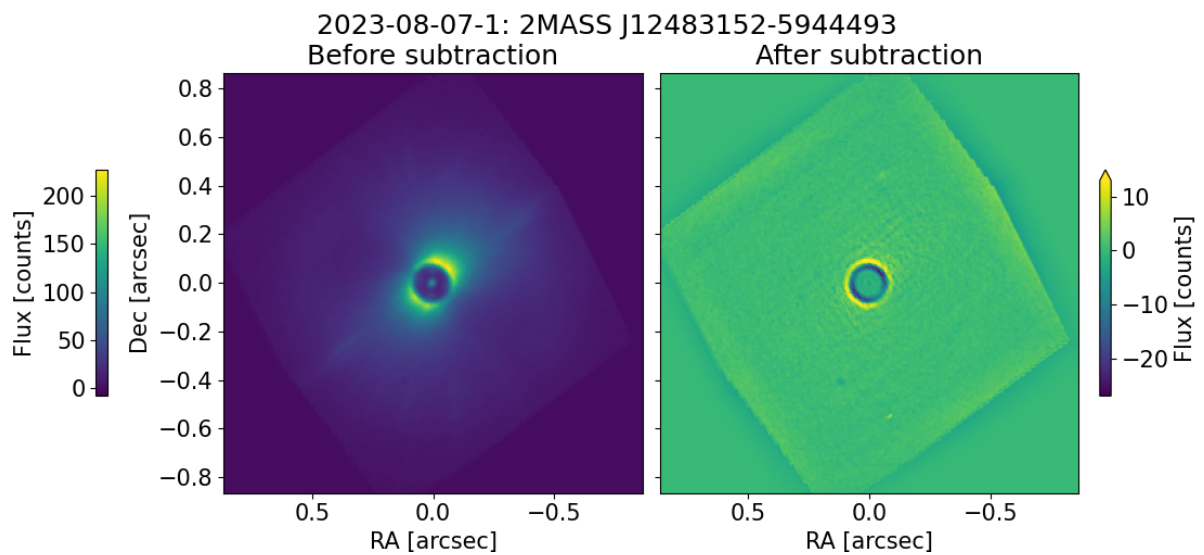
Figure A.29: Coadded cubes for the observation of 2MASS J12483152-5944493. The cubes have been derotated such that north is up and east is left. The square shape visible in the images is the shape of the detector, with part cut off due to the offset of the detector with respect to the IFU.
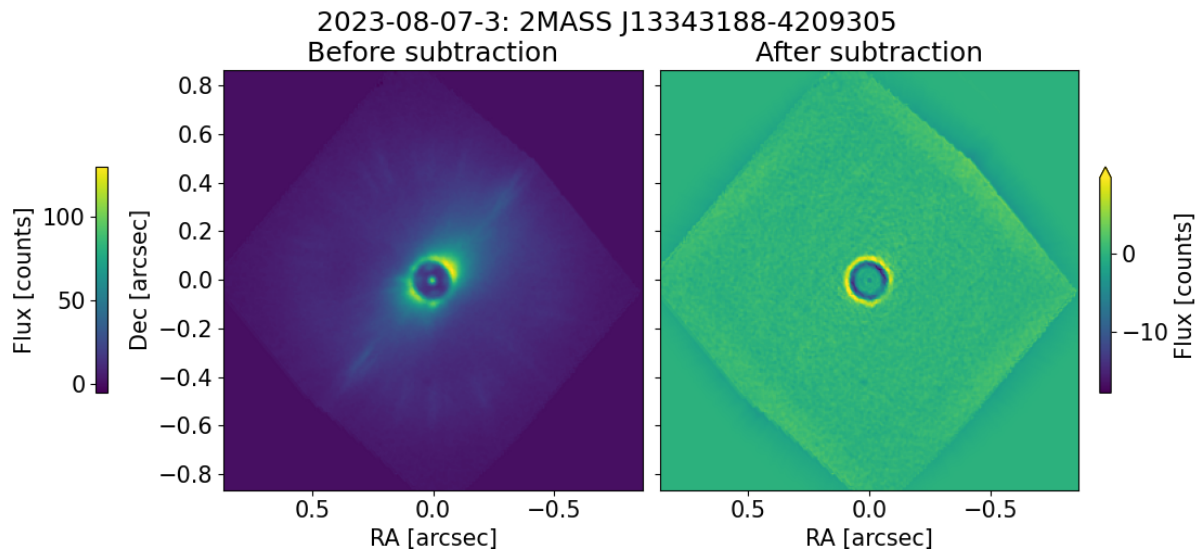
Figure A.30: Coadded cubes for the observation of 2MASS J13343188-4209305. The cubes have been derotated such that north is up and east is left. The square shape visible in the images is the shape of the detector, with part cut off due to the offset of the detector with respect to the IFU.
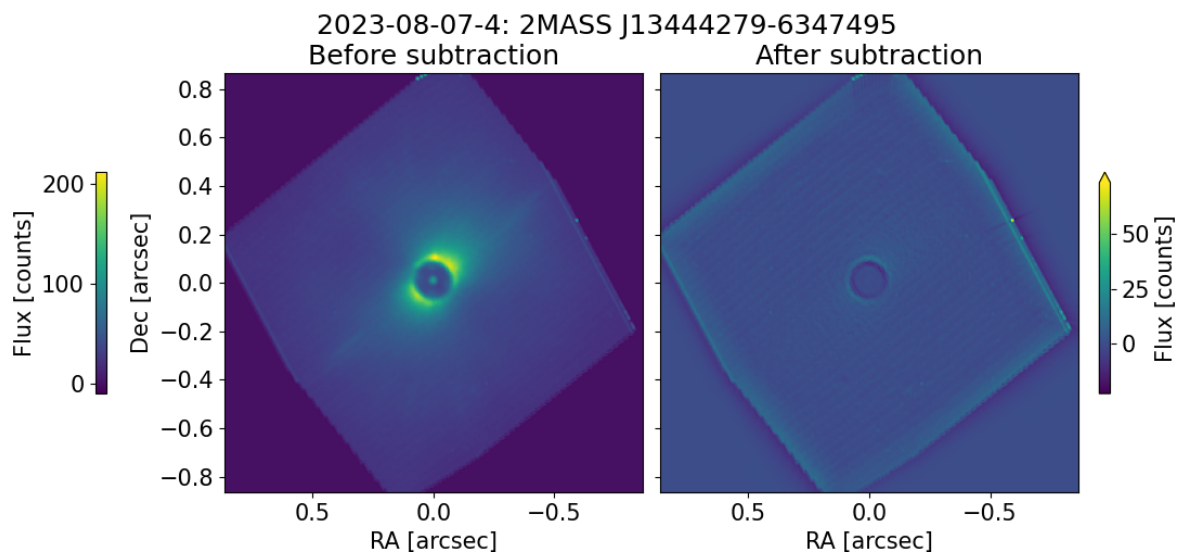
Figure A.31: Coadded cubes for the observation of 2MASS J13444279-6347495. The cubes have been derotated such that north is up and east is left. The square shape visible in the images is the shape of the detector, with part cut off due to the offset of the detector with respect to the IFU.
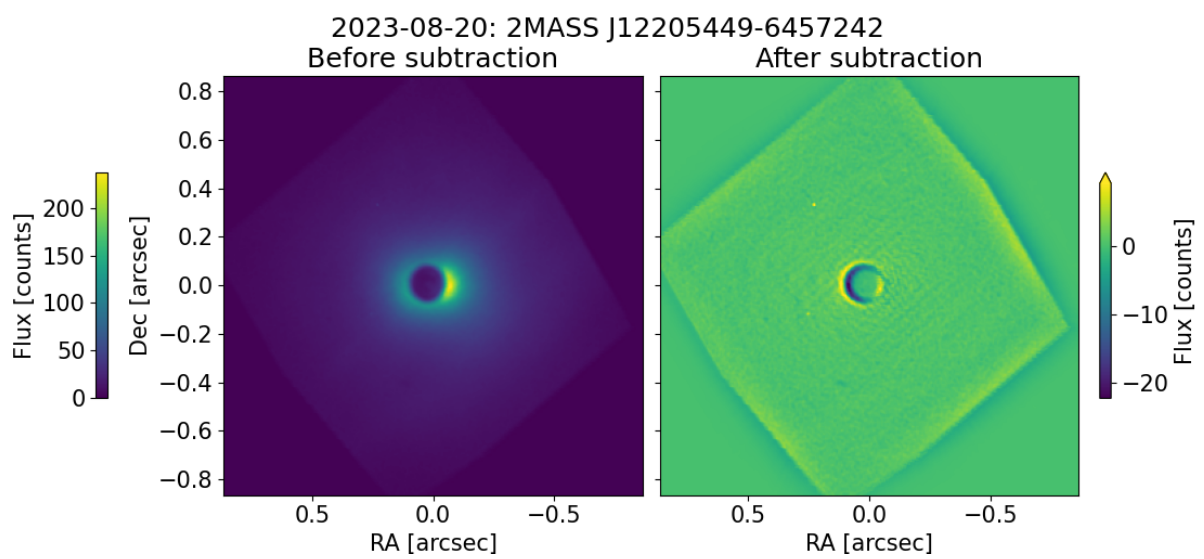
Figure A.32: Coadded cubes for the observation of 2MASS J12205449-6457242. The cubes have been derotated such that north is up and east is left. The square shape visible in the images is the shape of the detector, with part cut off due to the offset of the detector with respect to the IFU.

B

Individual Detection Limits

Here the detection limits are shown for all systems where companions were not detected. For targets that were observed more than once (see Table 8.1) only the contrast curve computed from the latest observation is shown.
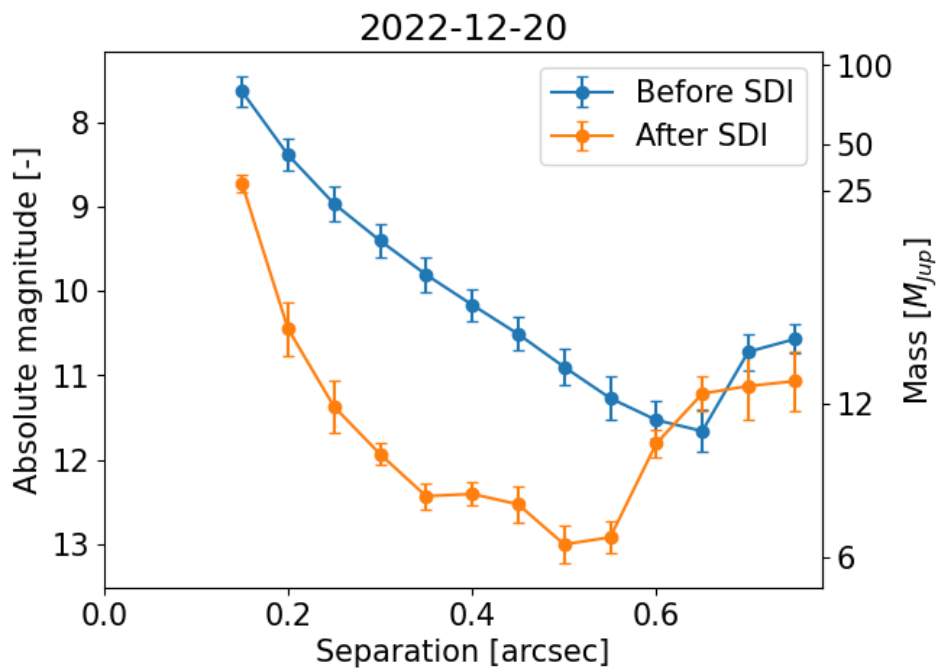
Figure B.1: Contrast curve for the observation of 2MASS J12505143-5156353.
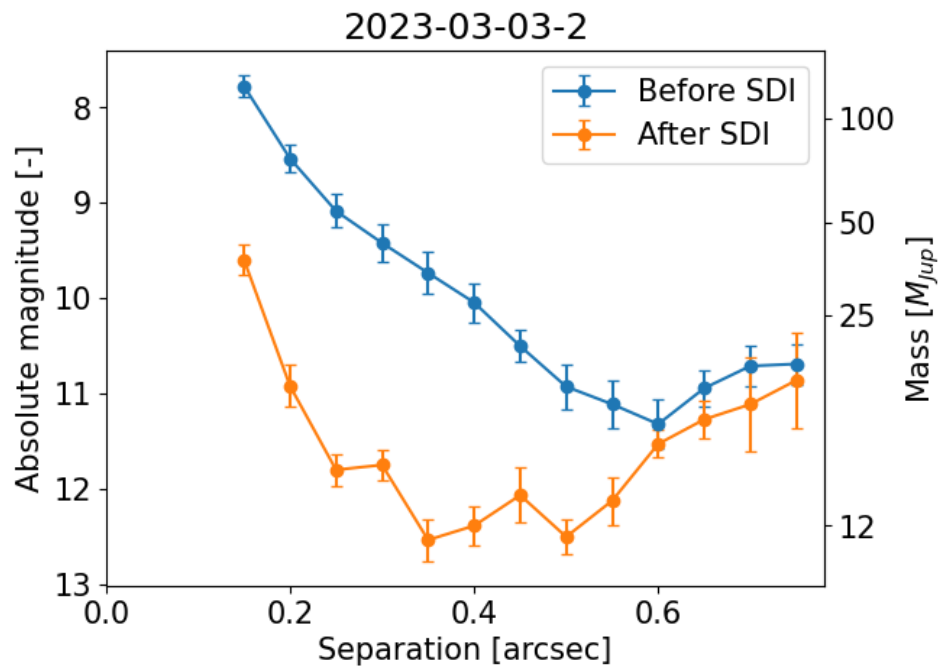
Figure B.2: Contrast curve for the observation of 2MASS J10065573-6352086.
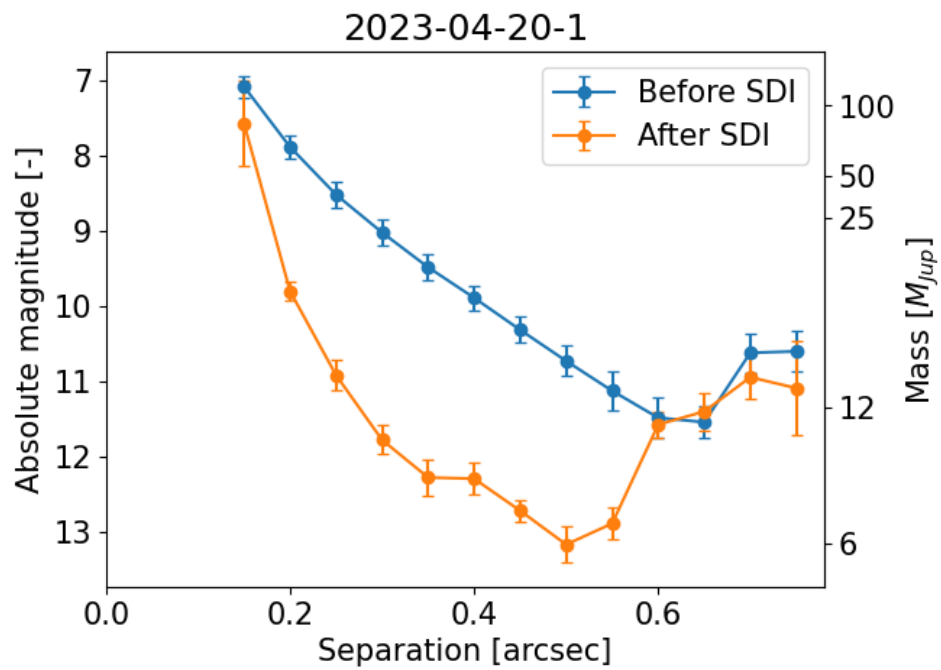
Figure B.3: Contrast curve for the observation of 2MASS J11445217-6438548.
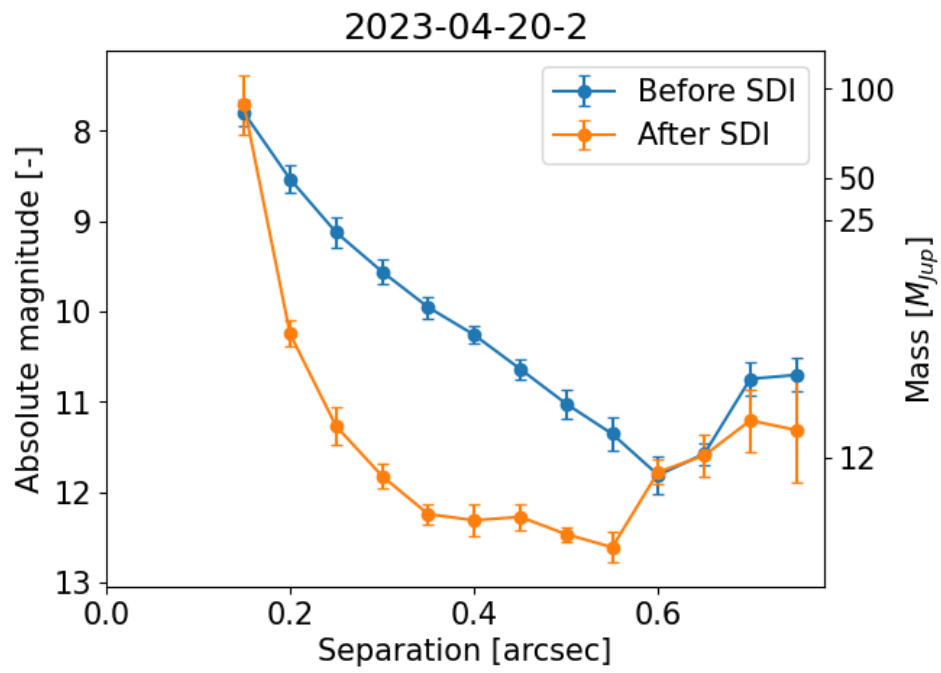
Figure B.4: Contrast curve for the observation of 2MASS J11454278-5739285.
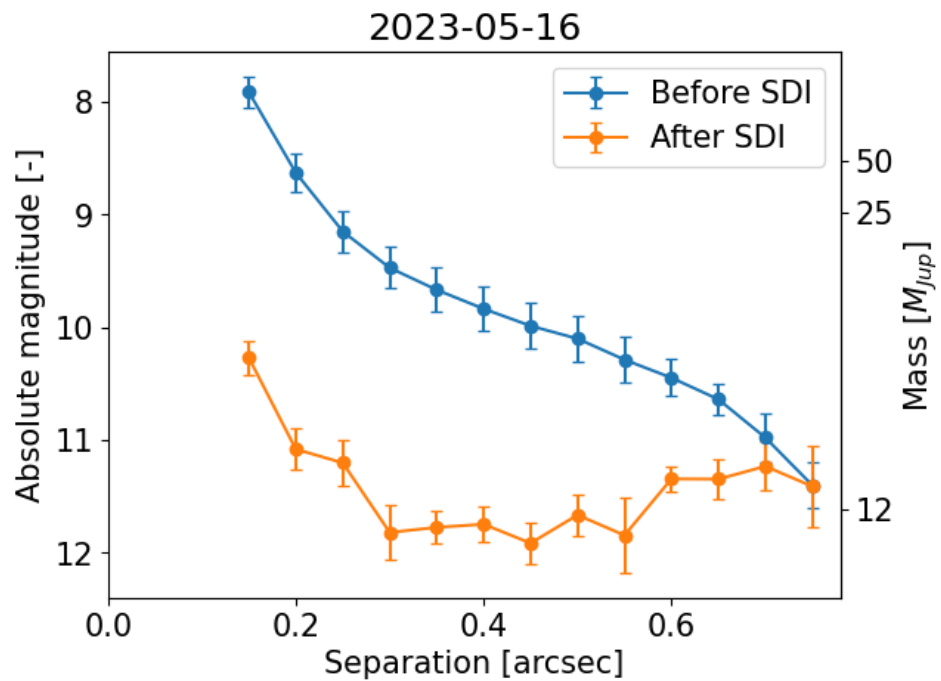
Figure B.5: Contrast curve for the observation of 2MASS J13015069-5304581.
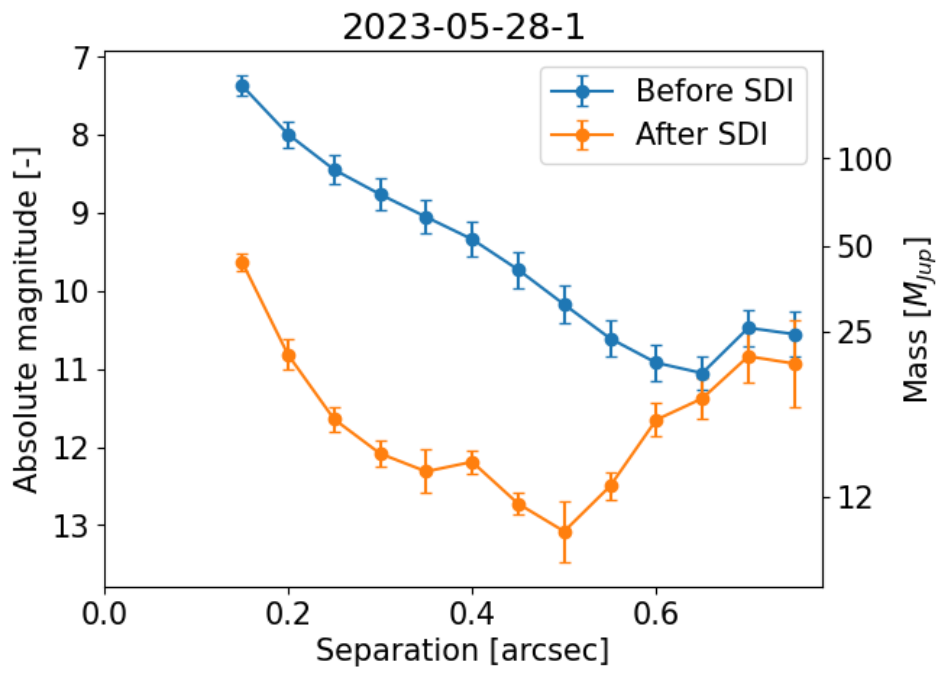
Figure B.6: Contrast curve for the observation of 2MASS J12333381-5714066.
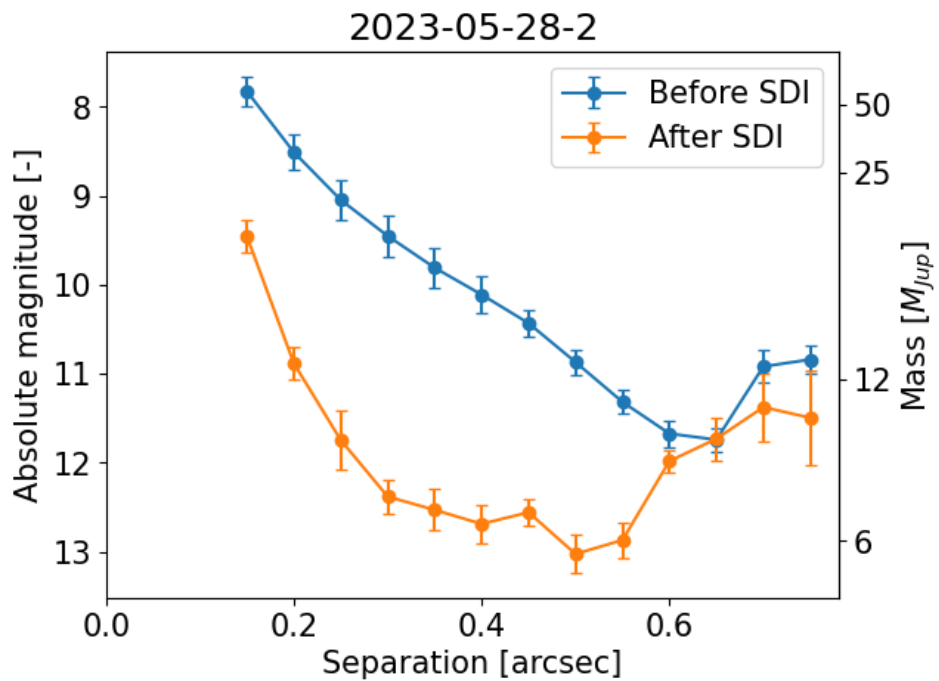
Figure B.7: Contrast curve for the observation of 2MASS J12264842-5215070.
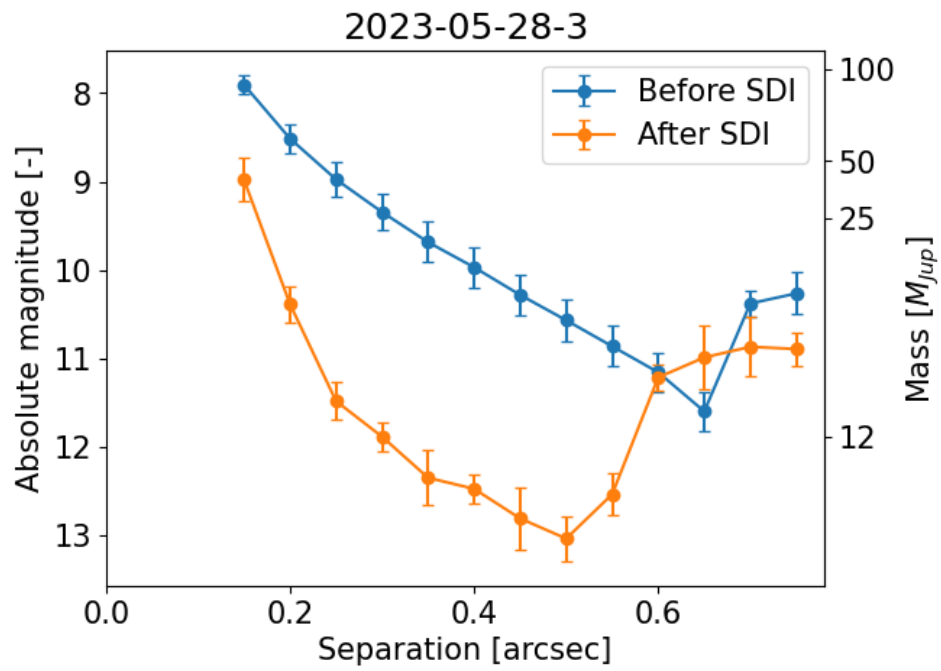
Figure B.8: Contrast curve for the observation of 2MASS J12240975-6003416.
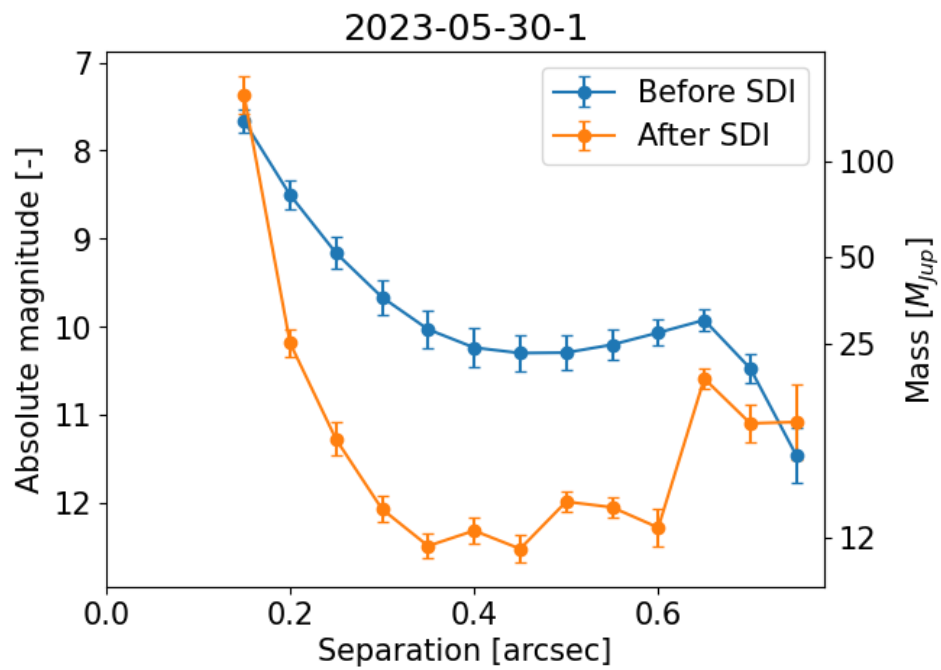
Figure B.9: Contrast curve for the observation of 2MASS J12405458-5031550.
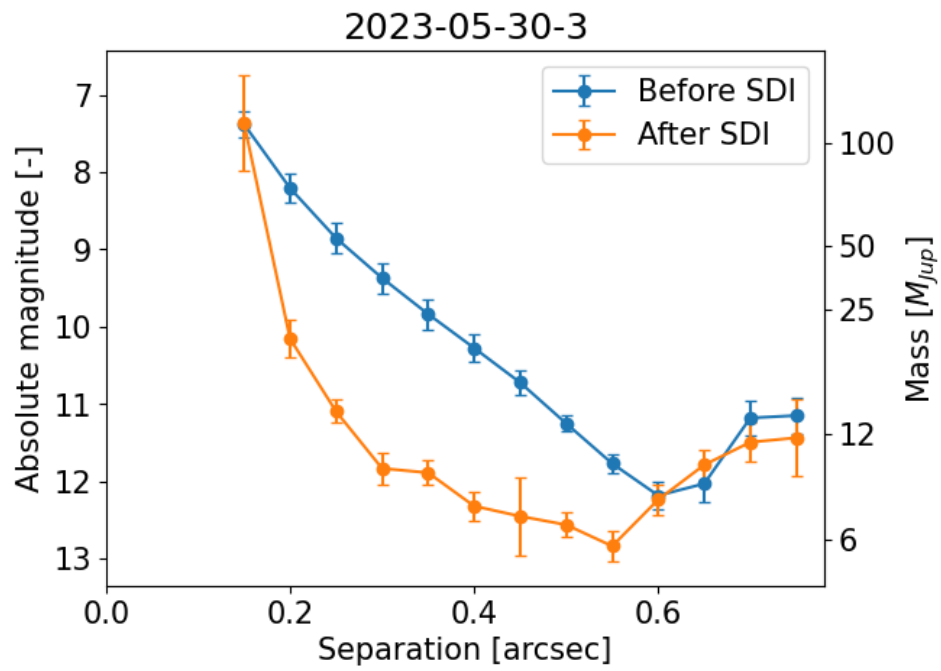
Figure B.10: Contrast curve for the observation of 2MASS J12391404-5454469.
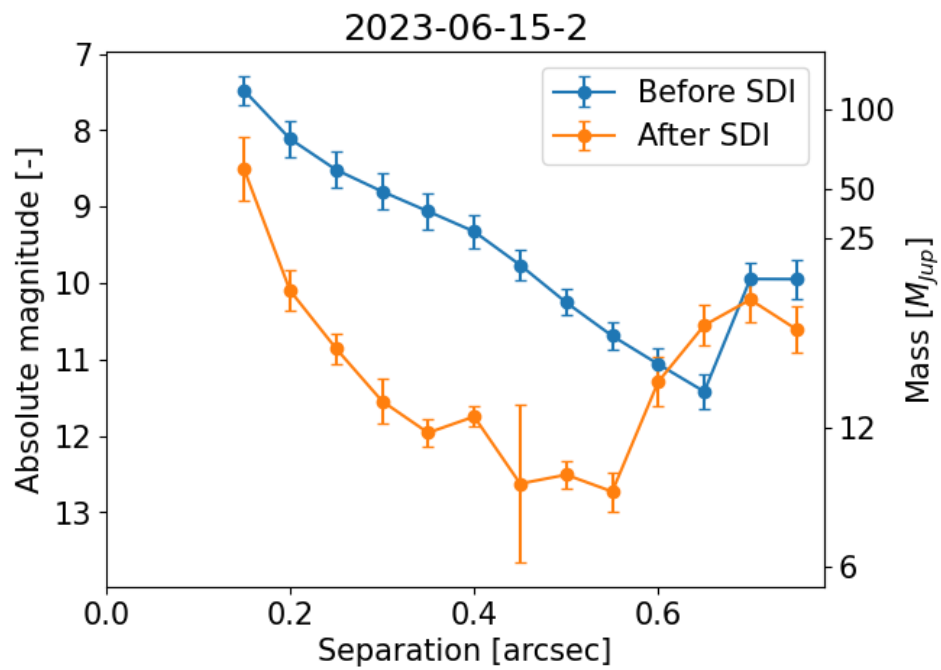
Figure B.11: Contrast curve for the observation of 2MASS J13064012-5159386.
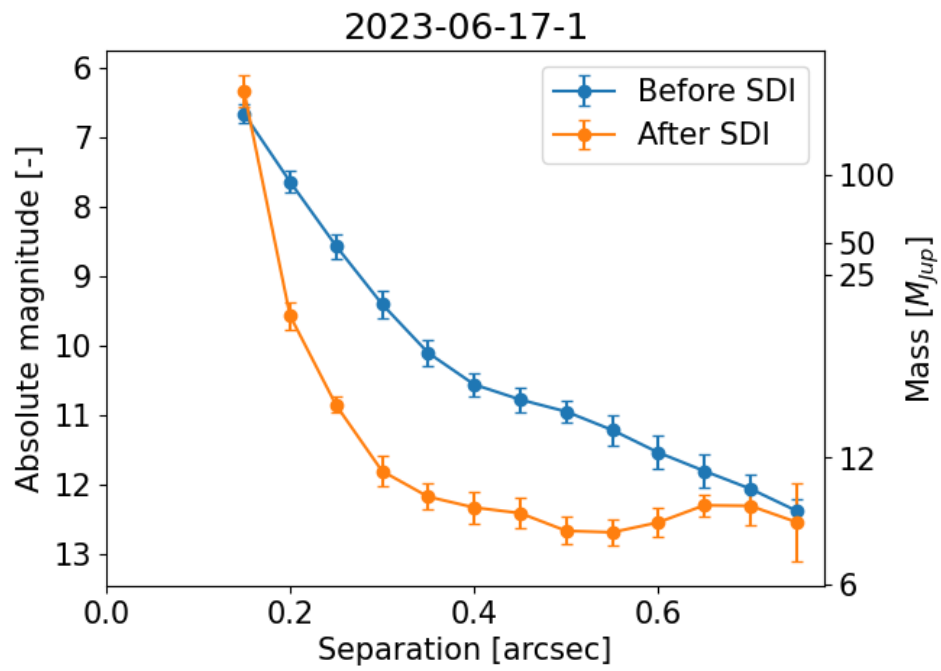
Figure B.12: Contrast curve for the observation of 2MASS J12210808-5212226.
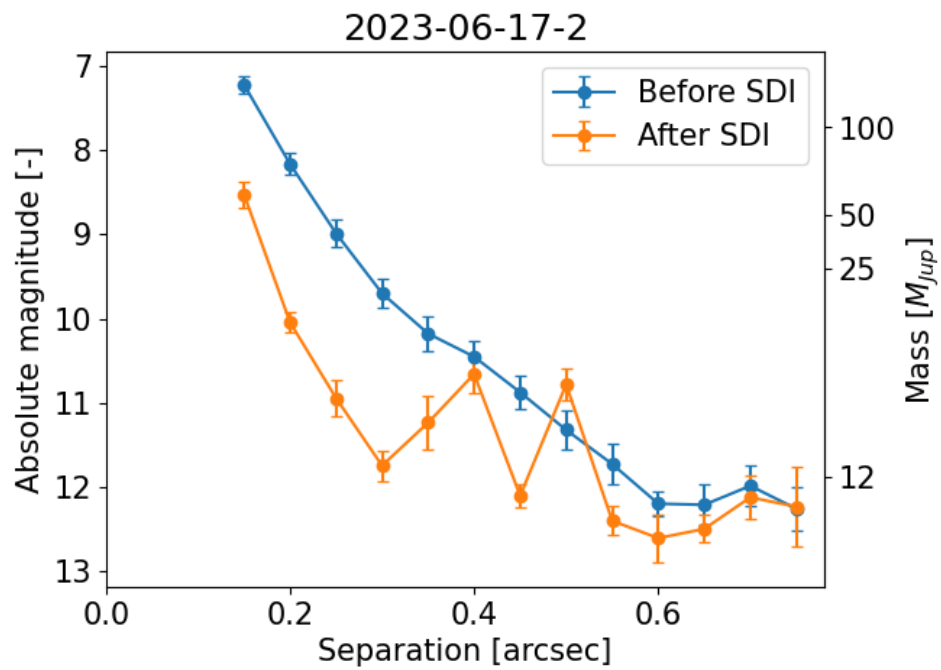
Figure B.13: Contrast curve for the observation of 2MASS J12195938-5018404.
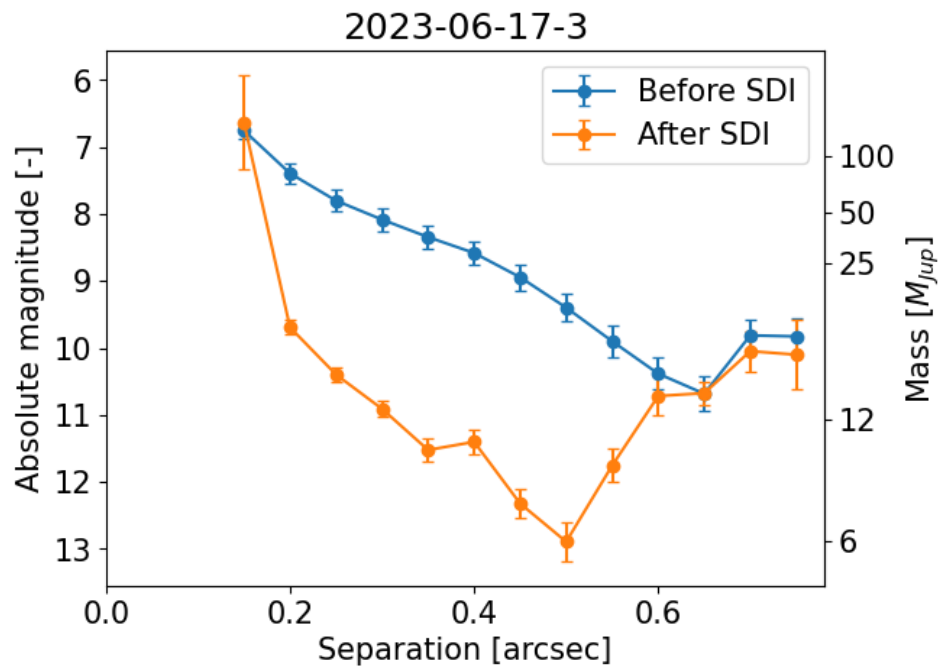
Figure B.14: Contrast curve for the observation of 2MASS J12192161-6454101.
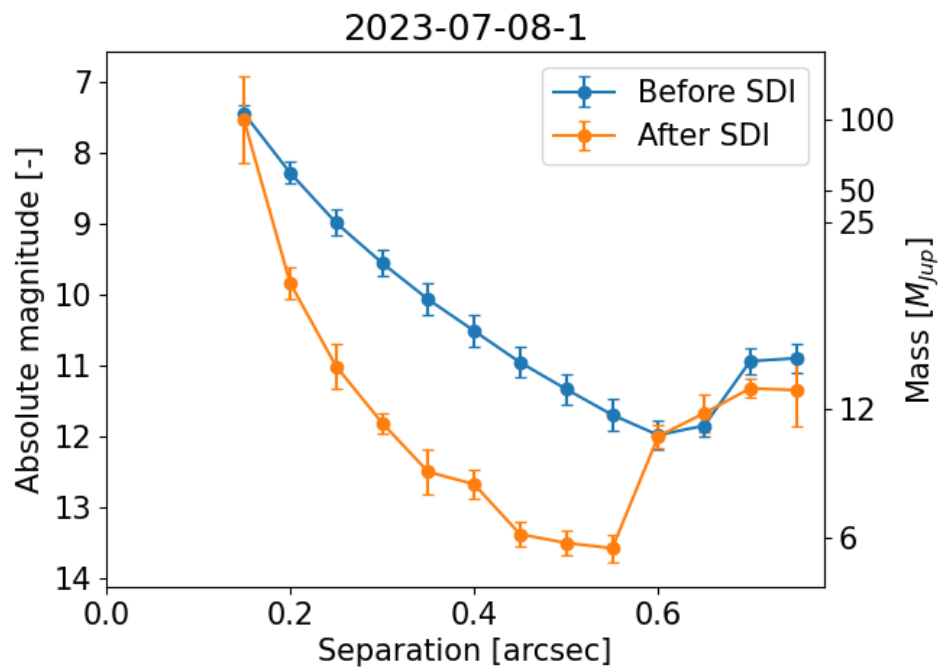
Figure B.15: Contrast curve for the observation of 2MASS J12210499-7116493.
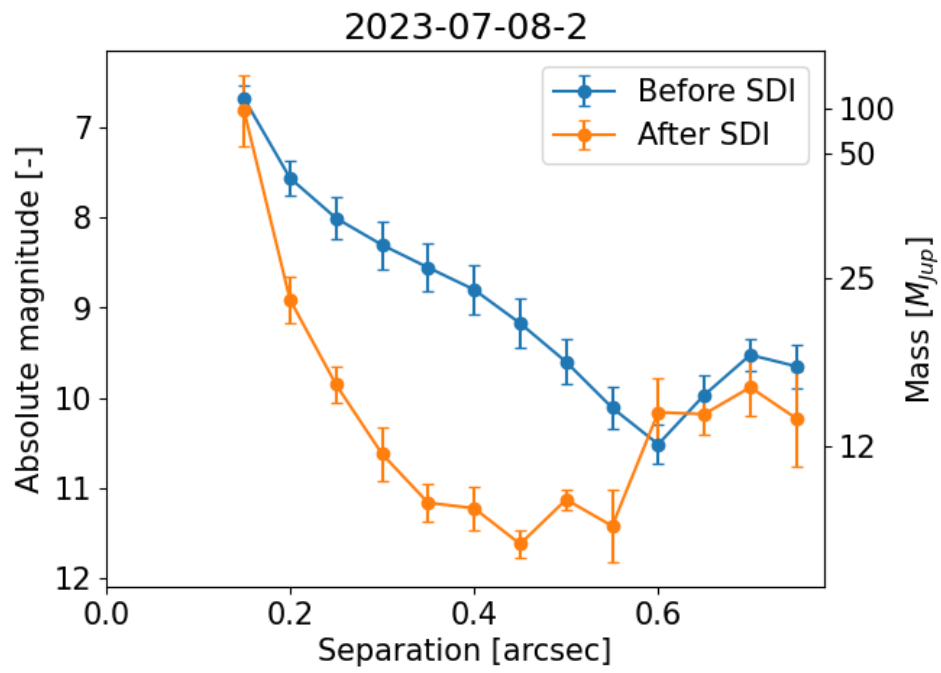
Figure B.16: Contrast curve for the observation of 2MASS J12185802-5737191.
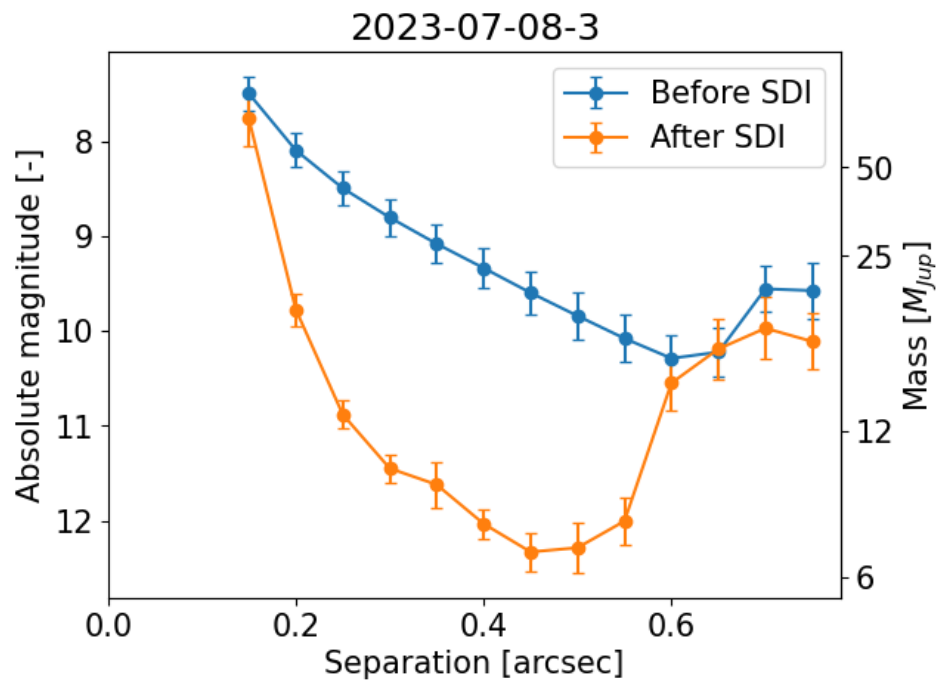
Figure B.17: Contrast curve for the observation of 2MASS J12092655-4923487.
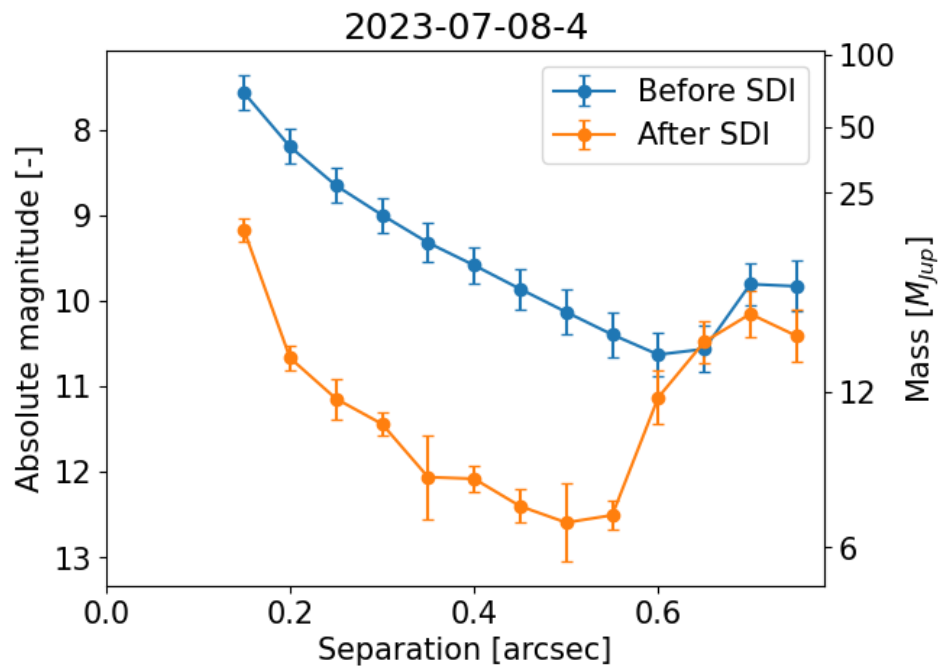
Figure B.18: Contrast curve for the observation of 2MASS J13065439-4541313.
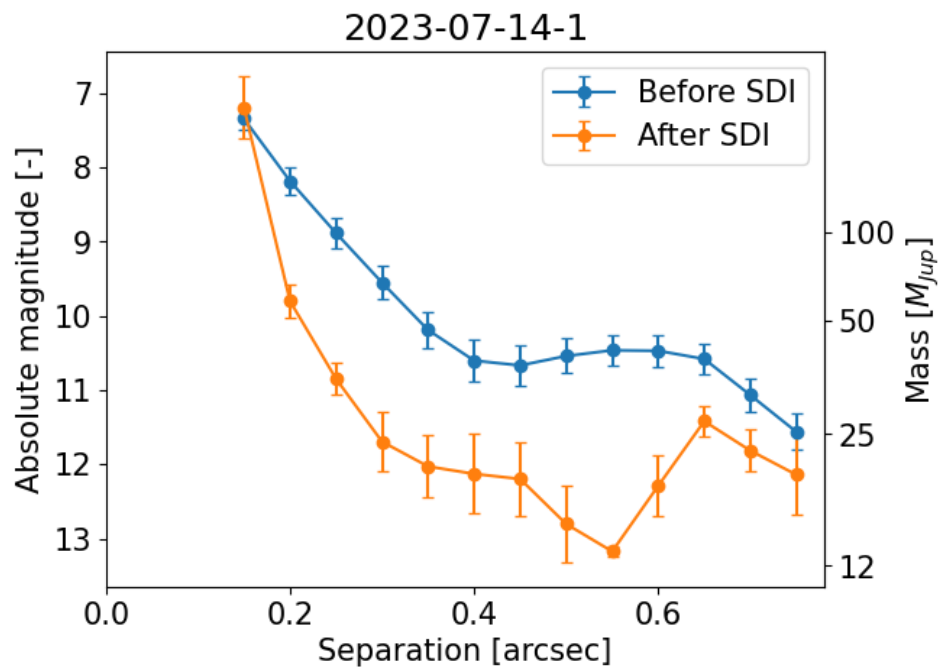
Figure B.19: Contrast curve for the observation of 2MASS J12383556-5916438.
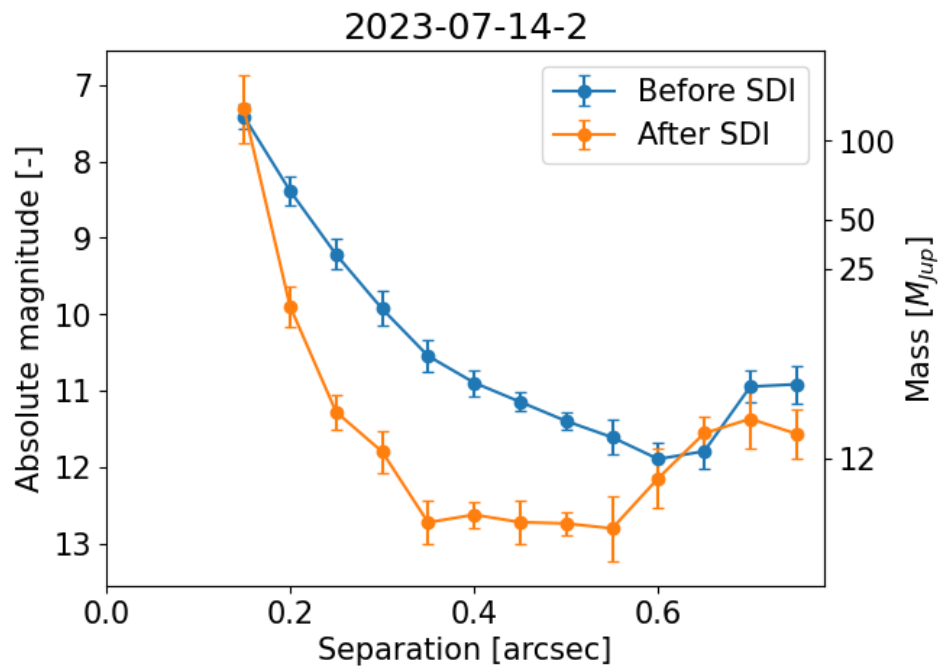
Figure B.20: Contrast curve for the observation of 2MASS J12374883-5209463.
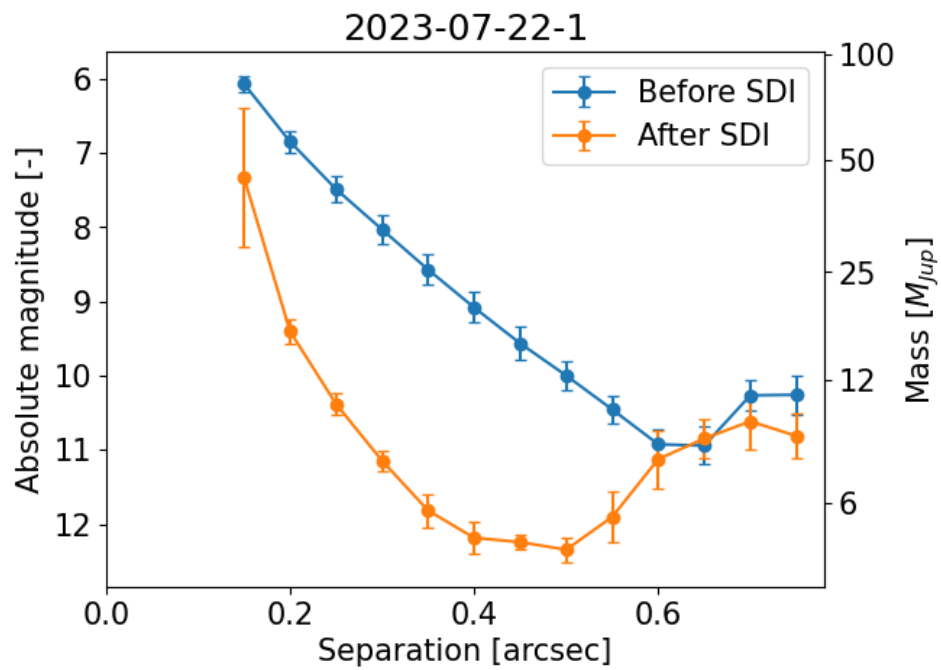
Figure B.21: Contrast curve for the observation of 2MASS J12160114-5614068.
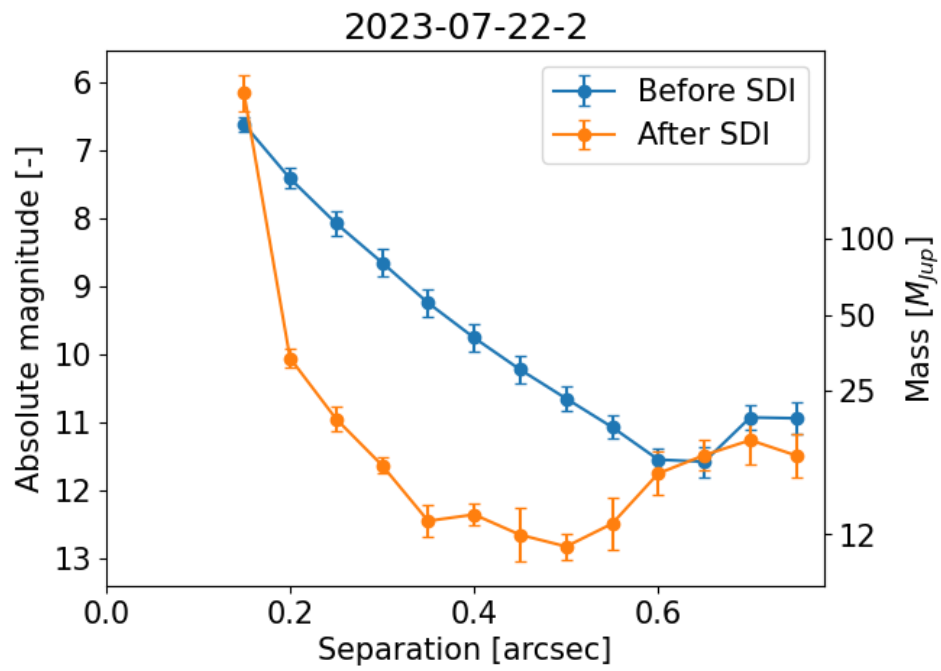
Figure B.22: Contrast curve for the observation of 2MASS J12454884-5410583.
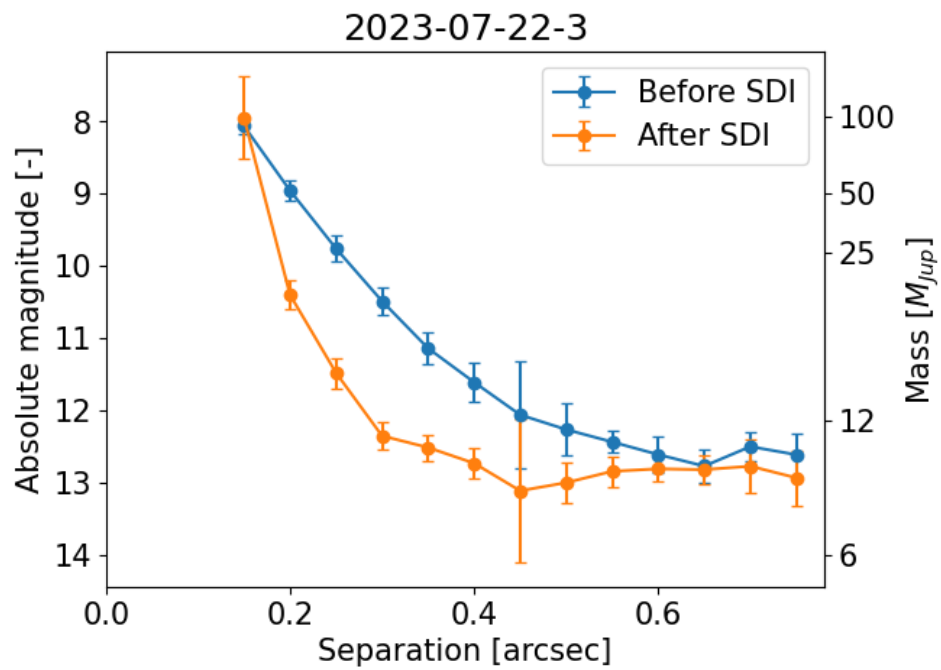
Figure B.23: Contrast curve for the observation of 2MASS J13055087-5304181.
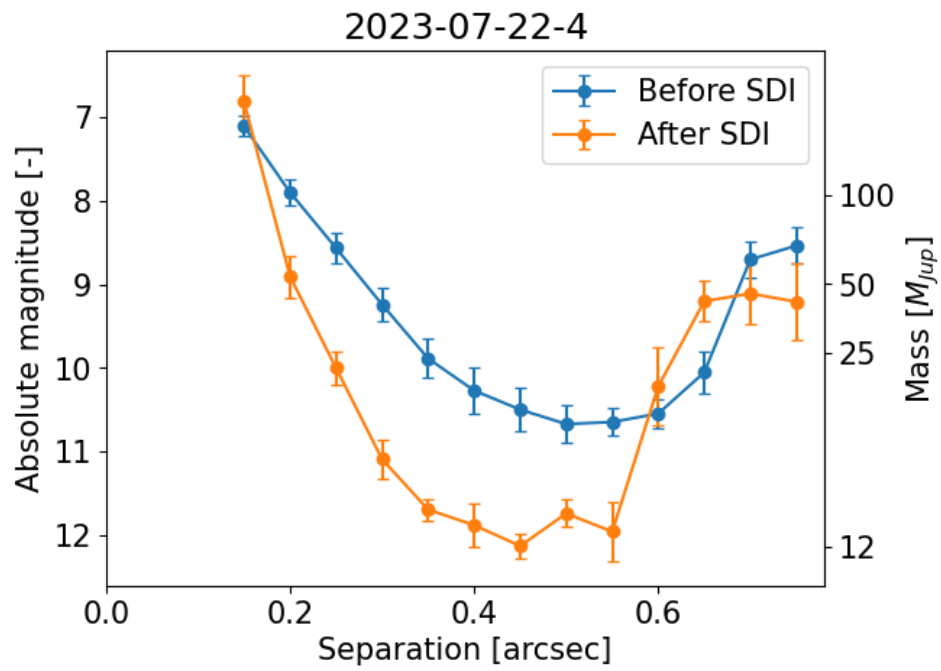
Figure B.24: Contrast curve for the observation of 2MASS J13334410-6359345.
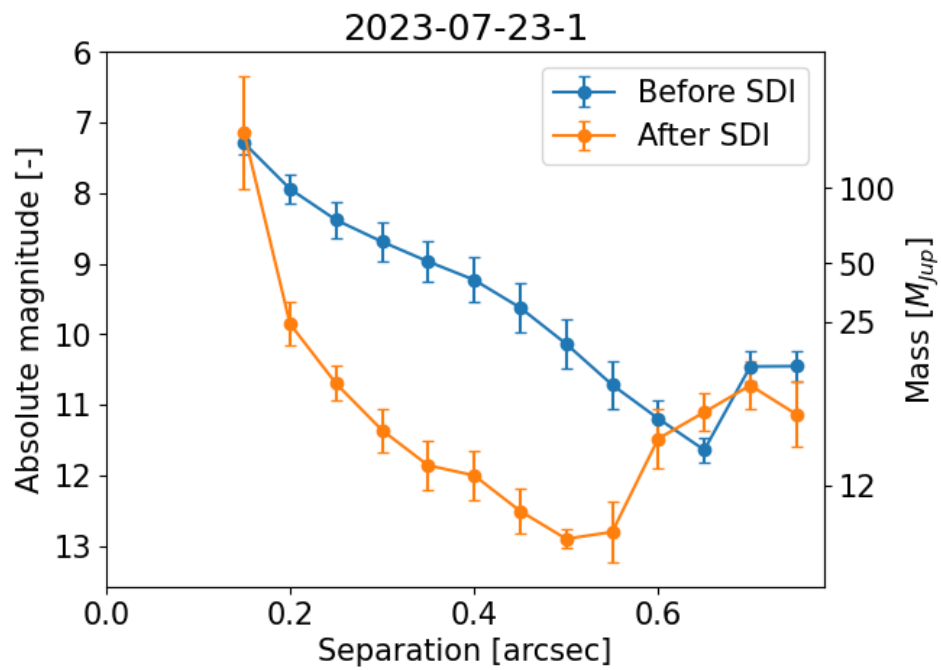
Figure B.25: Contrast curve for the observation of 2MASS J12113142-5816533.
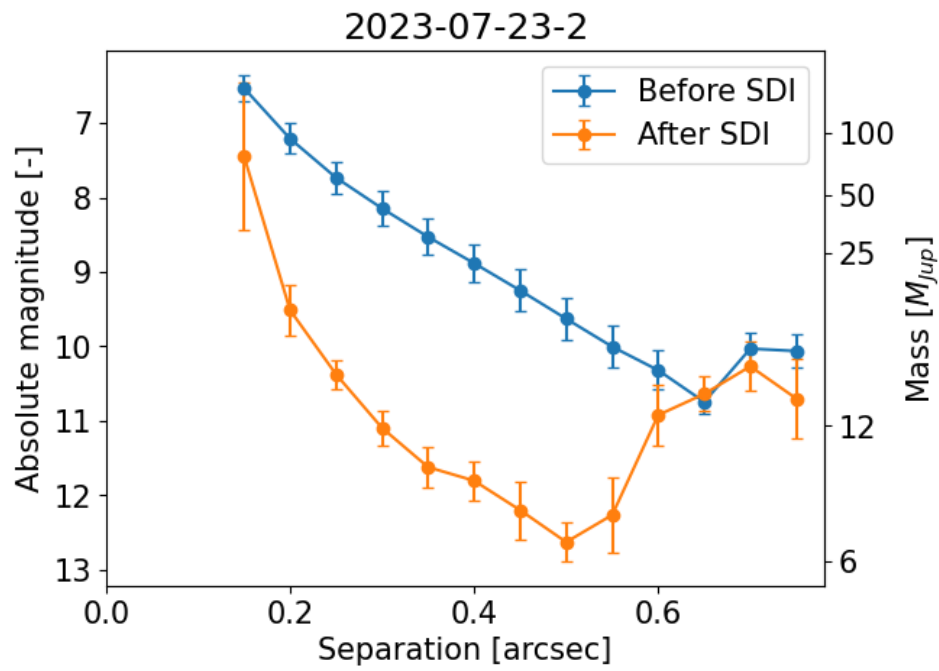
Figure B.26: Contrast curve for the observation of 2MASS J12472196-6808397.
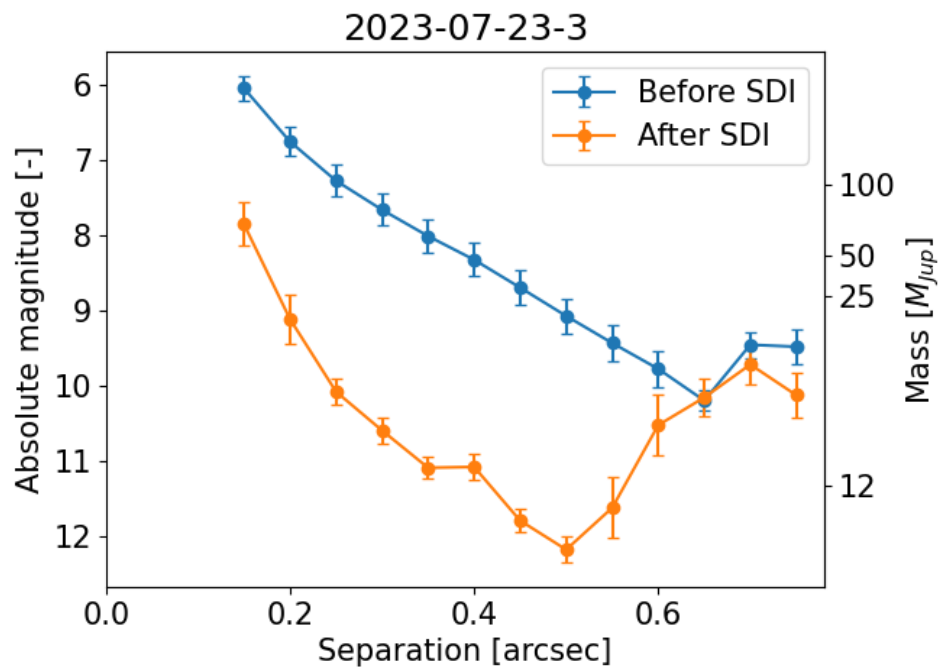
Figure B.27: Contrast curve for the observation of 2MASS J13095880-4527388.
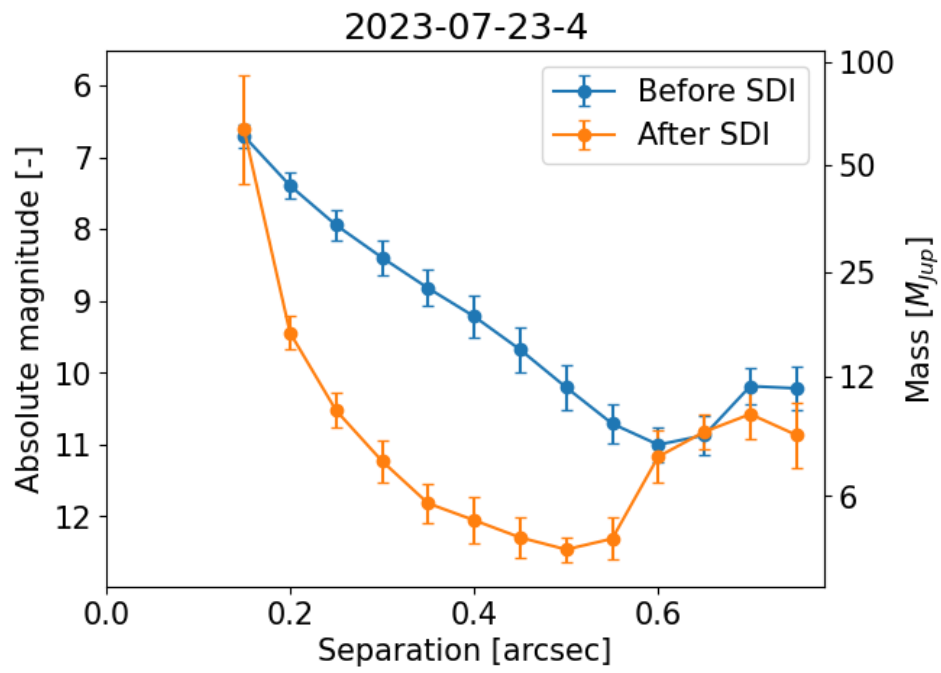
Figure B.28: Contrast curve for the observation of 2MASS J13335481-6536414.
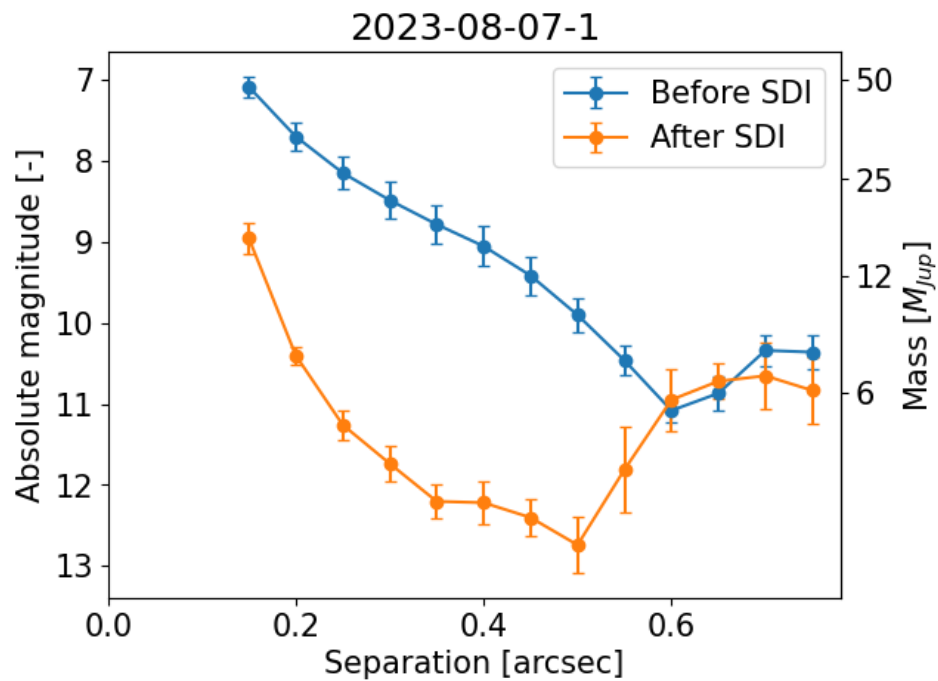
Figure B.29: Contrast curve for the observation of 2MASS J12483152-5944493.
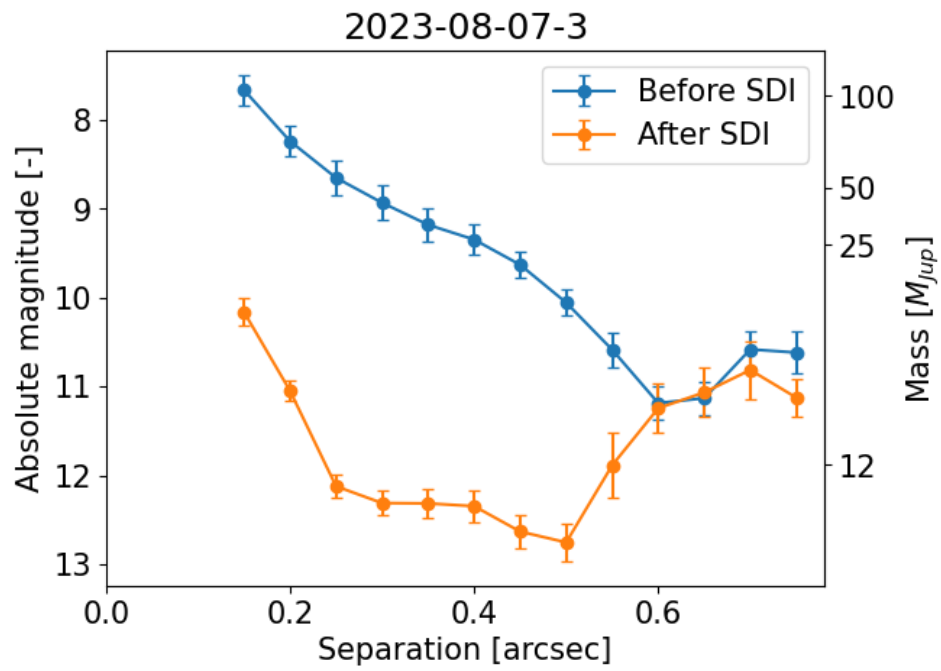
Figure B.30: Contrast curve for the observation of 2MASS J13343188-4209305.
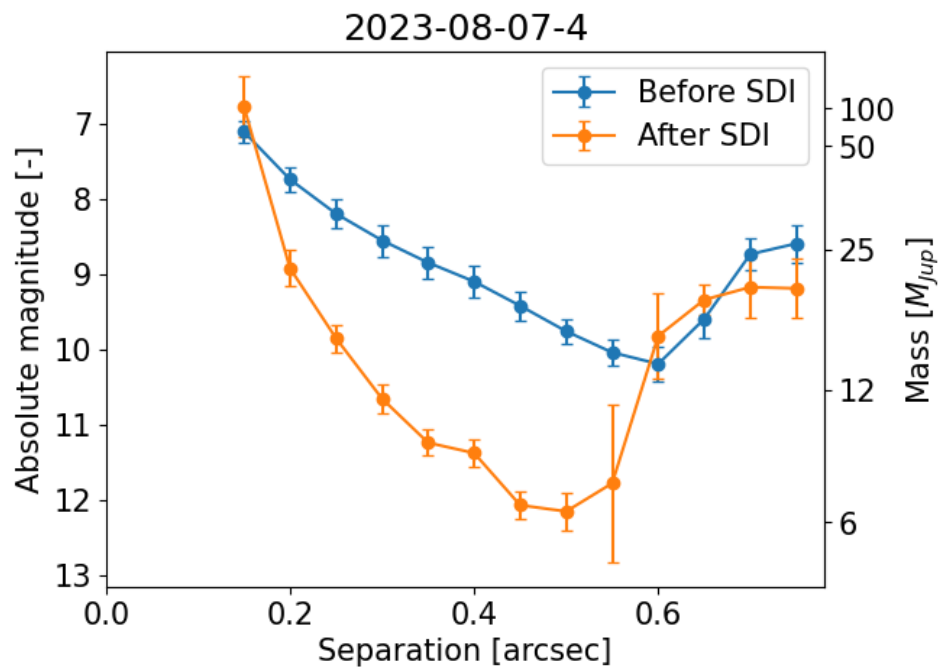
Figure B.31: Contrast curve for the observation of 2MASS J13444279-6347495.
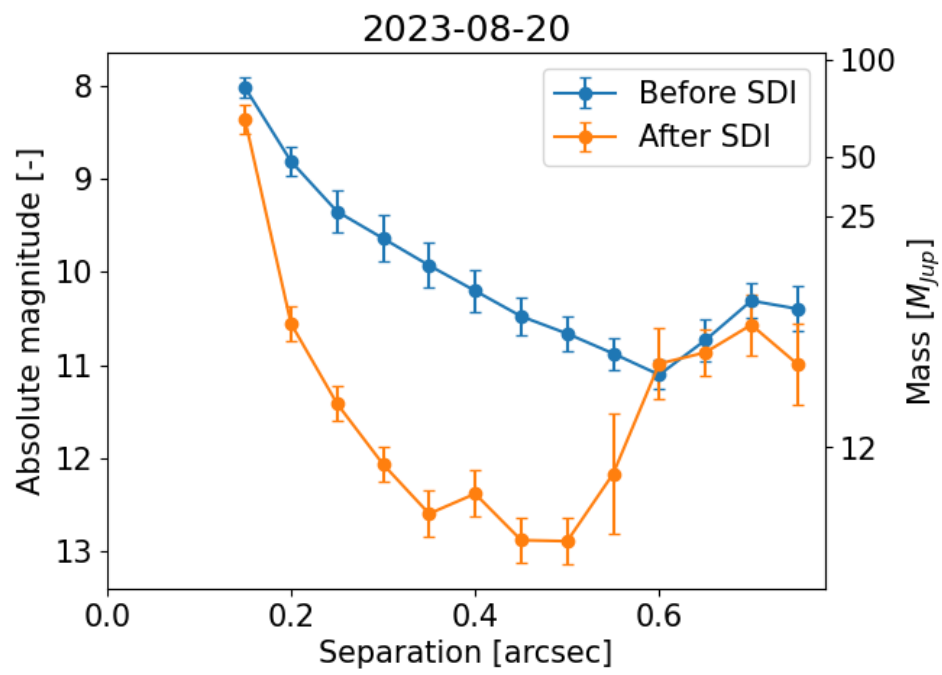
Figure B.32: Contrast curve for the observation of 2MASS J12205449-6457242.